CEACAM mediated internalization of Opa proteoliposomes into human cells

Jason Philip Kuhn

Middletown, MD

B.S. University of Maryland, Baltimore County, 2010

A Dissertation presented to the Graduate Faculty of

the University of Virginia in Candidacy for the Degree of

Doctor of Philosophy

Department of Chemistry

University of Virginia

August, 2018

August, 2018

Abstract

Carcinoembryonic antigen-like cell adhesion molecules (CEACAMs) are cell-surface proteins that are widely-expressed in the human body. In humans, CEACAM proteins play diverse roles in mediating cell adhesion, migration, and even host-pathogen interactions. Additionally, several CEACAM proteins exhibit increased expression on tumour cells in certain forms of pancreatic, gastric, hepatic, lung, and colorectal cancers. Because of the overexpression of CEACAM proteins on malignant cells, there is interest in developing strategies to target therapeutic delivery to cells overexpressing CEACAM proteins.

Neisseria gonorrhoeae and *Neisseria meningitidis* are Gram-negative bacteria that infect human host cells, including through binding to CEACAMs. Various surface proteins on *Neisseria* mediate bacterial engulfment into host cells. One such group of proteins is the opacity-associated (Opa) proteins on the outer membrane of *Neisseria*, which mediate *Neisseria* interactions with human CEACAM proteins. Previous work has shown that purified, recombinant Opa proteins can be folded into small unilamellar vesicles, termed liposomes, where the Opa proteins are functional. Because liposomes are common platforms for therapeutic delivery, this work investigates whether Opa-liposomes can be used to induce liposomal uptake into human cells through Opa-CEACAM interactions. Uptake of Opa-liposomes into cells through CEACAM would have relevance for the targeted delivery of therapeutic compounds into cancer cells overexpressing CEACAM proteins. This thesis details progress toward investigating Opa-liposome interactions with CEACAM.

Results indicate that cellular binding and uptake of Opa-liposomes can be assayed using imaging flow cytometry, with internalized liposomes able to be identified from surface-bound liposomes during data processing. Opa_{60} on liposomes promotes energy-dependent uptake of liposomes into HeLa cells when compared to control liposomes containing an

Opa_{60} variant in which the binding region of Opa_{60} has been removed. Non-specific uptake of liposomes is described in the context of the HeLa cells used in these experiments, with particular emphasis on the relationship between liposome size and non-specific uptake. Results suggest that small liposomes can be non-specifically internalized into HeLa cells through bulk fluid-phase uptake during macropinocytosis.

Additionally, various considerations for the uptake of Opa-liposomes into CEACAM1+ HeLa cells are detailed. A positive correlation was found between progression through cell cycle and CEACAM1 expression, which results in increased Opa60-liposome internalization into HeLa cells later in the cell cycle that express higher amounts of CEACAM1. Following internalization, at least some Opa-liposomes are trafficked through the classical endocytic pathway, as shown through colocalization with markers for early endosomes and lysosomes. Finally, preliminary experiments are described in which Opa-liposomes are loaded with doxorubicin in order to investigate the Opa-mediated delivery of an active compound to cells.

Acknowledgments

I am indebted to many people for helping me complete this work. Firstly, thank you to Dr. Linda Columbus, for all the encouragement and advice over the years. Whenever I found myself unsure of the next step, she was there with new ideas and the belief I would see things through.

Thank you to everyone in the Columbus lab, past and present, for your help over the years. Thank you especially to Marissa Kieber, Nicole Swope, Ashton Brock, Jennifer Martin, Steven Keller, and Tracy Caldwell. You guys are great, even if half of you pushed me into an imaginary tar pit. Thank you as well to members of the Mura lab for their friendship and support, especially Charles McAnany and Kimberly Stanek.

I am deeply grateful to Dr. Alison Criss and the members of her lab for their help and support over the years. The Criss lab provided me space and materials in order to culture the cells necessary for my experiments. Without that support, this project would not have been possible. In particular, I would like to thank Asya Smirnov, who trained me in how to work with HeLa cells, and provided valuable advice and guidance whenever I needed it. I would like to thank the lab of Dr. Scott Gray-Owen at the University of Toronto for generously providing us stably-transfected HeLa cells with which we could conduct our experiments.

I would like to thank Dr. Cassandra Fraser and her lab, especially Christopher DeRosa, for teaching me how to use their DLS plate reader and allowing me access to it.

I would like to thank Stacey Guillot of the Advanced Microscopy Facility for training and help with confocal microscopy. I would especially like to thank Joanne Lannigan and the staff at UVA's Flow Cytometry Core Facility for their training and help with imaging flow cytometry, and their generous advice whenever I needed it.

Thank you to both my parents and my brother Matthew for their support and encouragement over the years.

And thank you to my many friends whose friendship was always a source of joy even when things were rough in lab. I am forever indebted to old friends and the new friends I made in graduate school! Special thanks to Andrea. I can't imagine what graduate school without your friendship and support would have been like!

Table of Contents

Chapter 1—Introduction

1.1—Introduction to Cancer and Motivation for Work

1.1.1—Introduction to Cancer

Cancer is a widespread health concern; an estimated 1.6 million cases of cancer were diagnosed in the United States in 2016, with over half a million people dying from the disease. Nearly 40% of men and women will be diagnosed with cancer at some point in their lives [1]. A pressing need exists therefore to improve the early diagnosis and treatment of cancer in order to generate better patient outcomes. This thesis will investigate one potential avenue toward that aim.

1.1.2—Definition and Hallmarks of Cancer

Although frequently referred to as one disease, cancer in reality is an umbrella term under which many pathophysiological states can be grouped which lead to aberrant and unregulated cell growth [2]. In contrast to normal tissues, which closely regulate cell growth and proliferation, cancer cells lose the ability to regulate cell replication [2]. There exist many types of cancers arising from varying genetic causes and within different body tissues, which can produce different pathophysiological manifestations and health outcomes. Nonetheless, six major “hallmarks of cancer” have been identified which constitute a collection of common capabilities in the development of tumours. These capabilities include: sustaining proliferative signalling, evading growth suppressors, resisting cell death, enabling replicative immortality, inducing angiogenesis, and activating invasion and metastasis [3].

1.1.3—Molecular Causes of Cancer

The deregulation of cell proliferation in cancer results from a number of changes to the normal processes which carefully control cell growth and division. These changes frequently result from accumulated DNA mutations that destabilize cell genomes. Mutations leading to tumorigenesis may include activating mutations that result in constitutive signalling of cell growth pathways, such as mutations in the catalytic subunit of phosphoinositide 3-kinase isoforms which can activate proliferative PI3-kinase signalling pathways [3, 4]. Aberrant growth signals may be sustained through the production of growth factors which bind tumour-surface receptors, sometimes through autocrine stimulation by the tumour cells themselves, and sometimes through stimulation of neighbouring healthy cells which results in the production of excess growth factors nearby [3]. Additionally, tumour cells often upregulate receptors on their surface in order to maximize their response to growth signals, as demonstrated by increased Endothelial Growth Factor Receptor (EGFR) expression in several tumour lines [3].

In addition to the upregulation of growth pathways, tumour cells promote unrestrained growth by interrupting negative feedback mechanisms that serve to moderate proliferation. For instance, loss of function mutations in PTEN phosphatase prevents the degradation of phosphatidylinositol(3,4,5) trisphosphate, a product of PI3-kinase signalling which promotes cell growth and survival [3, 4]. Similarly, mutations in *ras* genes can result in loss of Ras GTPase activity, which normally provides an intrinsic negative-feedback mechanism to proliferative Ras signalling [3].

In contrast to the confluent monolayers formed by healthy cells in culture, tumour cells form dense populations of cells whose growth is unrestricted by neighbouring cells. Healthy cells experience “contact inhibition” whereby proliferation is attenuated when cells contact

neighbouring cells. Several mechanisms support this growth inhibition including, for example, the coupling of the cell-surface adhesion molecule E-cadherin to the growth factor receptor EGFR, which sequesters growth receptors and strengthens the adhesion of cell-cell attachments [3, 5].

Commensurate with dysregulation of proliferative pathways, cancer cells promote their survival by interfering with normal cellular apoptotic machinery. This machinery typically induces programmed cell-death as a response to signals and stresses which occur in cancer cells, including oncogenic signalling imbalances and DNA damage [3, 6]. For example, the tumour suppressor TP53 initiates apoptotic signals following high levels of DNA breaks and chromosomal abnormalities; loss of TP53 function in tumour cells, or upregulation of competing antiapoptotic regulators, can prevent programmed cell death [7].

1.1.4—Effects of tumorigenesis

As a result of alterations in genes and expression of key regulatory molecules, cancer cells induce replicative immortality within themselves, enabling them to avoid inducing senescence (a viable but nonproliferative state) or apoptosis. This immortalization is required for macroscopic tumour formation and is supported by increased expression of telomerase and DNA telomere length [8]. Supporting immortalized cell growth is an increased reliance on angiogenesis near the site of tumours, whereby tumour cells induce the growth of new blood vessels to help deliver nutrients and oxygenated blood to hyperproliferating cells [9]. This tumour neovasculature is often characterized by high capillary growth, high vessel branching, and leakiness resulting from local fenestrations [10, 11].

In late stage tumour growth, the invasion of cancer cells through neighbouring cell layers is frequently followed by metastasis to tissues distant from the tumour's site of origin. This

invasion of local tissues, entry into nearby vasculature, extravasation into distant tissues and formation of new colonies is favoured by expression of various ECM-degrading proteases and aberrant expression of surface cell-cell adhesion molecules. For example, the loss of E-cadherin surface expression can alter cell-cell attachments and promote invasion and metastasis, while expression of N-cadherin, typically expressed in migrating neurons and cells during organogenesis, is often upregulated in invasive cancer cells [12, 13].

1.1.5—Common membrane phenotypes of tumour cells

Tumour cells frequently display surface physiologies different from healthy cells. Certain proteins, especially antigen-presenting proteins involved in immune surveillance, may be downregulated in cancer, while other molecules increase their concentrations on cancer cell membranes. The folate receptor-α, for instance, transports the water soluble B-vitamin folic acid into cells and is commonly overexpressed on human tumours including ovarian, lung, and breast cancers [14, 15]. Many tumour lines including H1299 cells express high levels of EGF receptors as mentioned earlier [16], while several members of the widespread carcinoembryonic antigen-like cell adhesion molecule (CEACAM) family are upregulated on different cancers of the pancreas, liver, lung, and colon [17] (See 1.2.3).

1.2—CEACAM family proteins

1.2.1—Introduction and normal role of CEACAM proteins

Carcinoembryonic antigen-like cell adhesion molecules (CEACAMs) are a family of cell-surface glycoproteins involved in cell-cell adhesion mediated by homophilic and heterophilic interactions. Found in a number of mammalian species, including humans, mice, rats, and

various primates, CEACAM proteins are widely-expressed in various epithelial and endothelial tissues, as well as on cells of the immune system. The CEACAM family contains eleven unique cell-surface glycoproteins (CEACAM1, CEACAM3-8, CEACAM18-21) and one fully-secreted member (CEACAM16) [18, 19]. While CEACAM5, found on epithelial cells of the gastrointestinal tract and other mucosal surfaces such as the nasopharynx, lung, and urogenital tract [20, 21], was in 1965 the first CEACAM member identified [22], CEACAM1 is the evolutionary progenitor of the family. Consequently, CEACAM1 shows the broadest tissue distribution of any member in the family, and is found on epithelial cells, endothelial cells, lymphocytes, and neutrophils [20]. In contrast, CEACAM3 is found exclusively on granulocytes and is not believed to contribute to cell-adhesion, but rather plays a role in human immune responses to certain bacterial infections [23] (see 1.3.3).

As widely-expressed cell adhesion proteins, members of the CEACAM family play significant roles in cell processes beyond cell adhesion. CEACAM1, for example, has demonstrated pro-angiogenic effects, including tumor angiogenesis, through the stimulation of cell proliferation and migration of vascular endothelial cells [24-26]. Additionally, CEACAM1 serves as a phosphorylation substrate of the insulin receptor following insulin binding, downregulating insulin signalling and promoting endocytosis of the insulin-insulin receptor complex [27].

1.2.2—Structure of CEACAM proteins

Part of the immunoglobulin (Ig) super-family of proteins, all CEACAM members contain at least one variable N-terminus (IgV)-like domain characterized by a compact fold of two sandwiched β-sheets **(Figure 1)**, whose size ranges between 85-110 amino acids [20, 28]. The N-terminal domain is an important CEACAM binding domain—in CEACAM1, for

instance, the N-terminus domain mediates *trans*-homotypic binding and promotes *cis*-dimerization [29-31]. Most CEACAM members contain between one and six additional constant (IgC)-like domains of either the A or B form, which vary in their number of amino acids (93 and 85 residues respectively) **(Figure 2)**. Seven CEACAM members, including CEACAM1, CEACAM3, and CEACAM4 are typically attached to the cell surface through a transmembrane domain, while four other CEACAMs, including CEACAM5, CEACAM6, CEACAM7, and CEACAM8 are GPI-anchored to the membrane [32]. CEACAM1, CEACAM3, and CEACAM7 may show variable mRNA splicing (12, 3, and 2 variants respectively); these different spliceforms may vary in the number and size of extracellular domains. Importantly, variations in the number of CEACAM1 extracellular domains may lead to differences in its self-adhesion [33]. CEACAM1 and CEACAM3, in addition to their transmembrane domains, contain cytoplasmic domains which can vary between short or long splice forms. Long cytoplasmic domains may contain an immunoreceptor tyrosine-based inhibition (CEACAM1) or activation (CEACAM3) motifs (ITIM/ITAM) which are involved in transducing binding signals inside the cell [18]. Short splice variants do not contain tyrosine phosphorylation sites and consequently lack the ability to transmit signals intracellularly [18]. Consequently, adjusting the ratio of short to long CEACAM isoforms at the cell surface may be one way for cells to control CEACAM signalling levels [18]. In addition, the balance of CEACAM monomers, dimers, and clusters on the membrane can modulate CEACAM interactions with intracellular signalling molecules subsequent downstream effects [18, 31]. Cells may partially control CEACAM dimerization through altering its levels of glycosylation on the N-terminus and constant domains [33].

1.2.3—Pathophysiological Expression of CEACAM proteins

The first CEACAM member found, CEACAM5, was identified due to its presence in human colon cancer extracts where its abnormal expression led to high serum levels indicating colorectal cancer [34, 35]. In addition to colorectal cancer, CEACAM5 is upregulated on gastric and lung carcinomas, where CEACAM5 levels have been correlated with EGFR mutations [34, 36, 37]. Similarly, CEACAM6 overexpression has also been associated with gastric, lung, and colorectal carcinomas [34, 38, 39]. Importantly, both CEACAM5 and CEACAM6 have been found to inhibit normal cell apoptosis among cells that have lost attachment to their substrate [32, 40]. CEACAM1 has been found to increase its expression on gastric and squamous cell lung carcinomas, as well as metastatic colorectal cancer (94% of tumours are positive), cutaneous melanomas, pancreatic adenocarcinomas, and bladder cancer (where nearly 100% of tumour cells were positive) [41, 42]. Due to the increased expression of CEACAM1 on advanced cancers, high CEACAM1 expression is often considered a marker for poor prognosis [43]. Additionally, CEACAM1 expression promotes evasion of immune killing, as CEACAM1-L has shown inhibitory effects on T-cell receptor-mediated cytotoxicity [44] as well as decreasing killing of tumour cells by Natural Killer cells [45, 46]. Highly correlated with tumour angiogenesis and vascular endothelial growth factor (VEGF) activity, CEACAM1 overexpression can also be found on microvessels feeding renal, prostate, and urinary bladder carcinomas [24]. In light of the high correlation between members of the CEACAM family and the progression of certain cancers into advanced stages, there is interest in developing new strategies to target drugs to tumour cells overexpressing CEACAM receptors [42]. One possible strategy may employ CEACAM-binding Opacity proteins found on *Neisseria* bacteria.

1.3—Neisserial Opa proteins: context, structure, and binding to CEACAMs

1.3.1—Introduction to pathogenic *Neisseria* bacteria

Neisseria gonorrhoeae and *Neisseria meningitidis* are pathogenic Gram-negative bacteria that colonize various mucosal surfaces of the human urogenital tract, nasopharynx, and eye [47]. Colonization is driven by the phase-variable expression of various adhesion proteins such as type IV pili, PorB, opacity-associated (Opa) proteins, as well as lipooligosaccharides [47-50]. Following attachment, *N. gonorrhoeae* and *N. meningitidis* can induce entry into human cells through the binding of bacterial proteins to host receptors, such as the engagement of bacterial Opa proteins to heparin sulfate proteoglycans [32, 44, 51, 52] or CEACAM proteins [32, 47] **(Figure 3)**.

1.3.2—Opacity (Opa) protein structure, expression, and membrane context

Neisserial Opacity proteins contain eight anti-parallel beta strands in a beta-barrel configuration with four extracellular loops **(Figure 4)** [53]. Typically around 20-30 kDa in size, these proteins inhabit the outer membrane of the gram-negative bacteria. As such, the barrel is primarily nonpolar, while its extracellular loops contain a mix of polar and nonpolar amino acids **(Figure 5)**. Compared to the rigid barrel, the extracellular loops of Opa proteins are highly disordered and mobile. Sequence variation occurs within loops 1, 2, and 3, with the majority of the variation contained within loops 2 and 3 (termed the hypervariable loops, or HV1 and HV2 respectively). Loop 1 contains a slightly more conserved semi-variable (SV) region. The fourth extracellular loop, smaller than the other three, does not display significant variation between different Opa forms. The periplasmic side of the beta barrel contains short turns between the beta strands. The FA1090 strain of *N. gonnorrhoeae* encodes

eleven Opa proteins, while *N. meningitidis* encodes four proteins, with *opa* genes dispersed through the genomes for both [18, 54, 55].

The outer membrane of *N. meningitidis* and *N. gonorrhoeae* envelops both an inner membrane and a layer of peptidoglycan which is sandwiched between the two membranes. The outer membrane of *Neisseria* species typically contain high levels of phosphatidylethanolamine (PE), along with phosphatidylglycerol (PG), cardiolipin (CL), and phosphatidate (PA) [56, 57]. Additionally, the outermost leaflet of the outer membrane, from which Opa extracellular loops extend, contains a truncated form of lipopolysaccharide (LPS) termed lipooligosaccharide (LOS). LOS lacks the O-side chain repeat found in LPS and can itself mediate bacterial attachment and invasion [56, 58]. Understanding the components of the outer membrane of *Neisseria* bacteria is important as interactions can exist the binding loops of Opa and LOS which may modulate Opa specificities and affinities toward binding targets [59].

Opa proteins contain a high level of sequence diversity, primarily generated by recombination events within the bacterial genome or with extracellular DNA [18, 55, 60]. At least 338 unique *opa* alleles have been identified, which include at least 26 different SV regions, 96 unique HV1 regions, and 127 unique HV2 regions [18]. This high sequence diversity may contribute to Neisserial evasion of the human immune response. Additionally, Opa proteins are phase-variably expressed on the surface of *Neisseria*, with individual bacteria able to express zero, one, or multiple unique Opa proteins at any one time. This variable expression results from the presence of a pentameric coding repeat sequence (5'-CTCTT-3') within the leader peptide sequence [18, 61]. Slipped-strand mispairing during DNA replication results in frameshifts which control the repeats [18, 61]. Variable expression of different Opa proteins within subpopulations of *Neisseria* likely also contribute to bacterial survival and immune escape.

1.3.3—Neisserial Opa binding of CEACAM proteins: molecular interactions and cellular responses

Neisserial Opa binding to human CEACAM1, CEACAM3, CEACAM5, or CEACAM6 proteins can promote bacterial internalization into these host cells. Binding is largely contingent on the extracellular HV1 and HV2 sequences of Opa proteins, which are the primary determinants of target receptor affinity and specificity [62]. Interactions of Opa with CEACAM necessitates distinct combinations of HV loops, as chimeric versions of the protein that combine HV loops from different CEACAM-binding proteins show significantly reduced or no activity [62]. In addition to Opa HV1 and HV2 regions, the SV region can facilitate CEACAM binding, as its removal reduces affinity without fully abolishing binding [62]. Loop 4 has not been shown to play a role in CEACAM recognition.

Little is known about specific residues on Opa responsible for CEACAM binding. In contrast, key residues have been identified on particular CEACAM proteins which promote Opa binding. Opa interactions with CEACAM1, for instance, occur on the non-glycosylated face composed of strands C'', C', C, F, and G, and in all cases require the presence of CEACAM residues Tyr34 and Ile91 [63], with several other CEACAM1 residues facilitating binding to at least some Opa proteins **(Figure 6)**.

Following cellular CEACAM binding by Opa, different internalization processes are activated depending on the identity of the CEACAMs engaged. For instance, Opa binding of CEACAM1, which contains an ITIM, appears to promote serine/threonine kinase recruitment and receptor interactions with PKC and protein kinase A, leading to bacterial engulfment [32]. CEACAM3 engagement induces Src family kinases to phosphorylate tyrosine residues within the cytosolic ITAM, resulting in recruitment of effectors including Syk tyrosine kinase as well as a Rac- and Cdc42-caused reorganization of actin microfilaments that wrap around

Neisseria [32]. In contrast to the membrane-spanning CEACAM1 and CEACAM3, CEACAM5 and CEACAM6 are GPI-anchored and consequently lack cytoplasmic domains. Internalization of Opa-expressing bacteria with these receptors is believed to occur through recruitment of adjacent receptors in a progressive "zippering" mechanism whereby the host cell membrane envelops the bacterium [64].

Following internalization into model epithelial cells, such as HeLa cells stably transfected to overexpress a single Opa-binding CEACAM receptor, phagosomes containing single Opa-expressing bacteria typically mature in a process that leads to phagosome acidification and bacterial killing [32]. Importantly, however, this process likely differs in non-model cell lines which display multiple CEACAM proteins, as it was reported that in polarized monolayers of T84 colonic carcinoma cells, which express CEACAM1, CEACAM5, and CEACAM6, *Neisseria* bacteria displaying a mixture of Opa proteins can remain viable after transcytosing through the cells [65]. Thus, the intracellular fate of Opa-expressing bacteria may vary depending on the identities of Opa proteins engaging different CEACAMs. As the Opa-driven internalization of *Neisseria* into human cells can engage CEACAM, it raises the question as to whether Opa-CEACAM interactions can be used for therapeutic delivery. Since Opa proteins require a membrane environment to remain folded and functional, one possible strategy may employ therapeutic liposome particles as membrane mimics.

1.4—Liposome Nanoparticles for Drug Delivery

1.4.1—Introduction to liposomes

Liposomes are artificial lipid vesicles ranging between ~25 nanometers to several micrometers in size [66, 67]. They consist of one (unilamellar) or multiple (multilamellar) bilayers enclosing one or more internal aqueous compartments. Liposomes are often

composed of naturally-occurring lipids and therefore show high biocompatibility and low toxicity [68]. Lipids used can include: glycerophospholipids, whose polar headgroups attach to nonpolar tails through phosphodiester linkages, phosphatidic acid, cardiolipin, and cholesterol [69]. Following vesicle formation, the aqueous compartments within liposomes can entrap water soluble drugs, while hydrophobic drugs can partition into the hydrophobic lipid-tail region within the liposome bilayer **(Figure 7)** [68, 70]. Encapsulation of therapeutic compounds can prevent decomposition or metabolism of these compounds while allowing for controlled release at specific targets [68]. Therapeutic liposomes can accumulate at target sites passively (see 1.5.1) or use surface ligands to actively target subpopulations of cells [71]. For instance, immunoliposomes can incorporate antibodies on their surface to promote binding interactions with specific cell receptors. Examples include anti-α8 immunoliposomes which may treat lupus and glomerular diseases [72], or anti-HER2 immunoliposomes which can target delivery to a number of different cancers overexpressing HER2 on their surface [73]. In addition to proteins, liposomes can also employ non-protein targeting ligands, such as surface-conjugated folic acid, which promotes delivery to cells overexpressing folate receptors, as occurs on many cancers [74].

1.4.2—Physical properties of liposomes

The physical properties of liposomes can be modulated by the types and proportions of lipids used to create the vesicles. Important properties include liposome size and stability; bilayer thickness, fluidity, hydrophobicity, and permeability; temperature and pH sensitivity; and surface charge, among others. Understanding these physical properties of liposomes is important for being able to modulate properties important to therapeutic delivery, such as

drug permeability, liposome aggregation and fusion, and non-specific cell membrane adhesion.

The physical properties of lipids result from structural variations in their nonpolar tails as well as their polar headgroups. These variations can include alkyl chain length and degree of unsaturation in the tails, as well as their headgroup size and charge. With regard to lipid tail properties, longer lipid tails tend to associate more tightly together than shorter lipid tails due to increased van der Waals interactions, resulting in a less fluid bilayer when composed of lipids with higher tail lengths. This effect can be seen in the melting temperatures of saturated phosphatidylcholine lipids composed of fourteen (14:0 PC), sixteen (16:0 PC), and eighteen (18:0 PC) carbons, which demonstrate transition temperatures (the temperature required for the bilayer to transition from an ordered to disordered liquid state) of 24°C, 41°C, and 55°C respectively [75]. Similarly, the presence of unsaturated double bonds within the lipid tail can introduce "kinks" in the tail region that prevent tight association of lipid chains, leading to lower transition temperatures for lipid bilayers containing unsaturated lipids. For instance, 18:1 (Δ9-cis) PC, which contains a double bond after the ninth carbon, demonstrates a transition temperature of -17°C, 72 degrees lower than its tail length-equivalent unsaturated counterpart (18:0 PC) [75].

The presence of cholesterol also has a significant effect on membrane fluidity and hydrophobicity, and for this reason therapeutic liposomes may contain cholesterol in order to modulate these properties [76]. Cholesterol differs from many other typical lipids in that its non-polar tail contains a large, fairly rigid set of three six-member rings and one five-member ring, as well as a short alkyl chain. In contrast, its polar head-group is a comparatively-small hydroxyl group. Cholesterol exerts different bilayer effects depending on its concentration in the bilayer and the temperature [77]. In model bilayers composed of dimyristoyl phosphatidylcholine (14:0 PC) and 0-10 mol% cholesterol, for instance, a liquid disordered

(l_d) phase was seen above the transition temperature of 14:0 PC (23-24°C) and a solid ordered (s_o) phase below the transition temperature, while increasing the amount of cholesterol to 10-30 mol% induced the formation of liquid ordered domains both above ($l_d + l_o$) and below ($s_o + l_o$) the phase transition temperature [77, 78]. Above 50 mol% cholesterol, the bilayer was fully l_o [77, 78]. Thus, it appears cholesterol can both increase membrane fluidity and packing depending on its concentration and the temperature. Additionally, cholesterol can exhibit effects on membrane hydrophobicity, as below 30 mol% cholesterol in 14:0 PC membranes was found to increase bilayer hydrophobicity near the interior while decreasing hydrophobicity at the membrane surface [77]. Because cholesterol is a powerful modulator of membrane fluidity, liposome formulations must carefully optimize its concentration.

In addition to lipid tails, variations within lipid headgroups can also induce changes in bilayer properties. Common headgroups for phospholipids include phosphatidylcholine (PC), phosphatidylglycerol (PG), phosphatidylserine (PS), phosphatidylinositol (PI), and phosphatidylethanolamine (PE). Because these lipids contain a negatively-charged phosphodiester linkage between their tails and headgroups, they are typically either anionic at physiologic pH (PG, PS, PI) or net-neutral zwitterions (PC, PE), with zwitterionic lipids forming the majority of the native bilayer in cells compared to anionic lipids [79]. In addition to charge, headgroup identity can in some cases exert profound effects on bilayer structure. For instance, due to the small size of phosphatidylethanolamine, lipids with a PE headgroup often do not associate into a typical bilayer when protonated [80], but instead tend to form an inverse hexagonal phase, leading to their use in special fusogenic liposome formulations [81, 82].

1.4.3—Suggested therapeutic relevance of Opa proteoliposomes

As membrane proteins, Neisserial Opa proteins require a membrane-like environment to stabilize their beta-barrel fold. In the native biological context for Opa proteins, this membrane environment is the outer membrane of *N. gonorrhoeae* and *N. meningitidis*. Established protocols have been published, however, describing methods to purify and fold Opa proteins into liposomes [83]. The resulting Opa proteoliposomes stabilize the Opa fold in its functional form, as shown by the recognition and binding of the soluble N-terminus of CEACAM1 and CEACAM3 by various Opa proteoliposomes [84]. In light of the overexpression of a number of CEACAM proteins including CEACAM1, CEACAM5, and CEACAM6 on the surface of several cancers, as well as the recognized ability of Opa proteins to induce particle uptake into cells expressing these types of CEACAMs, it may be possible for liposomes containing folded and functional Opa proteins to therefore induce liposomal uptake into CEACAM expressing cells. Because liposomes can be useful vehicles for the targeted delivery of therapeutic compounds, targeted uptake of Opa proteoliposomes into cells through CEACAM proteins may serve as a strategy to enhance therapeutic delivery to CEACAM-expressing cancers.

1.5—Nanoparticles and Cellular Delivery

1.5.1—*In vivo* circulation of NPs

The *in vivo* circulation of lipid nanoparticles (NPs) such as liposomes depends on myriad factors including particle size, charge, lipid composition, drug loading, and presence of surface proteins or polymers. *In vivo* circulation lifetime of nanoparticles is primarily limited by uptake into the reticuloendothelial system (RES), including macrophages in the spleen and Kupffer cells in the liver [85]. Increasing NP circulation times by preventing RES uptake

better allows NPs to reach target sites, so a great deal of effort has been put into understanding these uptake processes [85]. It has been reported that larger NPs are more prone to uptake through opsonisation by immune cells, so smaller particles (between 50-200 nm) are often preferred in order to increase circulation time [85]. NPs with a positive surface charge are also more susceptible to non-specific uptake by immune cells, owing to the slight negative charge in the membranes of most healthy cells [86].

A major breakthrough in lengthening the timescales of NP *in vivo* circulation came with the incorporation of high molecular weight water soluble polymers onto the surface of NPs; these polymers mimic the high surface glycosylation that red blood cells use in order to escape immune killing [87, 88]. The prototypical polymer used with NPs, polyethylene glycol (PEG), ranges in size from several hundred to several million grams per mole, although most sizes used for therapeutic purposes are around 1000-5000 grams per mole. Surface PEG helps prevent serum-protein aggregation on the NP surface, thereby decreasing RES opsonisation [87]. In order to better treat Kaposi's sarcoma, liposome-encapsulated doxorubicin (Doxil) incorporates PEG-2000 conjugated to 18:0 PE lipids, which increases liposome circulation times and reduce volume of distribution, resulting in improved patient outcomes compared to unencapsulated doxorubicin [89, 90].

The benefits of increased NP circulation times can partially be explained through the Enhanced Permeability and Retention (EPR) effect, whereby rapid vasculature growth induced by tumour cells tends to contain holes in the vasculature of up to 600 nm, called fenestrations [91-93]. The poor quality vasculature around tumours subsequently permits increased departure of circulating NPs from tumor vasculature compared to healthy blood vessels, allowing NPs to preferentially congregate at tumors and deliver their cargo to tumour cells [92].

In addition to the EPR effect, other passive targeting techniques can be utilized when NP circulation times are increased. For instance, due to the overreliance of cancer cells on glycolysis to satisfy increased energy demands, the local milieu around tumour cells is often more acidic than near healthy tissues, which has led to the development of pH-sensitive liposomes incorporating DOPE that enhances membrane fusion with cells at low pH [94-96].

1.5.2—Cell uptake of NPs into target cells

Endocytosis can be separated into three distinct modes of uptake: fluid-phase, adsorptive, and receptor-mediated [97]. In fluid-phase uptake, molecules are non-specifically taken into cells as part of bulk extracellular fluid uptake, and so internalize with the same concentrations as in the extracellular fluid [97]. Adsorptive uptake describes conditions in which molecules non-specifically adhere to the cell surface, such as through charge-driven electrostatic interactions; this adsorption leads to a localized concentration at the cell membrane, and internalization of these particles tends to follow that of the plasma membrane [97]. During receptor-mediated endocytosis, such as the Opa-CEACAM interaction between *Neisseria* and host cells, ligands engage cell-surface receptors, concentrating the ligands at specific locations on the cell surface prior to internalization. The kinetics of uptake are affected by both the strength of the ligand-receptor binding as well as receptor concentration and internalization pathways utilized [97].

Endocytic uptake may also be defined by the size of particles internalized. Phagocytosis describes the uptake of large particles (>0.5 μm) into specialized cells such as macrophages and neutrophils [97, 98]. This receptor-mediated process initiates actin-modulated formation of cell-membrane extensions that surround and engulf the particle [99]. Phagosomal maturation leads to fusion with endocytic components and the formation of low pH

phagolysosomes where particle degradation occurs [98]. In contrast to specialized phagocytes, pinocytosis occurs in all cells and involves the uptake of smaller volumes of fluid and molecules. Several pinocytic pathways have been identified with unique mechanisms of internalization: clathrin-mediated endocytosis (CME), macropinocytosis, caveolae, and clathrin-independent endocytosis [100-102]. Described in further detail are CME and macropinocytosis.

Clathrin-mediated endocytosis: CME occurs constitutively in mammalian cells and involves the receptor-mediated, energy-dependent uptake of essential molecules. Prototypical examples include low-density lipoproteins (LDL) transporting cholesterol using LDL receptors, and the protein transferrin carrying iron into cells through Tf [97, 103, 104]. Following ligand-receptor binding in CME, receptors cluster on the membrane into clathrin-coated pits which, with the help of the GTPase dynamin [105], invaginate and pinch off into the cell as vesicles around 100 to 150 nm in diameter [102]. Inside the cell, the clathrin-complexes coating the vesicles disassemble and detach; the resulting early endosomes (pH 6) mature in a process controlled by the small GTPase Rab proteins [106] and form late endosomes which eventually fuse with lysosomes (pH <5) [107]. During this process of endosomal maturation, internalized ligands disassociate from their receptors and both may be sorted to separate destinations, such as lysosomes, the Golgi apparatus, or the nucleus for ligands, while frequently internalized receptors are recycled back to the plasma membrane [97, 107]. A more detailed discussion of endosomal processing can be found in Chapter 4.

Macropinocytosis: In contrast to CME, macropinocytosis does not involve the concentration of surface receptors. Instead, large irregular endocytic vesicles are formed through actin-driven envaginations at the plasma membrane [108, 109]. The formation of these envaginations is typically driven by membrane ruffling at the cell surface, often stimulated by signals from growth factors such as EGF [101, 108]. During this ruffling process, actin drives

protrusions from the cell surface, which lengthen upon stimulation by growth factors and other signals before closing in on themselves as macropinosomes [108]. Lacking both coat proteins and surface receptors at high density, these macropinosomes can vary in diameter up to 5 μm; the large size of macropinosomes and their ability to effect significant fluid-phase endocytosis makes macropinocytosis an effective pathway for non-selectively internalizing large amounts of bulk macromolecules [100]. Following internalization of macropinosomes, actin dissociates from the vesicles, which can then experience different trafficking fates depending on cell type [110]. For instance, in macrophages these vesicles often acidify and merge with lysosomes, while in human A431 cells macropinosomes remain separate from the rest of the endocytic pathway [108, 110]. In part due to their size, macropinosomes are believed to be leakier vesicles compared to other endosomal compartments, which may enhance the escape of therapeutic particles internalizing into cells through this pathway [111, 112].

1.6—Overview of Thesis

This chapter gave an overview of cancer biology and treatments, a discussion on the CEACAM family of proteins, an introduction to Opacity proteins on *Neisseria* bacteria, and a discussion on liposomes and their use in therapeutic delivery, and proposed the investigation of Opa proteoliposomes for the purpose of cellular CEACAM targeting. Chapter 2 will discuss microscopy techniques to determine adhesion versus internalization of liposomes within model cell lines. Chapter 3 will discuss the role of CEACAM and Opa proteins in promoting proteoliposome uptake into cells. Chapter 4 will discuss additional considerations of Opa proteoliposome internalization, while Chapter 5 will discuss conclusions from this work and propose future directions.

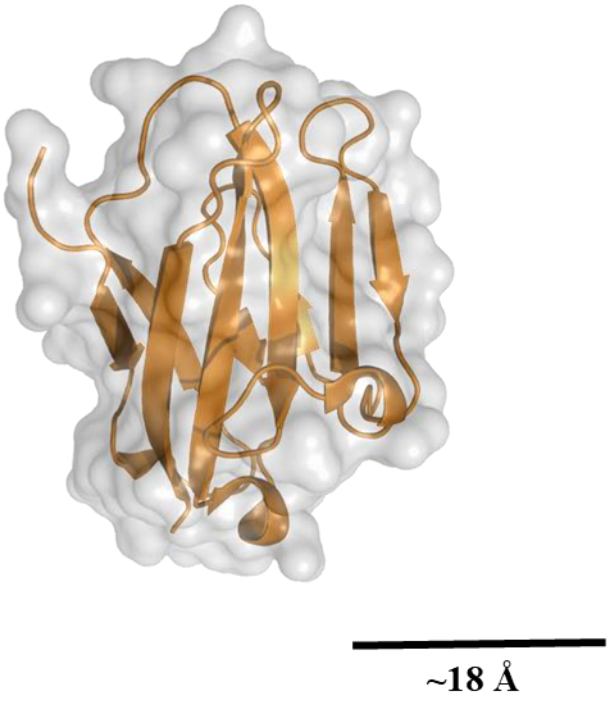

Figure 1. Structure of (IgV)-like CEACAM1 N-terminus. Ig-like fold showing sandwiched β-sheets of the N-terminus of CEACAM1 as a ribbon diagram (orange strands) within surface projection. (PDB ID: 2GK2) [113]

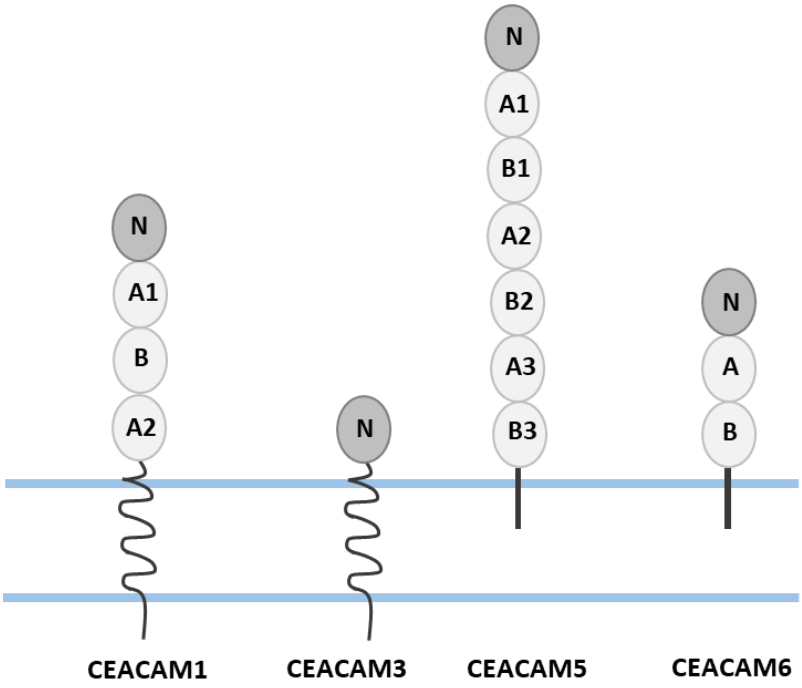

Figure 2. Domain organization and membrane anchors of CEACAM family members. CEACAM1, CEACAM3, CEACAM5, and CEACAM6 are example members of the CEACAM family of proteins. Each CEACAM contains an (IgV)-like variable N-terminus (dark grey), the major site of homo- and heterophilic binding. CEACAM proteins vary in their number of constant (IgC)-like domains (light grey), which come in two main types: the 93 residue A form and the 85 residue B form. CEACAM 1 and CEACAM3 both contain an alpha-helical transmembrane domain, with the Long form containing an ITIM for CEACAM1 and an ITAM for CEACAM3. CEACAM5 and CEACAM6 attach to the membrane (blue lines) through a GPI anchor. The four CEACAM proteins given here are all binding partners of Neisserial Opacity proteins.

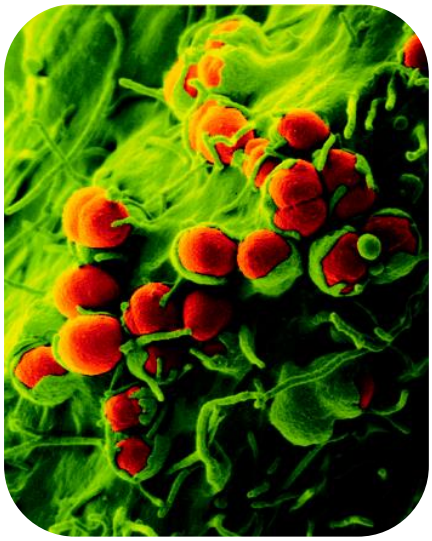

Figure 3. Scanning electron micrograph of *Neisseria gonorrhoeae* invading CEACAM+ human cells [47]. Human HeLa cells (green) transfected to overexpress CEACAM1 phagocytose *Neisseria gonorrhoeae* (red) displaying surface Opa proteins from *Billker et al (2002).* Membrane protrusions can be seen extending from the HeLa cells to envelop *N. gonorrhoeae*, a hallmark of phagocytosis.

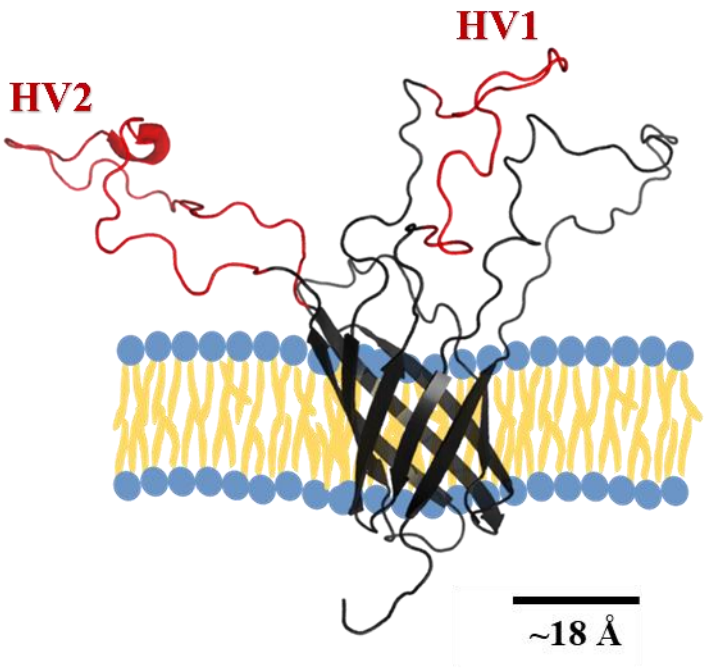

Figure 4. NMR-structure of Opa$_{60}$. The structure of Opa$_{60}$ solved by NMR shows an eight-stranded beta-barrel (black) with four extracellular loops embedded in a membrane (blue and yellow). Loops 2 and 3 contain hypervariable sequences 1 and 2 (red), which are the major determinants of target CEACAM binding. (PDB IDs: 2MLH, 2MAF) [53]

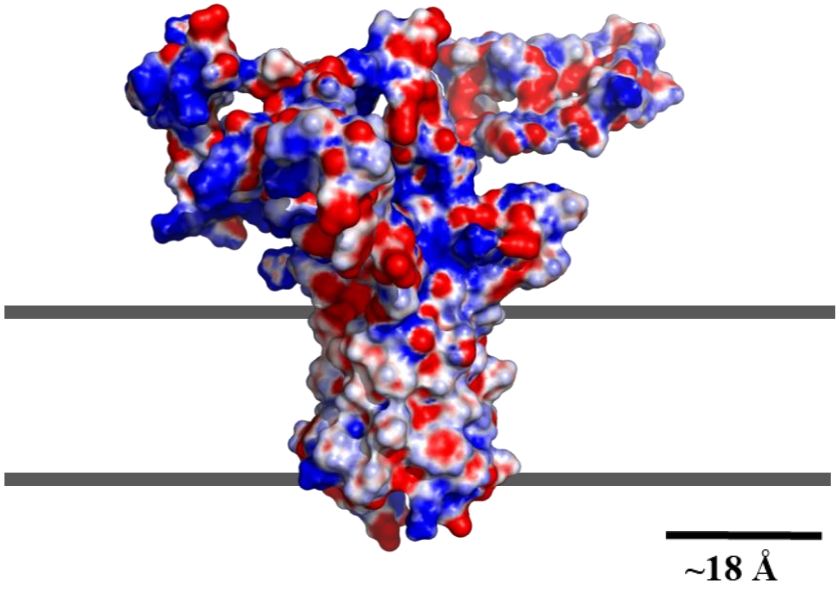

Figure 5. Electrostatic potential map of Opa$_{60}$. The Adaptive Poisson-Boltzmann Solver (APBS) in PyMol calculates the electrostatic potential on the molecular surface of Opa$_{60}$ (PDB IDs: 2MLH, 2MAF) [53]. Negative electrostatic potential is represented by increasing red, while increasing blue represents positive potential. The approximate positioning of Opa$_{60}$ within the membrane bilayer is depicted by horizontal grey lines, showing that the Opa$_{60}$ beta-barrel by its relative lack of red or blue is more nonpolar than its solvent-exposed loops.

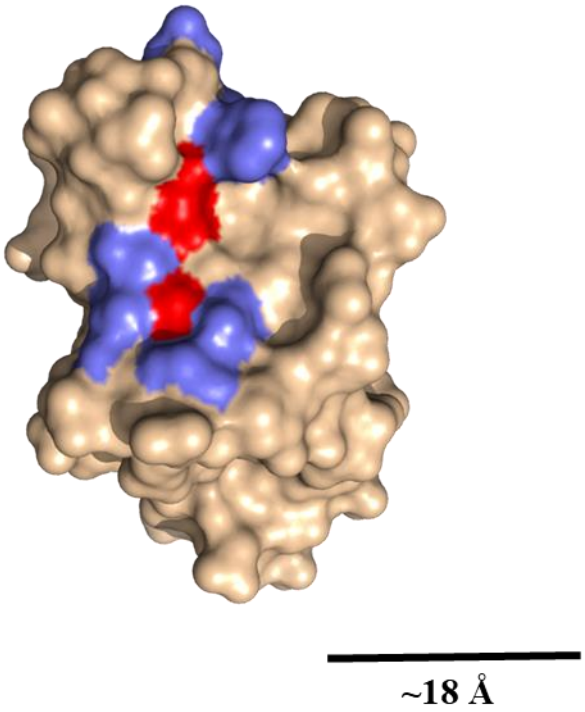

Figure 6. Opa-binding residues of CEACAM1 N-terminus. Surface representation of N-terminus of CEACAM1 with coloured Opa-binding residues. Residues in red (Tyr34 and Ile91) are involved in binding of all Opa proteins that bind CEACAM1. Residues in blue (Ser32, Val39, Gln44, Gln89) were shown to promote binding to some but not all CEACAM1-binding Opa proteins [63, 113]. (PDB ID: 2GK2)

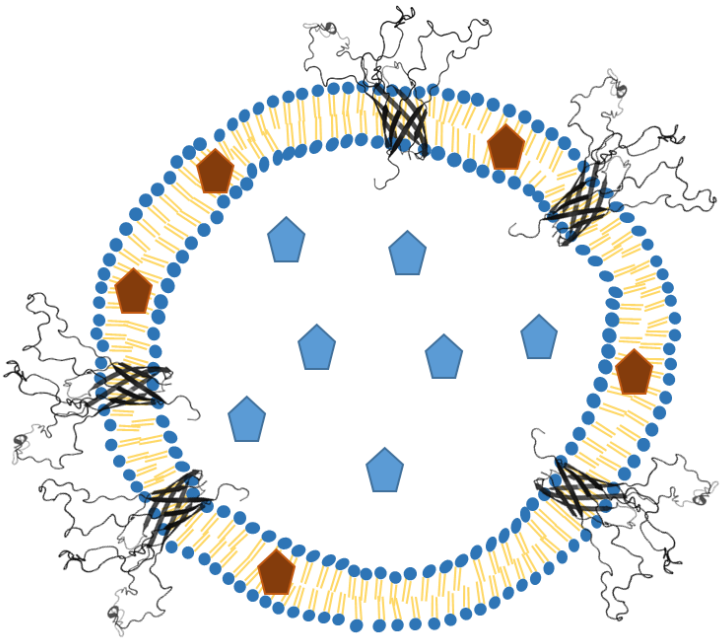

Figure 7. Cross-sectional illustration of proteoliposome. An illustrative cross-section of a hypothetical unilamellar liposome containing membrane proteins (here Opa_{60}, black) (PDB IDs: 2MLH, 2MAF). Hydrophobic compounds (brown pentagons) can partition into the nonpolar bilayer while water-soluble compounds (blue pentagons) can be entrapped within the aqueous interior.

1.7—References

1. *2005–2015 Database: National Program of Cancer Registries and Surveillance, Epidemiology, and End Results SEER*Stat Database: NPCR and SEER Incidence – USCS 2005–2015 Public Use Research Database.* Released June 2018.
2. Bertram, J.S., *The molecular biology of cancer.* Molecular Aspects of Medicine, 2000. **21**(6): p. 167-223.
3. Hanahan, D. and R.A. Weinberg, *The Hallmarks of Cancer.* Cell, 2000. **100**(1): p. 57-70.
4. Liu, P., et al., *Targeting the phosphoinositide 3-kinase (PI3K) pathway in cancer.* Nature reviews. Drug discovery, 2009. **8**(8): p. 627-644.
5. Curto, M., et al., *Contact-dependent inhibition of EGFR signaling by Nf2/Merlin.* The Journal of Cell Biology, 2007. **177**(5): p. 893-903.
6. Cory S, V.D., Strasser A, Harris AW, Adams JM., *Insights from Bcl-2 and Myc: malignancy involves abrogation of apoptosis as well as sustained proliferation.* Cancer Res., 1999 Apr.
7. Junttila, M.R., et al., *Selective activation of p53-mediated tumour suppression in high-grade tumours.* Nature, 2010. **468**(7323): p. 567-571.
8. Jafri, M.A., et al., *Roles of telomeres and telomerase in cancer, and advances in telomerase-targeted therapies.* Genome Medicine, 2016. **8**: p. 69.
9. Hanahan, D. and J. Folkman, *Patterns and Emerging Mechanisms of the Angiogenic Switch during Tumorigenesis.* Cell, 1996. **86**(3): p. 353-364.
10. Bai, F., et al., *Nanoparticle-mediated drug delivery to tumor neovasculature to combat P-gp expressing multidrug resistant cancer.* Biomaterials, 2013. **34**(26): p. 6163-6174.
11. Siemann, D.W., *The Unique Characteristics of Tumor Vasculature and Preclinical Evidence for its Selective Disruption by Tumor-Vascular Disrupting Agents.* Cancer treatment reviews, 2011. **37**(1): p. 63-74.
12. Berx, G. and F. van Roy, *Involvement of Members of the Cadherin Superfamily in Cancer.* Cold Spring Harbor Perspectives in Biology, 2009. **1**(6): p. a003129.
13. Cavallaro, U. and G. Christofori, *Cell adhesion and signalling by cadherins and Ig-CAMs in cancer.* Nature Reviews Cancer, 2004. **4**: p. 118.

14. Driver, B.R., et al., *Folate Receptor α Expression Level Correlates With Histologic Grade in Lung Adenocarcinoma.* Archives of Pathology & Laboratory Medicine, 2015. **140**(7): p. 682-685.
15. Cagle, P.T., et al., *Folate Receptor in Adenocarcinoma and Squamous Cell Carcinoma of the Lung: Potential Target for Folate-Linked Therapeutic Agents.* Archives of Pathology & Laboratory Medicine, 2012. **137**(2): p. 241-244.
16. Yang, C.-H., et al., *EGFR over-expression in non-small cell lung cancers harboring EGFR mutations is associated with marked down-regulation of CD82.* Biochimica et Biophysica Acta (BBA) - Molecular Basis of Disease, 2015. **1852**(7): p. 1540-1549.
17. Beauchemin, N. and A. Arabzadeh, *Carcinoembryonic antigen-related cell adhesion molecules (CEACAMs) in cancer progression and metastasis.* Cancer and Metastasis Reviews, 2013. **32**(3): p. 643-671.
18. Sadarangani, M., J. Pollard Andrew, and D. Gray-Owen Scott, *Opa proteins and CEACAMs: pathways of immune engagement for pathogenic Neisseria.* FEMS Microbiology Reviews, 2010. **35**(3): p. 498-514.
19. Pavlopoulou, A. and A. Scorilas, *A Comprehensive Phylogenetic and Structural Analysis of the Carcinoembryonic Antigen (CEA) Gene Family.* Genome Biology and Evolution, 2014. **6**(6): p. 1314-1326.
20. Kuespert, K., S. Pils, and C.R. Hauck, *CEACAMs: their role in physiology and pathophysiology.* Curr Opin Cell Biol, 2006. **18**(5): p. 565-71.
21. Thompson, J.A., *Molecular Cloning and Expression of Carcinoembryonic Antigen Gene Family Members.* Tumor Biology, 1995. **16**(1): p. 10-16.
22. Gold, P. and S.O. Freedman, *Demonstration of tumor-specific antigens in human colonic carcinoma by immunological tolerance and absorption techniques* The Journal of Experimental Medicine, 1965. **121**(3): p. 439.
23. Sarantis, H. and S.D. Gray-Owen, *Defining the Roles of Human Carcinoembryonic Antigen-Related Cellular Adhesion Molecules during Neutrophil Responses to Neisseria gonorrhoeae.* Infection and Immunity, 2012. **80**(1): p. 345-358.
24. Ergün, S., et al., *CEA-Related Cell Adhesion Molecule 1: A Potent Angiogenic Factor and a Major Effector of Vascular Endothelial Growth Factor.* Molecular Cell, 2000. **5**(2): p. 311-320.
25. Oh, P., et al., *Subtractive proteomic mapping of the endothelial surface in lung and solid tumours for tissue-specific therapy.* Nature, 2004. **429**: p. 629.

26. Kilic, N., et al., *Pro-angiogenic Signaling by the Endothelial Presence of CEACAM1*. Journal of Biological Chemistry, 2005. **280**(3): p. 2361-2369.
27. Soni, P., et al., *Cell Adhesion Properties and Effects on Receptor-Mediated Insulin Endocytosis Are Independent Properties of pp120, a Substrate of the Insulin Receptor Tyrosine Kinase.* Molecular Cell Biology Research Communications, 1999. **1**(2): p. 102-108.
28. Vaughn, D.E. and P.J. Bjorkman, *The (Greek) Key to Structures of Neural Adhesion Molecules.* Neuron, 1996. **16**(2): p. 261-273.
29. Klaile, E., et al., *The Cell Adhesion Receptor Carcinoembryonic Antigen-related Cell Adhesion Molecule 1 Regulates Nucleocytoplasmic Trafficking of DNA Polymerase δ-Interacting Protein 38.* Journal of Biological Chemistry, 2007. **282**(36): p. 26629-26640.
30. Klaile, E., et al., *The CEACAM1 N-terminal Ig domain mediates cis- and trans-binding and is essential for allosteric rearrangements of CEACAM1 microclusters.* The Journal of Cell Biology, 2009. **187**(4): p. 553-567.
31. Müller, M.M., et al., *Homophilic adhesion and CEACAM1-S regulate dimerization of CEACAM1-L and recruitment of SHP-2 and c-Src.* The Journal of Cell Biology, 2009. **187**(4): p. 569.
32. McCaw, S.E., E.H. Liao, and S.D. Gray-Owen, *Engulfment of Neisseria gonorrhoeae: Revealing Distinct Processes of Bacterial Entry by Individual Carcinoembryonic Antigen-Related Cellular Adhesion Molecule Family Receptors.* Infection and Immunity, 2004. **72**(5): p. 2742-2752.
33. Zhuo, Y., et al., *Glycosylation alters dimerization properties of a cell-surface signaling protein, CEACAM1*. Journal of Biological Chemistry, 2016.
34. Hammarström, S., *The carcinoembryonic antigen (CEA) family: structures, suggested functions and expression in normal and malignant tissues.* Seminars in Cancer Biology, 1999. **9**(2): p. 67-81.
35. Benchimol, S., et al., *Carcinoembryonic antigen, a human tumor marker, functions as an intercellular adhesion molecule.* Cell, 1989. **57**(2): p. 327-334.
36. Kobayashi, M., et al., *Carcinoembryonic antigen-related cell adhesion molecules as surrogate markers for EGFR inhibitor sensitivity in human lung adenocarcinoma.* British Journal of Cancer, 2012. **107**(10): p. 1745-1753.

37. Planque, C., et al., *Identification of Five Candidate Lung Cancer Biomarkers by Proteomics Analysis of Conditioned Media of Four Lung Cancer Cell Lines.* Molecular & Cellular Proteomics, 2009. **8**(12): p. 2746-2758.
38. Zhang, Y., et al., *CEACAM6 promotes tumor migration, invasion, and metastasis in gastric cancer.* Acta Biochimica et Biophysica Sinica, 2014. **46**(4): p. 283-290.
39. Chen, J.M., et al., *CEACAM6 induces epithelial-mesenchymal transition and mediates invasion and metastasis in pancreatic cancer.* International Journal of Oncology, 2013. **43**(3): p. 877-885.
40. Ordoñez, C., et al., *Human Carcinoembryonic Antigen Functions as a General Inhibitor of Anoikis.* Cancer Research, 2000. **60**(13): p. 3419.
41. Thies, A., et al., *CEACAM1 Expression in Cutaneous Malignant Melanoma Predicts the Development of Metastatic Disease.* Journal of Clinical Oncology, 2002. **20**(10): p. 2530-2536.
42. Dankner, M., et al., *CEACAM1 as a multi-purpose target for cancer immunotherapy.* OncoImmunology, 2017. **6**(7): p. e1328336.
43. Sienel, W., et al., *Elevated Expression of Carcinoembryonic Antigen-related Cell Adhesion Molecule 1 Promotes Progression of Non-Small Cell Lung Cancer.* Clinical Cancer Research, 2003. **9**(6): p. 2260.
44. Chen, Z., et al., *Carcinoembryonic Antigen-Related Cell Adhesion Molecule 1 Inhibits Proximal TCR Signaling by Targeting ZAP-70.* The Journal of Immunology, 2008. **180**(9): p. 6085.
45. Markel, G., et al., *CD66a Interactions Between Human Melanoma and NK Cells: A Novel Class I MHC-Independent Inhibitory Mechanism of Cytotoxicity.* The Journal of Immunology, 2002. **168**(6): p. 2803.
46. Dupuis, M.L., et al., *The Human Antibody Fragment DIATHIS1 Specific for CEACAM1 Enhances Natural Killer Cell Cytotoxicity Against Melanoma Cell Lines In Vitro.* Journal of Immunotherapy, 2015. **38**(9): p. 357-370.
47. Billker, O., et al., *Distinct mechanisms of internalization of Neisseria gonorrhoeae by members of the CEACAM receptor family involving Rac1- and Cdc42-dependent and -independent pathways.* The EMBO Journal, 2002. **21**(4): p. 560-571.
48. Dehio, C., S.D. Gray-Owen, and T.F. Meyer, *The role of neisserial Opa proteins in interactions with host cells.* Trends in Microbiology, 1998. **6**(12): p. 489-495.
49. Dehio, M., et al., *Vitronectin-dependent invasion of epithelial cells by Neisseria gonorrhoeae involves αv integrin receptors.* FEBS Letters, 1998. **424**(1-2): p. 84-88.

50. Merz, A.J. and M. So, *Interactions of Pathogenic Neisseriae with Epithelial Cell Membranes.* Annual Review of Cell and Developmental Biology, 2000. **16**(1): p. 423-457.
51. Chen, T., et al., *Adherence of pilus- Opa+ gonococci to epithelial cells in vitro involves heparan sulfate.* J Exp Med, 1995. **182**(2): p. 511-7.
52. Frits P. de Vries, R.C., Jacob Dankert, Matthias Frosch and Jos P. M. van Putten, *Neisseria meningitidis producing the Opc adhesin binds epithelial cell proteoglycan receptors.* Molecular Microbiology, 1998. **27**(6): p. 1203–1212.
53. Fox, D.A., et al., *Structure of the Neisserial Outer Membrane Protein Opa(60): Loop Flexibility Essential to Receptor Recognition and Bacterial Engulfment.* Journal of the American Chemical Society, 2014. **136**(28): p. 9938-9946.
54. Bhat, K.S., et al., *The opacity proteins of Neisseria gonorrhoeae strain MS11 are encoded by a family of 11 complete genes.* Molecular Microbiology, 1991. **5**(8): p. 1889-1901.
55. Hobbs, M.M., et al., *Recombinational reassortment among opa genes from ET-37 complex Neisseria meningitidis isolates of diverse geographical origins.* Microbiology, 1998. **144**(1): p. 157-166.
56. Rouphael, N.G. and D.S. Stephens, *Neisseria meningitidis: Biology, Microbiology, and Epidemiology.* Methods in molecular biology (Clifton, N.J.), 2012. **799**: p. 1-20.
57. Rahman, M.M., et al., *The membrane phospholipids of Neisseria meningitidis and Neisseria gonorrhoeae as characterized by fast atom bombardment mass spectrometry.* Microbiology, 2000. **146**(8): p. 1901-1911.
58. Kahler, C.M. and D.S. Stephens, *Genetic Basis for Biosynthesis, Structure, and Function of Meningococcal Lipooligosaccharide (Endotoxin).* Critical Reviews in Microbiology, 1998. **24**(4): p. 281-334.
59. Blake, M.S., et al., *Gonococcal opacity: lectin-like interactions between Opa proteins and lipooligosaccharide.* Infection and Immunity, 1995. **63**(4): p. 1434-1439.
60. Bilek, N., C.A. Ison, and B.G. Spratt, *Relative Contributions of Recombination and Mutation to the Diversification of the opa Gene Repertoire of Neisseria gonorrhoeae.* Journal of Bacteriology, 2009. **191**(6): p. 1878-1890.
61. Stern, A., et al., *Opacity genes in Neisseria gonorrhoeae: Control of phase and antigenic variation.* Cell, 1986. **47**(1): p. 61-71.

62. Bos, M.P., *Carcinoembryonic Antigen Family Receptor Recognition by Gonococcal Opa Proteins Requires Distinct Combinations of Hypervariable Opa Protein Domains.* Infection and Immunity, 2002. **70**(4): p. 1715-1723.
63. Virji, M., et al., *Carcinoembryonic antigens are targeted by diverse strains of typable and non-typable Haemophilus influenzae.* Molecular Microbiology, 2002. **36**(4): p. 784-795.
64. Swanson, J.A. and S.C. Baer, *Phagocytosis by zippers and triggers.* Trends in Cell Biology, 1995. **5**(3): p. 89-93.
65. Wang, J., et al., *Opa binding to cellular CD66 receptors mediates the transcellular traversal of Neisseria gonorrhoeae across polarized T84 epithelial cell monolayers.* Molecular Microbiology, 2002. **30**(3): p. 657-671.
66. Marqués-Gallego, P. and A.I.P.M. de Kroon, *Ligation Strategies for Targeting Liposomal Nanocarriers.* BioMed Research International, 2014. **2014**: p. 129458.
67. Nagayasu, A., K. Uchiyama, and H. Kiwada, *The size of liposomes: a factor which affects their targeting efficiency to tumors and therapeutic activity of liposomal antitumor drugs.* Advanced Drug Delivery Reviews, 1999. **40**(1): p. 75-87.
68. Allen, T.M. and P.R. Cullis, *Liposomal drug delivery systems: From concept to clinical applications.* Advanced Drug Delivery Reviews, 2013. **65**(1): p. 36-48.
69. Akbarzadeh, A., et al., *Liposome: classification, preparation, and applications.* Nanoscale Research Letters, 2013. **8**(1): p. 102-102.
70. Couvreur, P., *Nanoparticles in drug delivery: Past, present and future.* Advanced Drug Delivery Reviews, 2013. **65**(1): p. 21-23.
71. Sawant, R.R. and V.P. Torchilin, *Challenges in Development of Targeted Liposomal Therapeutics.* The AAPS Journal, 2012. **14**(2): p. 303-315.
72. Scindia, Y., et al., *Anti-Alpha 8 Integrin Immunoliposomes: A Novel System for Delivery of Therapeutic Agents to the Renal Glomerulus in Systemic Lupus Erythematosus.* Arthritis and rheumatism, 2008. **58**(12): p. 3884-3891.
73. Park, J.W., et al., *Anti-HER2 Immunoliposomes.* Clinical Cancer Research, 2002. **8**(4): p. 1172.
74. Shmeeda, H., et al., *Intracellular uptake and intracavitary targeting of folate-conjugated liposomes in a mouse lymphoma model with up-regulated folate receptors.* Molecular Cancer Therapeutics, 2006. **5**(4): p. 818.

75. Silvius, J.R., *Thermotropic Phase Transitions of Pure Lipids in Model Membranes and Their Modifications by Membrane Proteins*, in *Lipid-Protein Interactions*. 1982, John Wiley & Sons, Inc.: New York.
76. Coderch, L., et al., *Influence of cholesterol on liposome fluidity by EPR: Relationship with percutaneous absorption.* Journal of Controlled Release, 2000. **68**(1): p. 85-95.
77. Subczynski, W.K., et al., *High Cholesterol/Low Cholesterol: Effects in Biological Membranes: A Review.* Cell Biochem Biophys, 2017. **75**(3-4): p. 369-385.
78. Mainali, L., M. Raguz, and W.K. Subczynski, *Formation of Cholesterol Bilayer Domains Precedes Formation of Cholesterol Crystals in Cholesterol/Dimyristoylphosphatidylcholine Membranes: EPR and DSC Studies.* The journal of physical chemistry. B, 2013. **117**(30): p. 8994-9003.
79. Vorobyov, I. and T.W. Allen, *On the role of anionic lipids in charged protein interactions with membranes.* Biochimica et Biophysica Acta (BBA) - Biomembranes, 2011. **1808**(6): p. 1673-1683.
80. Guo, X., J.A. MacKay, and F.C. Szoka, *Mechanism of pH-Triggered Collapse of Phosphatidylethanolamine Liposomes Stabilized by an Ortho Ester Polyethyleneglycol Lipid.* Biophysical Journal, 2003. **84**(3): p. 1784-1795.
81. Koltover, I., et al., *An Inverted Hexagonal Phase of Cationic Liposome-DNA Complexes Related to DNA Release and Delivery.* Science, 1998. **281**(5373): p. 78-81.
82. Siegel, D.P. and R.M. Epand, *The mechanism of lamellar-to-inverted hexagonal phase transitions in phosphatidylethanolamine: implications for membrane fusion mechanisms.* Biophysical Journal, 1997. **73**(6): p. 3089-3111.
83. Dewald, A.H., J.C. Hodges, and L. Columbus, *Physical determinants of beta-barrel membrane protein folding in lipid vesicles.* Biophys J, 2011. **100**(9): p. 2131-40.
84. Martin, J.N., et al., *Neisserial Opa Protein–CEACAM Interactions: Competition for Receptors as a Means of Bacterial Invasion and Pathogenesis.* Biochemistry, 2016. **55**(31): p. 4286-4294.
85. Liu, D., A. Mori, and L. Huang, *Role of liposome size and RES blockade in controlling biodistribution and tumor uptake of GM1-containing liposomes.* Biochimica et Biophysica Acta (BBA) - Biomembranes, 1992. **1104**(1): p. 95-101.
86. Austin L. Bailey, P.R.C., *Membrane Fusion with Cationic Liposomes: Effects of Target Membrane Lipid Composition.* Biochemistry, 1997. **36**: p. 1628-1634.

87. Immordino, M.L., F. Dosio, and L. Cattel, *Stealth liposomes: review of the basic science, rationale, and clinical applications, existing and potential.* International Journal of Nanomedicine, 2006. **1**(3): p. 297-315.
88. Cattel, L., M. Ceruti, and F. Dosio, *From Conventional to Stealth Liposomes: a New Frontier in Cancer Chemotherapy.* Journal of Chemotherapy, 2004. **16**(sup4): p. 94-97.
89. Soundararajan, A., et al., *(186)Re-Liposomal Doxorubicin (Doxil): In Vitro Stability, Pharmacokinetics, Imaging and Biodistribution in a Head and Neck Squamous Cell Carcinoma Xenograft Model.* Nuclear medicine and biology, 2009. **36**(5): p. 515-524.
90. Tejada-Berges, T., et al., *Caelyx/Doxil for the treatment of metastatic ovarian and breast cancer.* Expert Review of Anticancer Therapy, 2002. **2**(2): p. 143-150.
91. Nakamura, Y., et al., *Nanodrug Delivery: Is the Enhanced Permeability and Retention Effect Sufficient for Curing Cancer?* Bioconjugate Chemistry, 2016. **27**(10): p. 2225-2238.
92. Greish, K., *Enhanced permeability and retention of macromolecular drugs in solid tumors: A royal gate for targeted anticancer nanomedicines.* Journal of Drug Targeting, 2007. **15**(7-8): p. 457-464.
93. Maeda, H., G.Y. Bharate, and J. Daruwalla, *Polymeric drugs for efficient tumor-targeted drug delivery based on EPR-effect.* European Journal of Pharmaceutics and Biopharmaceutics, 2009. **71**(3): p. 409-419.
94. Karanth, H. and R.S.R. Murthy, *pH-Sensitive liposomes-principle and application in cancer therapy.* Journal of Pharmacy and Pharmacology, 2010. **59**(4): p. 469-483.
95. Feng, L., et al., *The acidic tumor microenvironment: a target for smart cancer nano-theranostics.* National Science Review, 2018. **5**(2): p. 269-286.
96. Huth, U.S., R. Schubert, and R. Peschka-Suss, *Investigating the uptake and intracellular fate of pH-sensitive liposomes by flow cytometry and spectral bio-imaging.* J Control Release, 2006. **110**(3): p. 490-504.
97. Khalil, I.A., et al., *Uptake pathways and subsequent intracellular trafficking in nonviral gene delivery.* Pharmacol Rev, 2006. **58**(1): p. 32-45.
98. Allen, L.-A.H. and A. Aderem, *Mechanisms of phagocytosis.* Current Opinion in Immunology, 1996. **8**(1): p. 36-40.
99. Niedergang, F. and P. Chavrier, *Signaling and membrane dynamics during phagocytosis: many roads lead to the phagos(R)ome.* Current Opinion in Cell Biology, 2004. **16**(4): p. 422-428.

100. Conner, S.D. and S.L. Schmid, *Regulated portals of entry into the cell.* Nature, 2003. **422**: p. 37.
101. Nakase, I., et al., *Active macropinocytosis induction by stimulation of epidermal growth factor receptor and oncogenic Ras expression potentiates cellular uptake efficacy of exosomes.* Scientific Reports, 2015. **5**: p. 10300.
102. Takei, K. and V. Haucke, *Clathrin-mediated endocytosis: membrane factors pull the trigger.* Trends in Cell Biology, 2001. **11**(9): p. 385-391.
103. Ivaturi, S., et al., *Distribution of the LDL receptor within clathrin-coated pits and caveolae in rat and human liver.* Biochemical and Biophysical Research Communications, 2014. **445**(2): p. 422-427.
104. Liu, A.P., et al., *Local clustering of transferrin receptors promotes clathrin-coated pit initiation.* The Journal of Cell Biology, 2010. **191**(7): p. 1381-1393.
105. *Induction of mutant dynamin specifically blocks endocytic coated vesicle formation.* The Journal of Cell Biology, 1994. **127**(4): p. 915-934.
106. Zerial, M. and H. McBride, *Rab proteins as membrane organizers.* Nature Reviews Molecular Cell Biology, 2001. **2**: p. 107.
107. Maxfield, F.R. and T.E. McGraw, *Endocytic recycling.* Nature Reviews Molecular Cell Biology, 2004. **5**: p. 121.
108. Swanson, J.A. and C. Watts, *Macropinocytosis.* Trends in Cell Biology, 1995. **5**(11): p. 424-428.
109. Amyere, M., et al., *Constitutive Macropinocytosis in Oncogene-transformed Fibroblasts Depends on Sequential Permanent Activation of Phosphoinositide 3-Kinase and Phospholipase C.* Molecular Biology of the Cell, 2000. **11**(10): p. 3453-3467.
110. Meier, O., et al., *Adenovirus triggers macropinocytosis and endosomal leakage together with its clathrin-mediated uptake.* The Journal of Cell Biology, 2002. **158**(6): p. 1119-1131.
111. Wadia, J.S., R.V. Stan, and S.F. Dowdy, *Transducible TAT-HA fusogenic peptide enhances escape of TAT-fusion proteins after lipid raft macropinocytosis.* Nature Medicine, 2004. **10**: p. 310.
112. Imelli, N., et al., *Cholesterol Is Required for Endocytosis and Endosomal Escape of Adenovirus Type 2.* Journal of Virology, 2004. **78**(6): p. 3089-3098.
113. Fedarovich, A., et al., *Structure of the N-terminal domain of human CEACAM1: binding target of the opacity proteins during invasion of Neisseria meningitidis and*

N. gonorrhoeae. Acta Crystallographica Section D: Biological Crystallography, 2006. **62**(9): p. 971-979.

Chapter 2—Imaging liposomes to determine cell binding and internalization

2.1—Overview of detecting liposomes

2.1.1—Introduction to detection techniques

As detailed in the previous chapter, the overexpression of CEACAM proteins on certain cancers has led to an interest in targeting these markers for therapeutic delivery [1, 2]. Opa proteoliposomes were identified as a promising platform for therapeutic delivery based on the ability of Neisserial Opa proteins to bind and induce internalization of bacteria into cells using CEACAM proteins [3, 4]. To investigate this hypothesis, a strategy was sought to determine the best way to measure internalization of liposomes. In order to determine nanoparticle internalization into target cells, either direct or indirect methods may be employed.

Indirect measurements for particle internalization employ assays to screen for one or more cellular effects generated upon particle internalization. For example, internalization of liposomes containing a cytotoxic compound could be detected by measuring various signs of cellular cytotoxicity, such as DNA breakage [5], presence of phosphatidylserine on the outer leaf on the plasma membrane [6], or destabilization of electric potential in mitochondria [7]. Similarly, liposomes encapsulating siRNA could induce changes in RNA-transcription or protein expression levels upon internalization, which might be monitored using RT-PCR or Western blots [8]. Indirect detection methods for internalization therefore require not only particle internalization, but also internalized particles to exert productive cellular effects in sufficient quantity that they can be measured.

The direct detection of nanoparticle internalization involves tracking the internalization of the particles themselves rather than measuring effects exerted by these particles. Because of the small size of most nanoparticles, which precludes simple direct observation, special care must

often be taken to label nanoparticles so they can be visually tracked [9]. Methods commonly used to label liposomes include incorporation of radioisotopes for scintigraphic detection and imaging [10], incorporation of electron-rich compounds such as uranyl acetate for electron microscopy [11], and incorporation of fluorescent molecules for fluorescence microscopy [9, 12]. Of these techniques, fluorescence microscopy is currently widely-used for cell and particle imaging and is the technique utilized in the majority of this and following chapters.

2.1.2—Difficulties in determining internalized versus adhered particles

A major obstacle to investigating cell uptake of particles using microscopy is developing a method to determine whether particles are internalized or bound to the cell surface [13-16]. This determination is complicated by several factors: the roughness of the cell surface, the thickness of the plasma membrane (less than 5 nm) [17], and the frequently small size of the particles in comparison to cells (particle size varies but can range from several dozen nanometers for liposomes to several micrometers for bacteria).

A typical cell surface is remarkably heterogeneous and displays a variety of extracellular protein, lipid, and carbohydrate molecules [18, 19]. In addition to molecular heterogeneity, there exists structural and topological heterogeneity dictated by the architecture of the membrane itself[20]. This structural variation across the cell surface can result from ruffling of the membrane, including both protrusions from the membrane and pitted indentations into it. These structural heterogeneities are supported by various surface proteins as well as intracellular actin and microtubules [21-23]. For example, in clathrin-mediated endocytosis (CME), invaginations into the membrane called clathrin-coated pits are supported by assembly proteins such as clathrin, clathrin assembly lymphoid myeloid assembly protein, and AP2, and in some cells by intracellular actin [24-26]. These invaginations concentrate

ligands for internalization inside pits over 100 nm in diameter indented into the cell surface [24, 26]. Similarly, macropinosomes result from actin-generated protrusions from the cell membrane in a process called membrane ruffling. These extensions from the cell membrane drive the formation of macropinosomes up to 5 μm in diameter [24, 27].

Numerous factors can drive the formation of large-scale structures that cause significant variations within the topography across cell surfaces. These factors include cell type, composition of extracellular media (including osmotic gradients, nutrients, and growth factors), cell density, motility, and cell health, such as whether cells are cancerous [28, 29]. Many tumor cells, for instance, display high surface activity and numerous cell projections such as microvilli, membrane blebs, and surface ruffling which can contribute to tumor cell motility [30]. HeLa cervical cancer cells, for example, have been shown to form protrusions of several micrometers in order to increase interactions with neighbouring tumor cells [28].

The substantial architectural variation across the cell surface complicates the process of determining whether small particles are internalized. For instance, a surface-bound particle might be located substantially different distances away from the center of the cell depending on where on the membrane it is bound and whether the local membrane environment indents into the cell or protrudes away from it. In all cases surface-bound particles should be identified as extracellular regardless of different proximities to the cell center.

Further complicating the discernment between surface and intracellular particles is the relative thinness of the plasma membrane compared to a typical eukaryotic cell's size. Membrane thickness varies with lipid composition and presence of membrane proteins, but is approximately 3.5-4 nm [31], while eukaryotic cells often possess diameters of several micrometers. HeLa cells, for example, show diameters of around 20 μm, around 5000 times longer than the thickness of a typical single membrane. Because the plasma membrane is so

small compared to a cell's diameter, there can potentially be a very small spatial difference in fluorescence images between surface adhered and internalized particles relative to the size of the cell. Images at low resolution contain little spatial information regarding the separation of points of fluorescence, and imaging fluorescent particles at low resolution therefore complicates determining the exact spatial distribution of particles. Therefore, understanding the sensitivity and resolution of different fluorescence microscopes that may be used can give insight into accuracy of measurements based on collected images.

2.2—Overview of fluorescence microscopy

2.2.1—Introduction to fluorescence microscopy

Fluorescence microscopy enables the visualization of molecules using specific excitation and emission wavelengths of light. The basic principle of fluorescence involves electron excitation and relaxation following light absorption. Absorption of a photon by a molecule (termed the fluorophore) in the ground-state causes an electron to jump from its ground state into a singlet excited state where it resides for ~10^{-8} seconds (termed fluorescence lifetime) [32]. A fraction of the electron excitation energy is dissipated due to non-productive vibrational relaxation, causing the electron to fall to a lower energy level. In order to further relax back to its ground state, the remaining energy may be subsequently emitted as another photon. Because energy had been lost through vibrational relaxation, however, the emitted photon contains less energy than the excitation photon and consequently emits at a longer wavelength. Depending on fluorophore molecular structure, including extent and pattern of double bond conjugation, different fluorophores demonstrate different wavelengths of light at which they maximally absorb and emit light [32]. The shifting of photon emission to longer wavelengths compared to excitation light for a fluorophore is termed its Stokes' shift; this

Stokes' shift allows for fluorophores to be distinguished from excitation and background light, a task made easier with fluorophores that demonstrate a larger Stokes' shift [33].

The brightness of a fluorophore is dependent on several factors including its extinction coefficient (denoting likelihood to absorb photons), quantum yield (ratio of photons emitted/absorbed), fluorescence lifetime, solvent, fluorophore concentration, and intensity of excitation light . Importantly, fluorescence can often be inefficient, since fluorophores do not absorb every excitation photon encountered, nor do they exactly convert each photon absorbed to a photon emitted, and a number of pathways exist for absorbed energy to be lost through non-productive pathways (such as generation of heat). Therefore the relative intensity of fluorescence emission is frequently far lower (~10^{-5} to 10^{-6} times) than the exciting light [34]. Compounding the issue of dim fluorophores is the consideration that photon detection is also imperfect, and perhaps only as much as 30% of photons emitted through fluorescence may be collected by the detector [34]. Therefore, in order to increase fluorophore brightness to sufficient levels to enable detection, high intensity light sources are used to generate large numbers of excitation photons. Common light sources include mercury and xenon arc lamps which use direct current to ionize gas vapers, argon-ion lasers, and argon-krypton ion lasers. Arc lamps show intensity peaks at specific wavelengths of light, such as 406, 435, 546, and 578 nm for mercury lamps, which determines the wavelengths available for fluorophore excitation [34]. Upon photon emission from the light source, excitation light passes through a excitation filter in order to select for light of a specific wavelength. This filtered excitation light then interacts with a dichroic mirror angled 45 degrees to the oncoming light. Dichroic mirrors reflect light below a specific cut-off wavelength while passing longer-wavelength photons; in fluorescence microscopy, excitation light reflects off the angled dichroic mirror down 90 degrees onto the sample specimen, where it may excite fluorophores [34]. Following fluorescence emission from the sample, the

longer-wavelength, Stokes' shifted emission light now passes through the dichroic mirror instead of being reflected back toward the excitation light source. Emitted fluorescent photons pass through a suppression filter in order to filter out any remaining short-wavelength excitation light, before passing emitted photons onto the detector, which depending on the apparatus may be a photomultiplier tube (PMT) or CCD camera [34].

Because fluorescence microscopes must record fluorescence emission data within an image containing finite pixels, image resolution is an imperfect representation of the photon emission patterns of an actual specimen. Resolution refers to the minimum distance that two points must be separated in order for contrast to exist between them: this contrast is determined by number of emitted photons collected, the signal's dynamic range, and the number of pixels used to make the image [35]. Imaging a point light source produces a three-dimensional point-spread function in the imaging plane, which laterally is represented by the Airy pattern, a symmetric representation of the light-point pattern resulting from the diffraction of light as it passes through a circular aperture [36]. Airy patterns contain a central maximum and alternating minima and maxima of decreasing intensity as distance increases from the central maximum; when two point light-sources are close such that their Airy patterns overlap significantly, the two points are unable to be resolved [36]. Sufficient distance between two Airy patterns for distinct point-light sources enables the two points to be resolved; according to the Rayleigh criterion, this distance is sufficient when the first minimum of one Airy disk is aligned with the central maximum of the second (**Fig. 1**) [36]. The point distance between the central maximum and first minimum of two Airy patterns ($r_{lateral}$) can be estimated in widefield fluorescence microscopy by the following equation:

$r_{lateral} = 0.61\lambda/NA$ [37]

in which λ is the wavelength of emitted light and N.A. is the numeric aperture of the objective [37]. For a short-wavelength fluorophore emitting around 400 nm, imaged with a lens of N.A.=1.2, this correlates to a lateral resolution of approximately 200 nm, which is typically considered the best resolution that can be achieved with conventional fluorescence microscopy.

2.2.2—Confocal fluorescence microscopy

One of the drawbacks of fluorescence microscopy is that excitation light is not restricted to the desired focal plane, but in a three-dimensional specimen can interact with fluorophores above and below the plane of focus. The excitation of fluorophores out of the focal plane causes light emitted from these non-focal planes to reach the detector, which results in blurred fluorescence images and decreased image contrast, obscuring specimen details. Because the liposomes used in these experiments are small vesicles that range in size from only several dozen to a few hundred nanometers, good image-quality with high resolution is desirable in order to best visualize small punctae on and within cells. One method to improve image quality is with confocal microscopy, which uses a small pinhole aperture set between the specimen and the detector and which is conjugate with the specimen focal plane. This pinhole aperture, because it is conjugate with the focal plane, excludes out-of-focus background light while permitting light from the plane of focus to reach the detector, resulting in sharper images composed primarily of in-focus fluorescence [37].

Disadvantages to confocal microscopy compared to widefield fluorescence microscopy are increased scanning time and decreased signal light reaching the detector due to light exclusion by the pinhole screen. The decreased signal light often requires excitation lasers of higher intensities for confocal microscopy compared to widefield microscopy, as well as

longer scanning times, which can lead to fluorophore photobleaching and long data collection times, respectively.

Calculating resolution in the z-axis is more complicated than determining lateral resolution. Due to blurring from the point spread function/chromatic aberration, the vertical, or z-axial resolution in confocal microscopy is several times less than the resolution of the lateral x-y axis (typically no better than 800 nm) [38]. Increased resolution can be achieved in the vertical axis by using higher numeric aperture objectives and decreasing the pinhole diameter, although this has the drawback of excluding fluorescent signal from the detector and results in dimmer images [38]. Nonetheless, the exclusion of blurred, out-of-focus light in confocal microscopy enables the optical sectioning of samples, for which successive focal planes are imaged along the z-axis. These vertical sections can be recombined to generate three-dimensional cell images in order to analyse fluorescence signals from different, specific focal planes. This technique is discussed in more detail below.

2.2.3—Using confocal fluorescence microscopy to investigate proteoliposomal binding and uptake using HeLa cells

In order to investigate liposome internalization into target cells, a Zeiss LSM 700 confocal fluorescence microscope with a 63x Plan-Apochromat 1.4 N.A. oil objective was used to image Opa_{60}-containing proteoliposomes after exposure to HeLa cells. This strategy requires the fluorescence labelling of both liposomes and cells in order to better visualize both the small particles and cell membranes. Liposomes were labelled with 1,1’-Dioctadecyl-3,3,3’,3’-Tetramethylindocarbocyanine perchlorate (DiI), a lipophilic fluorophore that demonstrates low solubility and fluorescence in water, but high fluorescence and photostability in nonpolar environments such as the lipid bilayer [39]. The high lipophilicity

of the molecule leads to its being retained well within lipid membranes, in which the molecule diffuses laterally throughout the bilayer, and prevents DiI from being transferred between adjacent membranes except in cases of membrane fusion. Due to its lipophilic nature and high fluorescence, DiI has been used previously to determine cell-cell adhesion and fusion, lipid membrane diffusion, and lipoprotein labelling [39, 40]. Proteoliposomes containing folded Opa_{60} were formed using previously published protocols [4, 41] and labelled with 1 mol% DiI in order to fluorescently track the particles.

Model cell lines for which Opa proteoliposomes might bind and internalize, HeLa cells stably-transfected to express CEACAM1 or CEACAM3, as well as a transfection control line, were generously provided by the Gray-Owen lab from the University of Toronto. These transfected HeLa cervical cancer cells were used previously to demonstrate the CEACAM-dependent binding and internalization of Opa-expressing *Neisseria gonorrhoeae* as well as to investigate mechanisms of bacterial uptake with different CEACAM proteins [3]. Untransfected HeLa cells typically show little to no CEACAM expression as long as they are not kept too confluent or retained across too many passages, which is shown through Western blotting for CEACAM expression using a polyclonal pan-CEACAM antibody (Dako A0115) (**Figure 2A**). Therefore, HeLa cells in which CEACAM overexpression has been induced through stable transfection can be assumed to express entirely or nearly entirely a single CEACAM, as long as endogenous CEACAM expression of control cells is monitored and cell lines are discarded after around thirty passages.

In order to investigate confocal fluorescence microscopy as a tool to determine liposome internalization versus surface adhesion, a way to visualize the borders of the cell membrane must be determined. A pan-CEACAM antibody was found to give reasonable fluorescence staining of CEACAM1+ HeLa cells, but was unable to provide information about membrane borders in control cell lines not expressing CEACAM (**Figure 2B**). The method used to

visualise the membranes of control and transfected cell lines should be kept consistent in order to prevent differences in staining patterns, which may lead to differences in determining adhered versus internalized liposomes on different cell lines. Thus, other fluorescence methods were sought to better visualise the membranes of both transfected and control HeLa cell lines. A number of alternative membrane stains were investigated in both transfected and control HeLa cell lines, including Wheat Germ Agglutinin (WGA-647), Soy Bean Lectin (SBL-647), Deep Red CellMask (ThermoFisher C10046), a pan-cadherin antibody (CH-19), and an alpha 1 sodium potassium ATPase antibody (Na/K ATPase, Abcam Ab2867). These labelling strategies utilize diverse interactions between label and cell membrane in order to maximize possible opportunities to consistently label the surface of different HeLa lines. The pan-cadherin and Na/K ATPase antibodies, for instance, both target membrane proteins which are widely-expressed on epithelial cell surfaces. The cadherin superfamily is a widely-expressed family of transmembrane glycoproteins that regulate cell adhesion and tissue architecture [42]. Sodium-potassium ATPase, also widely-expressed on cells, is a surface complex which couples the hydrolysis of ATP to sodium-potassium exchange across the membrane, and is responsible for maintaining an electrochemical gradient that drives nutrient transport into cells [43]. Primary antibodies to these proteins are stained with a fluorescent secondary antibody. In contrast, WGA-647 and SBL-647 are fluorescently-tagged lectins that bind carbohydrate targets on the cell surface. WGA exists as a dimer in solution and selectively binds N-acetylglucosamine and N-acetylneuraminic (sialic) acid [44], while SBL exists as a tetramer and binds terminal N-acetylgalactosamine and galactopyranosyl residues [45]. Cell mask, unlike the other membrane stains, does not bind a specific membrane target, but instead is an amphipathic molecule that combines a lipophilic probe which inserts into the lipid bilayer with a negatively charged fluorophore that anchors the probe and enables

fluorescence imaging [46]. An amphipathic dye, CellMask tolerates fixation but not detergents and thus is not appropriate for experiments requiring cell permeabilization.

The quality and consistency of membrane staining was mixed for each stain tested. α-cadherin and α-Na^+/K^+ ATPase antibodies were found to give primarily punctate staining on the membranes of the tested HeLa cells and were thus deemed unsuitable for membrane visualization (data not shown). WGA, SBL, and CellMask gave strong fluorescence staining, and a range of concentrations and incubation times were tested to optimize membrane staining. Representative results for WGA-647, SBL-647, combined WGA and SBL, and Deep Red CellMask are shown below for CEACAM1+ Hela cells (**Figure 3**). Cells seeded onto acid-etched glass coverslips were fixed onto the coverslips using 4% paraformaldehyde (PFA) in phosphate-buffered saline (PBS) solution prior to labelling with WGA and SBL, while the staining protocol for CellMask required fixation after cell labelling. Imaging was carried out with the 63X 1.4 N.A. oil-objective on the Zeiss LSM 700 confocal fluorescence microscope. Cell nuclei were stained with DAPI, while the various membrane stains are shown in red due to the excitation and emission wavelengths of each stain being longer than 600 nm. In addition to the fluorescence channels, cells were also imaged using a differential interference contrast (DIC) channel, which uses polarized light to provide imaging and contrast to the cells separate from fluorescence channels. DIC works by transmitting through the sample polarized light which is split into mutually coherent parts. While traversing the sample, differences in the refractive index leads to differences in the optical path of the split polarized light parts, which upon being recombined prior to detection results in interference of the recombined light. As the plasma membrane alters the refractive index compared to the cytosol, the contrast at cell edges is enhanced upon illumination with DIC. Therefore, DIC imaging provides additional information about the cell surface and topology which can aid in determining borders of the cell membrane.

As shown in Figure 3, WGA, SBL, combined WGA and SBL, and CellMask were able to label cell membranes for CEACAM1+ HeLa cells. None of these labels were able to consistently label the membranes across all cells imaged, however, and even with significant effort put into optimizing the different staining protocols, each stain varied considerably in its labelling from cell to cell, with some cells showing high membrane labelling and others showing little at all. Additionally, cells whose membranes were successfully labelled still demonstrated low contrast between the intracellular compartment (which includes the cytosol, nucleus, and organelles) and the cell membrane, which is particularly evident in cells which demonstrate localization of red membrane stain with DAPI nuclear stain. This occurs most often in HeLa cells stained with WGA or WGA with SBL, less often with SBL alone, and almost not at all with CellMask. CellMask did, however, stain the body of HeLa cells much more strongly than it labelled protrusions and extensions from the cell body, such as membrane attachments to the glass coverslip or to other HeLa cells. As there is little space between the membrane stain and the nucleus, this pattern of staining makes it very difficult to visualize the cell cytosol, which is where internalized liposomes could be expected to end up. Similarly WGA appears to show high membrane staining close to the nucleus, with less intense and defined labelling near cell edges. SBL gives inconsistent staining but appears to provide more space between the edges of the membrane stain and the nucleus for several cells. WGA+SBL together show properties of both individual stains, with some cells showing reasonably sharp contrast near cell edges but also significant fluorescence near the nuclei that obscures their cytosolic compartments.

The body of a typical HeLa cell is approximately 20 μm in diameter, although this distance can increase when including protrusions and extensions that stretch out from the main body. These extensions from the cell are relatively flatter than the main body, which is approximately 5-10 μm thick in the z-axis. Thus, in order to account for particles throughout

the entirety of the cytosol, the cell can be imaged in several vertical sections. In order to investigate the utility of the above membrane stains in determining liposome internalization, DiI+ Opa_{60} proteoliposomes were exposed to CEACAM1+ HeLa cells, which were then fixed and their nucleus and membrane stained with DAPI and either SBL-647, WGA-647, or Deep Red CellMask. The cells were imaged in 1 μm sections throughout the entirety of their vertical axis, with example images of CEACAM1+ HeLa cells stained with SBL-647 shown below (**Figure 4A**). Liposomes appear as yellow punctae adhered either to the surface of the cells (outside the membrane stain), colocalized with the stain (either adhered externally or internalized), or are located well within the stain, suggesting internalization. As sections are imaged from the bottoms to tops of cells (representative images below organized 1-8 from bottom to top sections), individual cells typically show a wider base where extensions spread out and attach to the coverslip. As the focal plane progresses up the vertical axis, cell borders typically become rounder and smaller as the focal plane images through the cell body alone and excludes membrane protrusions involved in attachment. Within cells, as the focal plane cuts through the cell body, nuclei become visible before disappearing again once the top of the cell is reached; therefore, the presence of a well-defined, visible nucleus indicates that the focal plane is within this central cell body. Shown in **Figure 4B** is an enlarged single cell chosen from sections 1-7, with apparent internal and surface liposomes (green and purple arrows, respectively) indicated in different focal planes based on their relation to membrane stain and the nucleus. In section #6 the cell's nucleus is no longer visible, showing that this focal plane has progressed beyond the cell body and that the liposomes indicated with purple arrows are present among membrane stain and thus adhered to the surface rather than internalized. The green arrows in section #4 indicate liposomes within the borders of the membrane stain adjacent to a well-defined nucleus, suggesting that these particles were internalized within the cell. The relatively high number of liposomes clustered on top the cell

in section #6 shows that there may exist a large number of particles which are surface adhered, underscoring the importance of distinguishing these particles from internalized liposomes.

Once sections have been obtained throughout the full vertical span of all imaged cells, the different focal planes may be combined into a single image stack in order to better determine for each particle whether it is internalized or surface adhered (**Figure 5**). In order to set the x and y cross-sections, horizontal and vertical cross-lines (here shown in green, purple, grey) may be centered so that they intersect over specific liposomes (indicated by arrows) within a set focal plane defined by x and y axes. The z-stack for each x and y axis cross-section shows the chosen liposome (again indicated by colored arrows) at the intersection (x-z and y-z) of the green, purple, or grey x or y cross-section line and a blue line indicating the z-layer in the z-stack. Thus, particles are presumed internalized (green and grey in Figure 4) when located within the membrane stain in both the x-z and y-z dimensions, while particles (shown in purple) outside the membrane stain in these dimensions are considered adhered to the cell surface.

By analysing liposomal fluorescence in proximity to membrane stain, liposomes can be classified as either internal or surface. Nevertheless, this process is complicated by ambiguous and inconsistent membrane staining, a substantial investment of time needed for data collection and analysis resulting in limited data sets, and the possibility of subjectivity in defining liposomes as external or internal. Therefore, alternative approaches were considered to complement or even replace confocal fluorescence microscopy for cell analysis.

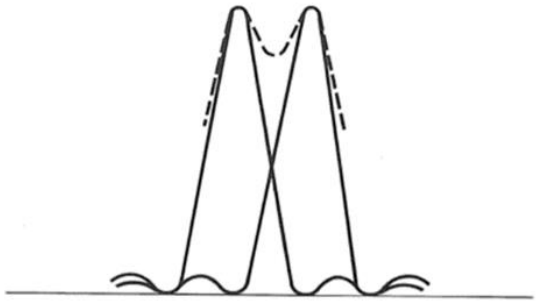

Figure 1. The Rayleigh criterion and resolution [36]. The Rayleigh criterion states that two points become resolved (dotted line) when the diffraction maximum of one overlaps with the diffraction minimum of the other (solid lines). Figure adapted from *Flay et al. (2012).*

A.

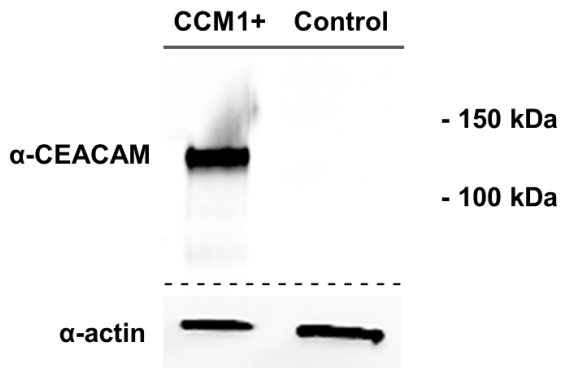

B.

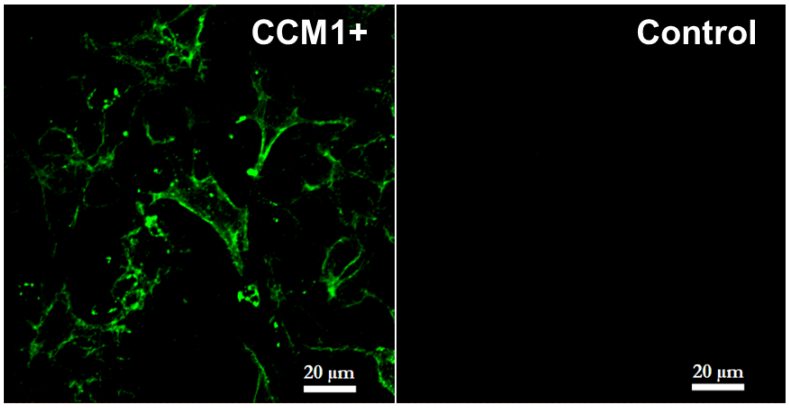

Figure 2. Validation of CEACAM1 expression on stably transfected cells compared to untransfected controls. (A) Western blot of cell lysate using a pan-CEACAM antibody shows high CEACAM expression at the correct molecular weight for CEACAM1 (~125 kDa) in HeLa cells stably transfected to express CEACAM1 and no expression in untransfected HeLa cells. (B) Confocal fluorescence imaging of adherent HeLa cells transfected to express CEACAM shows green CEACAM fluorescence at periphery of cells.

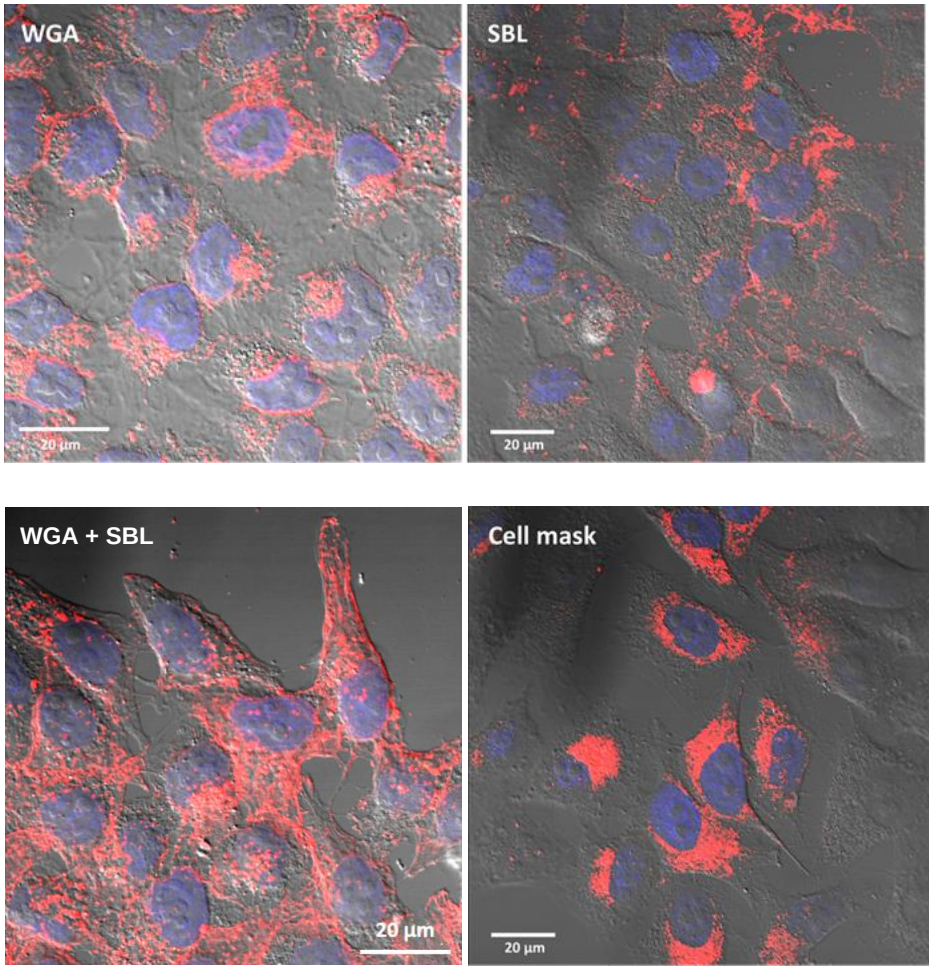

Figure 3. Representative images of different membrane stains with HeLa cells.

Representative images of CEACAM1+ HeLa cells stained with WGA-647, SBL-647 or Deep Red CellMask show variable quality membrane fluorescence. In each image, blue DAPI fluorescence shows nuclear stain, while the membrane stain is depicted as red fluorescence. Cells were additionally imaged with differential interference contrast (DIC) imaging to better visualize cell borders.

A.

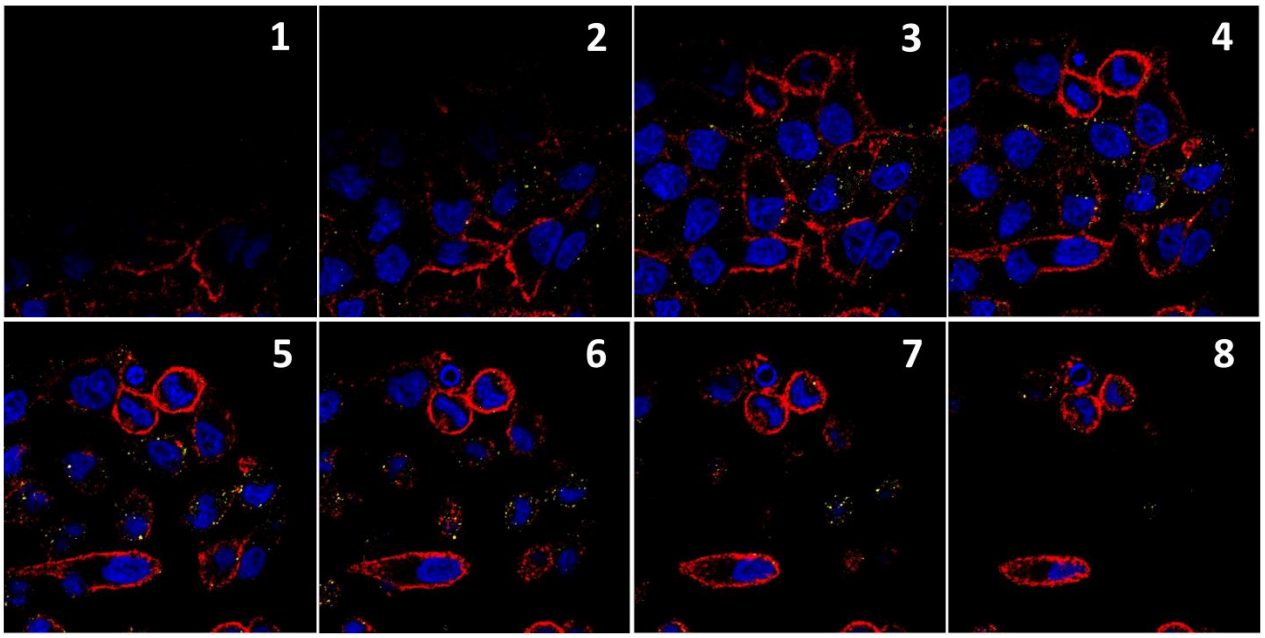

B.

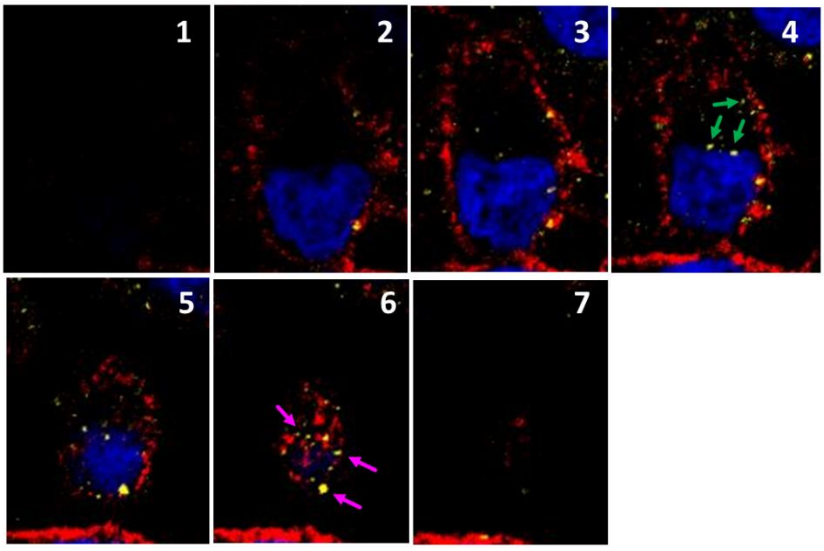

Figure 4. Imaging cells at varying focal planes along vertical axis. (A) CEACAM1+ HeLa cells stained with SBL-647 (red) and DAPI (blue) were exposed to Opa proteoliposomes (yellow). (B) Imaging through z-section of chosen cells enables identification of liposomes as being located within (green arrows) or outside of (purple arrows) the red membrane stain.

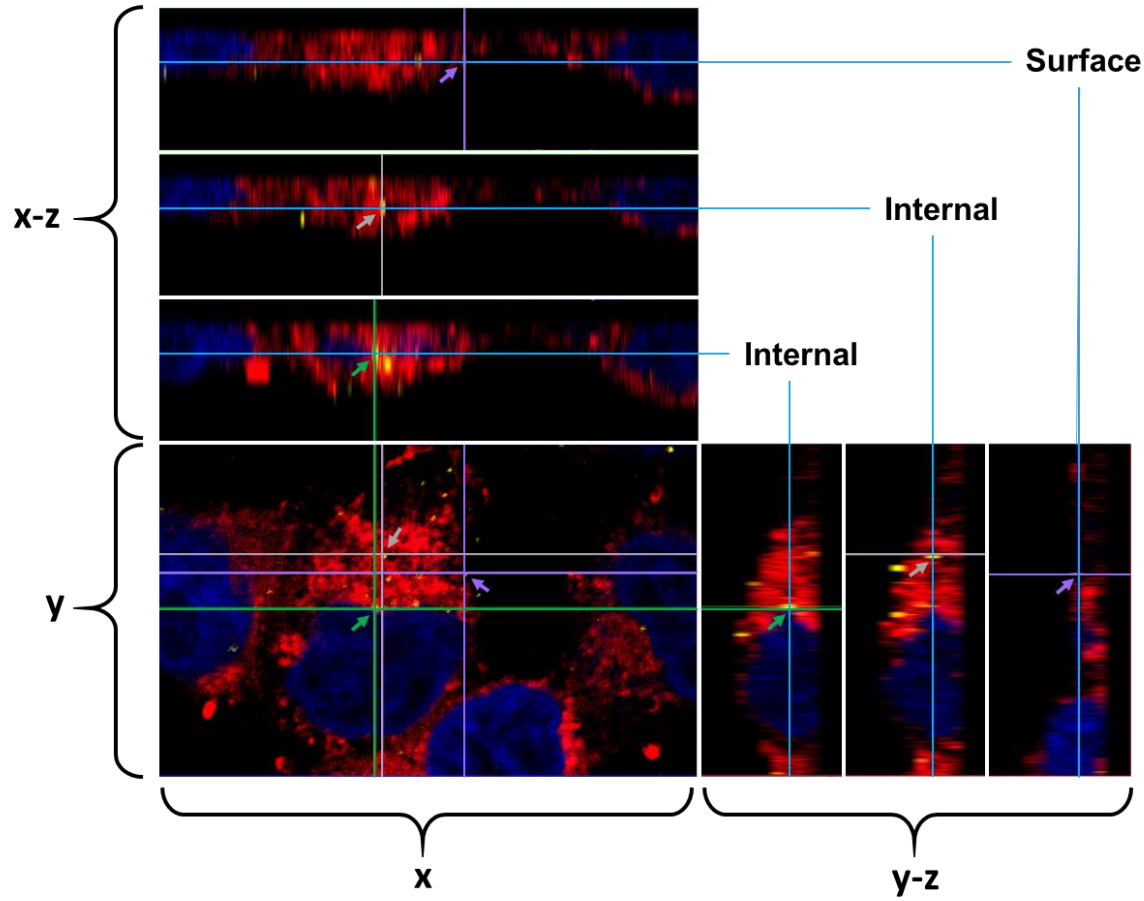

Figure 5. Determining particle internalization using stacked z-planes. Images acquired at different focal planes through z-axis can used to create a z-stack allowing analysis of individual puncta with relation to membrane fluorescence. Different layers of the image stack within the x-z and y-z axis can be represented and chosen punctae can be determined as internal (green or grey cross lines) or surface (purple cross lines) based on their localization within a membrane stain. Here, CEACAM1+ HeLa cells were stained with SBL-647 (red) and DAPI (blue) to image the membrane and nucleus, respectively.

2.3—Overview of Imaging Flow Cytometry

2.3.1—Introduction to Imaging Flow Cytometry (IFC)

The use of small apertures to block out-of-focus light in confocal fluorescence microscopy requires high laser intensities and long scan times with the use of high numeric apertures in order to maximize fluorophore excitation and photon detection [37, 38]. The significant amount of time required for data collection limits the number of cells that can reasonably be imaged to no more than a hundred per experimental condition, or even fewer if multiple focal planes are imaged throughout each cell, as is necessary to generate z-stacks. Further, a significant investment of time for data analysis, ambiguous membrane staining, and the possibility for subjectivity in data analysis prompted an investigation into alternative methods to image cells and liposomes.

Flow cytometry utilizes directed flow to move individual cells in suspension past an excitation/detection system which excites fluorophores and records fluorescence output for each cell. Conventional flow cytometers combine high fluorescence sensitivity (detecting as low as 100 fluorophores per cell) with an extremely high rate of data acquisition, reaching as high as tens of thousands of cells analysed per minute [47]. Unlike fluorescence microscopy, however, conventional flow cytometry sacrifices imaging capabilities, and thus spatial information of the fluorophore with relation to the cell is lost, making conventional flow cytometry of limited use in determining particle internalization. The recent development of multispectral Imaging Flow Cytometry (IFC), however, combines the imaging capabilities of fluorescence microscopy with the high-throughput data collection of conventional flow cytometry, enabling the collection of large data sets preserving spatial fluorescence information [47]. The imaging flow cytometers available at present are the Amnis ImageStream and EMD Millipore FlowSight [47, 48], with the ImageStreamX MarkII flow

cytometer by Amnis the instrument discussed here unless otherwise specified. Similar to conventional flow cytometers, IFC uses hydrodynamic focusing to flow single cells in a straight line past excitation lasers where the cells are trans-illuminated by the Brightfield light source and orthogonally illuminated by fluorescence excitation lasers [47]. Light from fluorescence excitation proceeds through a spectral decomposition element in which fluorescence emission light is split by wavelength into different angles and focused onto separate locations on CCD detectors [47]. Therefore, each cell can be represented by images containing fluorescence information of different wavelengths as well as side-scatter and transmitted Brightfield light, giving not just fluorescence information, but information on the cell's granularity (side-scatter) and size (forward scatter) [47].

IFC data from the Amnis ImageStreamX MarkII is processed using the Amnis IDEAS program, which compared to other flow cytometry analysis programs (such as CellProfiler and FCSExpress) enables more customizable masking methods and the ability to generate more varied analyses based on diverse criteria [48]. Fluorescence compensation is performed on all images in order to subtract spectral bleedthrough into other detection channels. The utility of IFC for determining cellular uptake of fluorescent proteoliposomes was investigated and compared to confocal fluorescence imaging.

2.3.2—Imaging Flow Cytometry: Ensuring quality data

As meaningful IFC fluorescence data is predicated on obtaining high-quality images of the cells, any investigation into particle internalization must include measures to ensure image quality. Flow cytometry provides certain challenges to obtaining high-quality images of cells that are non-existent in typical fluorescence microscopy due to the fact that in flow cytometry, suspended cells are in a state of constant flow prior to and during fluorescence

excitation and signal collection. The rate of flow must be kept at a speed high-enough to permit the rapid collection of fluorescence data while still enabling cell positioning within the focal volume of excitation lasers. Cells that deviate from expected positioning with relation to the excitation volume may appear blurred if they are too far back or forward when flowing past excitation lasers, or may even be partly out of the image frame. As IFC produces data collection for a large number of cells, many images may not meet quality standards and must be removed prior to data analysis. IFC uses gates in order to designate certain populations of cells based on analysis criteria, which enables the evaluation of each cell based upon various aspects of image quality. Important requirements to ensure quality images include that each analysed cell is in-focus and fully in the image, a single cell, and that the focal volume captures the center of the cell. In order to select cells that meet these criteria out of the total number of cells imaged (potentially many thousands or tens of thousands), gates are set to select cell populations based on Brightfield RMS Gradient, Brightfield Aspect Ratio and Area, and Nuclear staining (**Figure 6**) [49]. The initial criterion, Brightfield RMS Gradient, ensures that cells are focused by measuring the contrast of cell borders with the extracellular sheath flow medium; cells that are in-focus will have a defined, high-contrast border at their edges, while out-of-focus cells show blurriness at their edges. By measuring the Brightfield RMS Gradient across each image, blurriness manifests as a low value while sharp contrast results in a high value. Therefore a gate can be set to select cells with a high Brightfield RMS Gradient value (typically 50 or above, validated for cell focus by eye). Next, single cells are selected from the population of in-focus cells by analysing the Brightfield area with its aspect ratio. A Brightfield mask is applied to each cell image in order to cover the cell while excluding the extracellular volume, and the area and aspect ratio (a measure of its ellipticity or circularity) [49] are calculated for each cell. Multiple cells stuck together will typically show a high area compared to the general population as the mask will cover the clump of

cells as a single unit; therefore, it is best to exclude cells that are outside the majority population range for Brightfield area. Similarly, a high aspect ratio implies a cell is circular, as is expected for suspended HeLa cells, while low aspect ratios indicate elliptical cells and may imply either two cells adhered together or that a singlet cell was incompletely captured in the image. Finally, after focused, centered singlets have been selected out of the total population of imaged cells, a histogram of DAPI fluorescence intensity may be plotted in order to ensure the presence of a strongly-staining nucleus as weak or non-existent nuclear fluorescence may imply the focal volume is not centered within the cell or that the object imaged is not a stained cell at all. Typically 5000 cells are imaged per condition with approximately 2000 cells meeting criteria for in-focus, nucleated singlets. One consideration is whether this type of quality control could exclude cell populations of biological interest. In general, out of focus cells result from physical effects of the flow cytometer. The overexpression of surface adhesion molecules such as CEACAM1, however, could result in a higher propensity for cells to adhere. For this reason, cells are lifted by both chemical means and mechanical disruption in order to minimize cell clumping. Additionally, for experiments in which cell nuclear staining might be disrupted, such as after the delivery of the therapeutic compound doxorubicin, the step of gating on cells with DAPI fluorescence is skipped, since delivery of the compound could change DAPI staining and cells demonstrating these effects should still be analysed.

2.3.3—Imaging Flow Cytometry: Developing image masks to identify cell-surface from internalized fluorescence

Once images of high-quality have been selected, the cells can be analysed by a diverse set of criteria depending on the questions being asked. As the major question for this chapter is how

best to determine surface-bound from internalized particles, a method was sought to distinguish fluorescence from these two regions in IFC images. Amnis IDEAs software enables researchers to design a diverse array of novel masks and quantitative algorithms (called Features) in order to measure a large number of cell parameters [47]. Examples of parameters able to be measured in this way include fluorescence intensity, fluorescence area, spot count, fluorescence minima and maxima, fluorescence colocalization, among many others. Before any Feature is designed to quantitatively evaluate a particular parameter, such as intensity within a fluorescence channel, a mask must be designed and designated for that Feature. Image masks enable certain components of the cell image to be demarcated according to set criteria; if Features are the program instructions for what researchers want done, image masks are the markers designating where and to what components of the image each Feature will apply. A mask, for instance, may be defined in order to demarcate fluorescence intensity within a particular detector channel (for example, Channel 7, which includes DAPI emission, collects fluorescence signals emitted between 420-505 nm), while a separate mask may designate intensity within a different channel (for example, Channel 3, which collects fluorescence signal between 560-595 nm and includes DiI fluorescence emission). By using masks, different components of an image, such as separate fluorescence signals, can be defined and identified, enabling their quantification with a particular Feature. Developing a particular masking strategy can incorporate a number of criteria combined together in order to designate very specific image components for analysis; for example, a mask can be applied not just to fluorescence from a particular detector channel, but may incorporate spatial criteria, criteria for shapes, fluorescence intensity, colocalization, and many other variables. In this way, a mask could be used to designate fluorescence intensity of a specific detector channel that falls within a certain intensity range, or is located within a certain location of the cell, or even is located within or separate from a different mask

defining a different image component. Image masks define every component of what is measured, and the development of appropriate masking strategies is crucial to meaningful data analysis [48].

In order to distinguish internal from surface-bound particles, the most important criteria is defining these two spaces within cell images. The Brightfield channel is helpful in defining these regions within the image, as this channel contains information pertaining to cell size and basic topology. The Brightfield channel can even indicate the location and thickness of the plasma membrane as the difference in refractive index between the plasma or nuclear membrane compared to the cytosol and extracellular buffer can enable the visual demarcation of these bilayers when transmitted light passes through them [50]. In order to define an internal from external compartment for the cell, a Brightfield mask can be applied to the entirety of the cell starting at the plasma membrane; this mask can then be shrunk in order to exclude the membrane from this defined internal compartment. Several methods exist to shrink the Brightfield mask past the cell membrane, although the most useful are by manipulating the mask in order to Erode it in from the full Brightfield mask by a defined number of pixels (typically 4-5 pixels) [48], or by using Adaptive Erode in order to shrink the Brightfield mask to a defined percent of the original mask while retaining the original mask shape. Adaptive Erode in IDEAS was used instead of Erode because it better incorporates variations in cell shape as shown in the Brightfield channel and as picked up by the original Brightfield mask. In order to define internal from surface cell compartments, CEACAM1+ HeLa cells were detached with 2 mM EDTA in PBS and fixed in PFA before being stained by an anti-CEACAM antibody and counterstained by a secondary fluorescent antibody. Following staining, antibody fluorescence can be assumed to exist exclusively on the cell surface as these cells were not permeablized during the experiment, and therefore the internal cell compartment was unavailable for antibody binding. These cells can then be used to

validate Brightfield masks following various levels of Adaptive Erode being applied. For instance, an uneroded Brightfield mask will cover the entire cell as defined by its Brightfield image, and thus antibody fluorescence quantified using such a mask would count all of the surface-bound antibody within the mask; such a mask is therefore an inappropriate demarcation of internal fluorescence. As the Brightfield mask shrinks in, however, using the Adaptive Erode algorithm, the mask will include less area at the cell periphery; as the mask excludes more of the peripheral cell surface, the Adaptive Eroded mask becomes a more accurate definition of the internal compartment. Therefore the challenge becomes to define an internal mask that measures exclusively internal fluorescence (since counting surface fluorescence as internal fluorescence can generate false conclusions), without becoming too restrictive with defining the internal compartment and thereby excluding legitimate internal fluorescence from analysis. The analysis of surface antibody fluorescence was determined, therefore, using a range of Brightfield masks defined as a percent of the full Brightfield mask, ranging from 100% down to 75% Adaptive Erode of the full Brightfield mask (**Figure 7**). Once an internal mask is generated, a surface mask can be made by defining it as the area of the full Brightfield mask minus the area of the Adaptive Erode internal mask. Since antibody fluorescence on unpermeablized cells should be measured as entirely or nearly entirely at the cell surface, Adaptive Erode masks can be evaluated for their accuracy in defining an internal compartment.

The results indicate that the Brightfield mask that was most heavily Adaptive Eroded (75% of the full Brightfield mask) most accurately defines the internal compartment. Not surprisingly, the non-eroded Brightfield mask (100% of full mask) reports all antibody fluorescence as falling within the mask. As the mask is eroded inward and excludes more of the surface, the amount of antibody fluorescence counted within the internal mask decreases, with the most substantial decrease between the range of 90 to 80% Adaptive Erode. At the same time, the

antibody fluorescence counted as within the mask defined as the surface mask (full Brightfield minus the adaptive eroded internal mask) increases as the internal mask shrinks inward, reaching nearly 100% of antibody fluorescence accurately counted as surface fluorescence when the internal mask is defined as 75% Adaptive Erode of the full Brightfield mask. This result may seem overly stringent, as the membrane bilayer assuredly does not encompass the outer 25% of any HeLa cell, but the curvature of the cells and overflow of strong fluorescence signal into nearby pixels apparently necessitates tight masking. This result is similar to a previously reported study [48] in which the cellular internal compartment was defined as a 60% Adaptive Erode of the Brightfield mask. These results show that surface fluorescence can in fact overflow surprisingly far into cells, which may be a concern for studies using less restrictive internal masking (for example, using Erode to shrink the internal mask through the membrane in the Brightfield channel by only 4 pixels [51]), since surface fluorescence may be inaccurately counted as internalized. Importantly, the use of restrictive definitions when designing internal masks for experiments may result in true internalized fluorescence not being counted as internalized if it does not fall within the conservative 75% adaptive erode mask, since fluorescence outside the 75% adaptive mask could be either internal or surface fluorescence. Thus, quantification of internal fluorescence using a 75% adaptive erode mask may significantly underestimate true internal fluorescence if large amounts of true internal fluorescence fall outside the 75% adaptive erode mask. Underestimating internal fluorescence in this manner is necessary, however, in order to ensure that true surface fluorescence is not inaccurately counted as internalized.

In order to validate the developed masking strategy in the context of liposomes, CEACAM1+ HeLa cells were again lifted and fixed with 4% PFA before this time being exposed to Opa_{60} proteoliposomes containing DiI. As these cells were unpermeablized and fixed prior to liposome exposure, liposomes would be unable to internalize and should be entirely counted

as surface-bound. Similar to using the α-CEACAM antibody, liposomes on the surface of pre-fixed HeLa cells were falsely counted as internalized when the Brightfield mask was not sufficiently shrunk by Adaptive Erode, while an internal mask defined as 75% of the full Brightfield mask excluded nearly all surface fluorescence from being quantified as internal and was therefore determined to be the most accurate (**Figure 8**). Since liposomes should appear as fairly-bright punctae compared to their surroundings, the Adaptive Erode masks generated from the Brightfield image were combined with a mask to better exclude non-liposomal background fluorescence. The fluorescence intensity of each pixel in these images is defined as a value between 0-4095, so an Intensity Threshold mask was applied to the cells in order to only quantify fluorescence between 100-4095 for each pixel, which was determined to exclude background fluorescence. This Intensity Threshold mask was combined with the Internal or Surface masks so that both intensity and spatial criteria were met prior to quantification.

2.3.4—Imaging Flow Cytometry: Developing image masks for spot counting

While measuring fluorescence intensity is the most straightforward method to analyse liposomes in the context of HeLa cells, other strategies can also be informative and complement fluorescence quantification. For small fluorescent particles like liposomes, spot counting may serve to validate fluorescence intensity quantification and provide additional information [52]. Spot counting involves defining groups of adjacent pixels containing fluorescence as spots, which may indicate a single fluorescent particle or a cluster of particles (as may occur in endocytic vesicles such as lysosomes). Masks must be developed in order to define spots before they are counted. One complication in defining spots is in determining how to delineate spots when they exist as large patches of fluorescence within or on cells. To

this end, a basic bright spot mask (defining a spot as cluster of bright pixels compared to background) was combined with a peak mask in order to better define spots not just as bright areas against a dim background, but as clusters of bright pixels that may be surrounded by non-background fluorescence. For instance, three bright spots in close proximity to each other may appear to the eye as one large patch of fluorescence due to the overflow of each spot's fluorescence into neighbouring pixels. A peak mask, however, can be used to demarcate each spot individually [48]. The combination of a basic spot mask to identify clusters of bright pixels, with a peak mask, which enables identification of spots within patches of unbroken fluorescence, allows for sensitive spot quantification for each cell. It is important to validate that spot masks accurately identify individual punctae and that reported numbers of spots for cells match the best evaluation by eye. This was done for spot masks applied to the pre-fixed HeLa cells exposed to Opa proteoliposomes and spot counts were deemed to match visual evaluation (**Figure 9**). Upon developing a masking strategy to accurately count spots, spot masks were combined with internal and surface Brightfield masks in order to evaluate if changes in internal and surface spot count match the pattern seen with fluorescence intensity upon applying different Adaptive Erode masks. The results for internal and surface spot counts are in strong agreement with fluorescence measurements, with liposome spots being erroneously counted as internal when less stringent Adaptive Erode masks are used to define the internal compartment, while a 75% Adaptive Erode mask combined with spot and peak masks reports nearly all spots being surface-bound (**Figure 10**). Interestingly, unlike fluorescence intensity measurements, which altered not the total cellular DiI fluorescence intensity from one Adaptive Erode percent to another, but only the proportion of intensity defined between internal and surface compartments, it was discovered that varying the Adaptive Erode percent significantly alters not just the ratios of internal to surface spots, but also the total number of spots counted. For instance, when the internal

compartment is defined as 100, 95, or 75% of the full Brightfield mask, so that all or nearly all punctae are counted as internal (for 100, 95%) or surface (for 75%), the total number of spots counted is nearly the same for all three mask definitions. Between 90 and 80% Adaptive Erode, however, the total number of spots increases, with the highest number of spots counted when the internal mask is defined as 85% of the full Brightfield mask. This is likely due to the fact that within these ranges, spots that fall exactly on the demarcation line between internal and surface are likely split into two and assigned to both compartments, so that a single spot, half located within the internal mask and half located within the surface mask, might have these two arbitrary halves inaccurately counted as two separate spots. Another way of representing this data is shown in **Fig. 10B** which shows spots inaccurately counted as internalized for each adaptive erode mask as a percent of total spots counted within the population (approximately 6.8 spots per cell).

Because strong agreement exists between masking strategies which were used to quantify surface CEACAM antibody fluorescence, surface proteoliposome fluorescence, and liposome spot count, an Adaptive Erode mask set to 75% of the full Brightfield mask was determined with high confidence to quantify internal fluorescence accurately, while almost fully excluding surface fluorescence from analysis.

2.4—Comparison between applicability of confocal fluorescence microscopy and imaging flow cytometry for quantifying internalized versus surface-bound particles

Of the two techniques surveyed in this chapter, both confocal fluorescence microscopy and imaging flow cytometry are able to discriminate between internal and surface liposome particles within the context of transfected HeLa cells. Confocal fluorescence microscopy enables high-resolution imaging of a variety of focal planes spanning the full vertical axis of

HeLa cells. When combined with effective membrane stains, these images can be used to form z-stacks enabling individual fluorescent punctae to be analysed for localization within or adjacent to the cell membrane. Despite these powerful capabilities, significant difficulties in consistently staining cell membranes complicated imaging. As adherent HeLa cells lie relatively flat and extend large membrane protrusions for attachment to glass coverslips and adjacent Hela cells [28], liposomes are not necessarily localized exactly within or on the cell body, but can be attached to or internalized into these extensive protrusions. These projections from the cell body can be difficult to cleanly image using certain membrane stains. Finally, the significant amount of time required to obtain and analyse data, the limited number of cells that can be analysed in this fashion, and the potential for bias in determining liposome internalization suggested that alternative approaches to investigate internalization may be warranted.

In light of the many difficulties involved with confocal imaging, flow cytometry arose as an imaging alternative whose strengths addressed many of the difficulties encountered. Although the 60x, 0.9 NA objective of the ImagestreamX MarkII is slightly lower resolution than the 63x, 1.4 NA objective used to analyse cells with the Zeiss LSM 700 confocal microscope, the high-sample throughput and automated data analysis with IFC improved data collection and increased confidence in the meaningfulness of results. Further, the masking strategy to determine particle internalization was shown with fixed cells to work well with the Brightfield channel alone, which diminished the need to stain cells with membrane dyes. Therefore, with a clear and proven masking strategy to determine particle internalization, imaging flow cytometry was made the primary technique to investigate Opa proteoliposome binding and uptake into HeLa cells, which is the focus of the succeeding chapters.

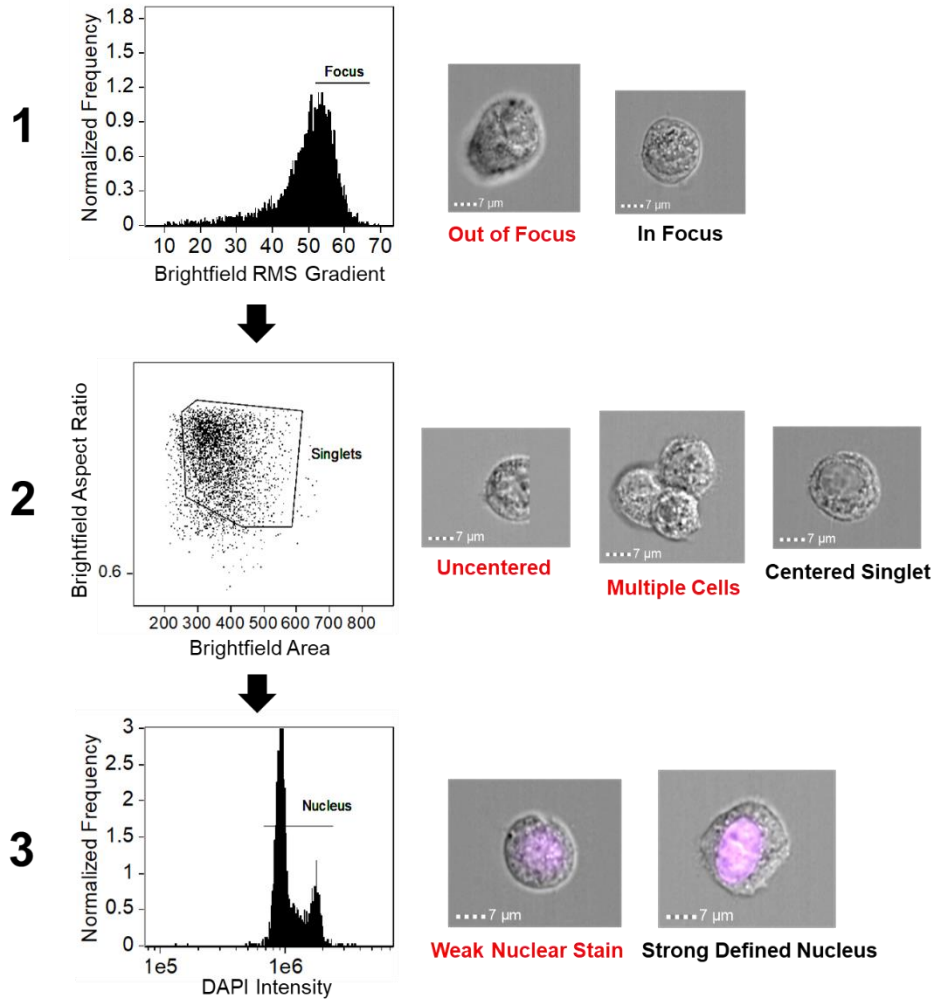

Figure 6. Gating strategy to select in-focus singlet cells. To ensure quality images, a gate is applied to the Brightfield Root Mean Square (RMS) Gradient, which measures contrast at cell edges, to select in-focus cells. Singlets are then selected from focused cells by plotting cell Aspect Ratio (measuring ellipticity) against cell Area (measuring size) in the Brightfield image, as single cells should be round and smaller than aggregated cells. Finally, nucleated singlets are selected by gating on DAPI fluorescence intensity. In images, cells are shown in Brightfield with nuclear DAPI staining depicted as purple fluorescence. Red text indicates examples of rejected cells.

A.

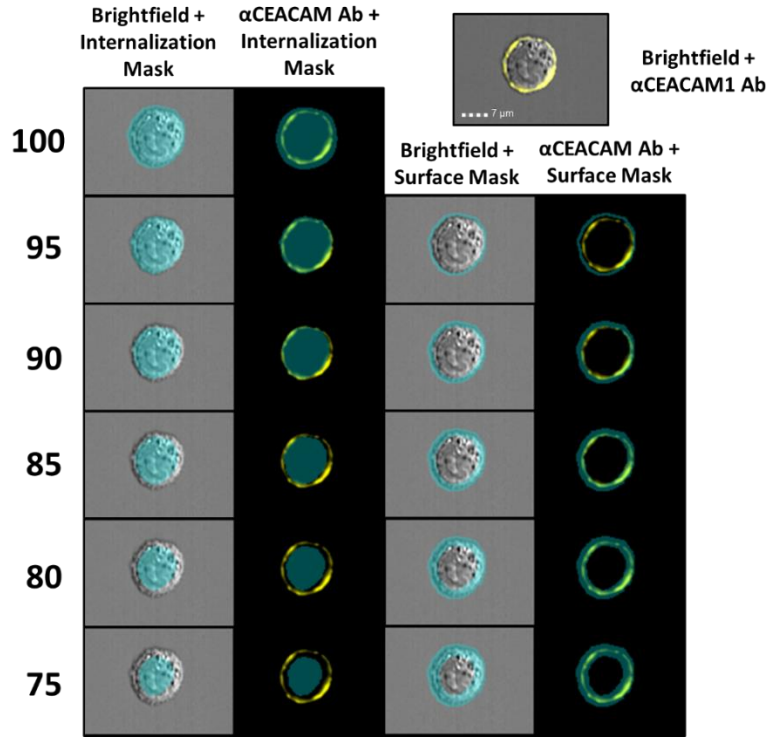

B.

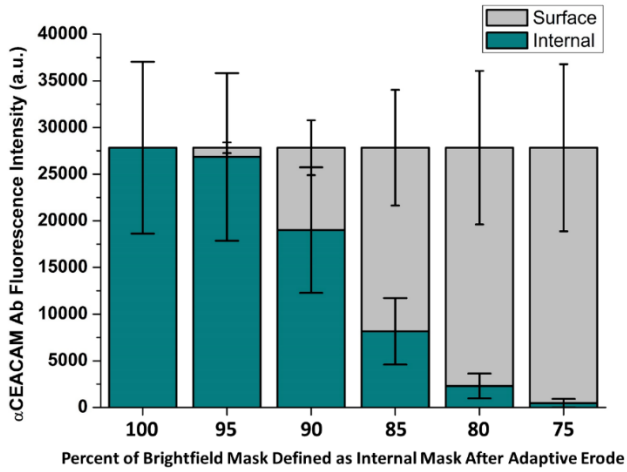

Figure 7. Masking strategy to measure surface antibody fluorescence. (A) Masks (blue) were designed to demarcate internal from surface cell compartments based on Adaptive Erode (100-75%) in the Brightfield channel and then validated by measuring the fluorescence of a surface CEACAM antibody (yellow). (B) Surface-fluorescence inaccurately measured as

internal fluorescence was lowest with a 75% adaptive erode Brightfield mask defining the internal compartment. Approximately 500 cells were analysed. Error bars represent 95% C.I.

A.

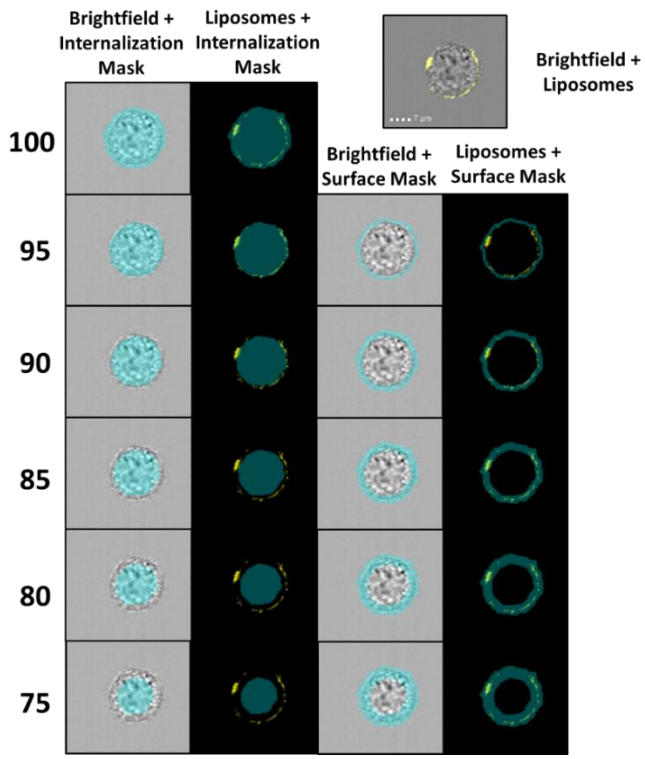

B.

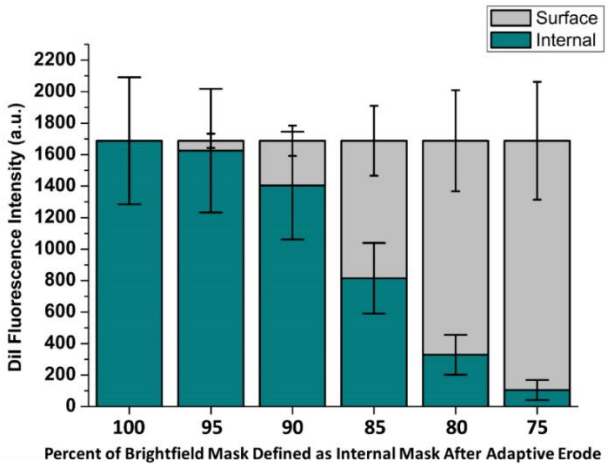

Figure 8. Masking strategy to measure surface liposome fluorescence. (A) As in Figure 6 above, masks (blue) demarcating internal and surface compartments were designed based on Adaptive Erode (100-75%) in the Brightfield channel and validated by measuring the fluorescence falsely-categorized as internal for surface fluorescent proteoliposomes (yellow)

given to pre-fixed HeLa cells. (B) A 75% adaptive erode mask resulted in the lowest levels of surface-fluorescence being called internal fluorescence. Error bars represent 95% C.I.

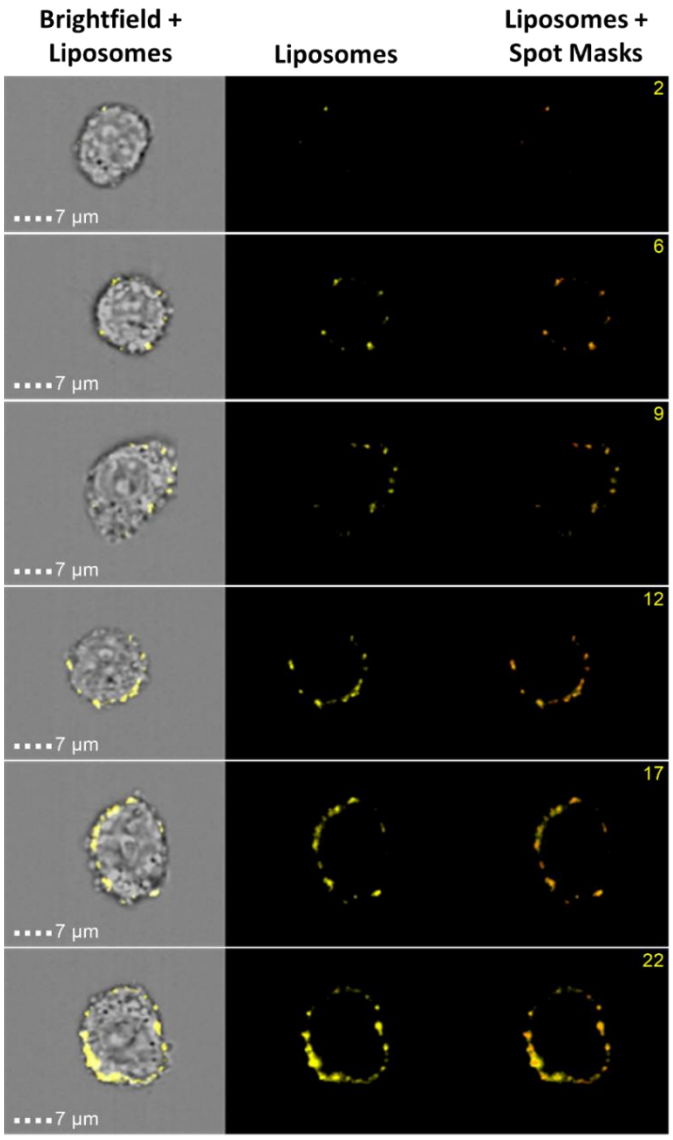

Figure 9. Validating spot masks and quantification of fluorescent punctae. In order to generate useful spot masks for accurate spot counting, masking (red) of spots representing proteoliposomes (yellow) can be validated by eye along with their quantification by a spot-count algorithm in IDEAS. Automated spot-counts match counts by eye, suggesting that spot masks and spot counts accurately quantify punctae.

A.

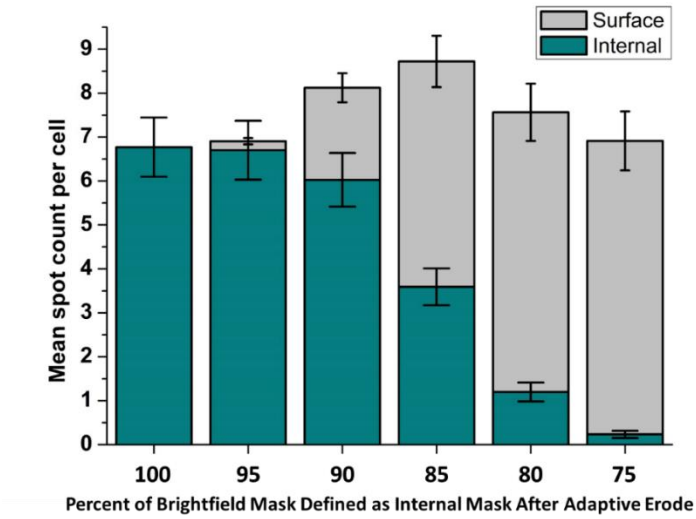

B.

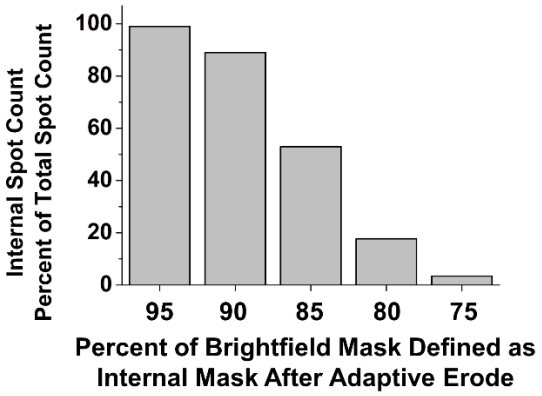

Figure 10. Validating masking strategy to measure surface liposome spot count. (A) In addition to validating internal and surface masks for surface-bound liposomal fluorescence intensity, a spot count algorithm can be applied to the different adaptive erode Brightfield masks (100-75%) demarcating internal and surface compartments of the cell. Adaptive Erode masks set to 75% of the full Brightfield mask accurately reflects low internalized and high surface particles. Error bars represent 95% C.I. (B) Alternatively, spots inaccurately counted as internal may be represented as a percent of the total spots for the population (approximately 6.8 spots per cell counted with 100% Brightfield masks).

2.5—References

1. Dankner, M., et al., *CEACAM1 as a multi-purpose target for cancer immunotherapy.* OncoImmunology, 2017. **6**(7): p. e1328336.
2. Hu, C.-M.J., et al., *Half-Antibody Functionalized Lipid-Polymer Hybrid Nanoparticles for Targeted Drug Delivery to Carcinoembryonic Antigen (CEA) Presenting Pancreatic Cancer Cells.* Molecular pharmaceutics, 2010. **7**(3): p. 914-920.
3. McCaw, S.E., E.H. Liao, and S.D. Gray-Owen, *Engulfment of Neisseria gonorrhoeae: Revealing Distinct Processes of Bacterial Entry by Individual Carcinoembryonic Antigen-Related Cellular Adhesion Molecule Family Receptors.* Infection and Immunity, 2004. **72**(5): p. 2742-2752.
4. Martin, J.N., et al., *Neisserial Opa Protein–CEACAM Interactions: Competition for Receptors as a Means of Bacterial Invasion and Pathogenesis.* Biochemistry, 2016. **55**(31): p. 4286-4294.
5. Ivashkevich, A., et al., *Use of the γ-H2AX assay to monitor DNA damage and repair in translational cancer research.* Cancer letters, 2012. **327**(1-2): p. 123-133.
6. Mariño, G. and G. Kroemer, *Mechanisms of apoptotic phosphatidylserine exposure.* Cell Research, 2013. **23**(11): p. 1247-1248.
7. Jo, W.-S., et al., *Loss of mitochondrial membrane potential and caspase activation enhance apoptosis in irradiated K562 cells treated with herbimycin A.* International Journal of Radiation Biology, 2005. **81**(7): p. 531-543.
8. Kim, H.-K., et al., *Enhanced siRNA delivery using cationic liposomes with new polyarginine-conjugated PEG-lipid.* International Journal of Pharmaceutics, 2010. **392**(1): p. 141-147.
9. Bibi, S., et al., *Microscopy imaging of liposomes: From coverslips to environmental SEM.* International Journal of Pharmaceutics, 2011. **417**(1): p. 138-150.
10. Boerman, O.C., et al., *Radiolabeled liposomes for scintigraphic imaging.* Progress in Lipid Research, 2000. **39**(5): p. 461-475.
11. Baxa, U., *Imaging of Liposomes by Transmission Electron Microscopy*, in *Characterization of Nanoparticles Intended for Drug Delivery*, S.E. McNeil, Editor. 2018, Springer New York: New York, NY. p. 73-88.
12. Deissler, V., et al., *Fluorescent Liposomes as Contrast Agents for In Vivo Optical Imaging of Edemas in Mice.* Small, 2008. **4**(8): p. 1240-1246.

13. Smirnov, A., et al., *High-Throughput Particle Uptake Analysis by Imaging Flow Cytometry.* Current Protocols in Cytometry, 2017. **80**(1): p. 11.22.1-11.22.17.
14. Lee, J.S., S.Y. Hwang, and E.K. Lee, *Imaging-based analysis of liposome internalization to macrophage cells: Effects of liposome size and surface modification with PEG moiety.* Colloids and Surfaces B: Biointerfaces, 2015. **136**: p. 786-790.
15. Ducat, E., et al., *Cellular uptake of liposomes monitored by confocal microscopy and flow cytometry.* Journal of Drug Delivery Science and Technology, 2011. **21**(6): p. 469-477.
16. Gottstein, C., et al., *Precise quantification of nanoparticle internalization.* ACS nano, 2013. **7**(6): p. 4933-4945.
17. Li, L.B., I. Vorobyov, and T.W. Allen, *The role of membrane thickness in charged protein–lipid interactions.* Biochimica et Biophysica Acta (BBA) - Biomembranes, 2012. **1818**(2): p. 135-145.
18. Sachs, J.N. and D.M. Engelman, *Introduction to the Membrane Protein Reviews: The Interplay of Structure, Dynamics, and Environment in Membrane Protein Function.* Annual Review of Biochemistry, 2006. **75**(1): p. 707-712.
19. Rauvala, H., *Cell surface carbohydrates and cell adhesion.* Trends in Biochemical Sciences, 1983. **8**(9): p. 323-325.
20. Gibson, W.T. and M.C. Gibson, *Chapter 4 Cell Topology, Geometry, and Morphogenesis in Proliferating Epithelia*, in *Current Topics in Developmental Biology*. 2009, Academic Press. p. 87-114.
21. Dominguez, R. and K.C. Holmes, *Actin Structure and Function.* Annual review of biophysics, 2011. **40**: p. 169-186.
22. Stephens, D.J., *Functional coupling of microtubules to membranes – implications for membrane structure and dynamics.* Journal of Cell Science, 2012. **125**(12): p. 2795.
23. Domínguez-Giménez, P., N.H. Brown, and M.D. Martín-Bermudo, *Integrin-ECM interactions regulate the changes in cell shape driving the morphogenesis of the Drosophila wing epithelium.* Journal of Cell Science, 2007. **120**(6): p. 1061.
24. Khalil, I.A., et al., *Uptake pathways and subsequent intracellular trafficking in nonviral gene delivery.* Pharmacol Rev, 2006. **58**(1): p. 32-45.
25. Ferguson, J.P., et al., *Mechanoregulation of clathrin-mediated endocytosis.* Journal of Cell Science, 2017. **130**(21): p. 3631.

26. Maib, H., E. Smythe, and K. Ayscough, *Forty years on: clathrin-coated pits continue to fascinate.* Molecular Biology of the Cell, 2017. **28**(7): p. 843-847.
27. Kerr, M.C., et al., *Visualisation of macropinosome maturation by the recruitment of sorting nexins.* Journal of Cell Science, 2006. **119**(19): p. 3967.
28. Knyrim, K. and N. Paweletz, *The formation of contacts between HeLa cells.* Virchows Archiv B, 1978. **28**(1): p. 243-254.
29. Ron, A., et al., *Cell shape information is transduced through tension-independent mechanisms.* Nature Communications, 2017. **8**(1): p. 2145.
30. Yilmaz, M. and G. Christofori, *Mechanisms of Motility in Metastasizing Cells.* Molecular Cancer Research, 2010. **8**(5): p. 629.
31. Mitra, K., et al., *Modulation of the bilayer thickness of exocytic pathway membranes by membrane proteins rather than cholesterol.* Proceedings of the National Academy of Sciences, 2004. **101**(12): p. 4083-4088.
32. Shashkova, S. and Mark C. Leake, *Single-molecule fluorescence microscopy review: shedding new light on old problems.* Bioscience Reports, 2017. **37**(4): p. BSR20170031.
33. al, M.V.S.e., *Fluorescent dyes with large Stokes shifts for super-resolution optical microscopy of biological objects: a review.* Methods Appl. Fluoresc., 2015. **3**.
34. Spring, K.R., *Fluorescence Microscopy.* Encyclopedia of Optical Engineering, 2003.
35. Sluder, G. and J.J. Nordberg, *Microscope Basics*, in *Methods in Cell Biology*, L. Wilson and P. Matsudaira, Editors. 2003, Academic Press. p. 1-10.
36. Flay, N. and R. Leach, *Application of the optical transfer function in X-ray computed tomography – a review*. 2012.
37. C.J.R. Sheppard, D.M.S., *Confocal Laser Scanning Microscopy.* BIOS Scientific Publishers, 1997.
38. Gary C. Sieck, C.B.M., and Y. S. Prakash *Volume Measurements in Confocal Microscopy* Methods in Enzymology, 1999. **307**: p. 296-315.
39. Majkowski, M., et al., *Alternation of Fluorescent Spectra of Membrane Markers DiI C18(3) and DiI C18(5) Evoked by Laser Illumination.* Journal of Histochemistry and Cytochemistry, 2012. **60**(10): p. 789-791.
40. Li, Y., et al., *Direct labeling and visualization of blood vessels with lipophilic carbocyanine dye DiI.* Nature protocols, 2008. **3**(11): p. 1703-1708.
41. Dewald, A.H., J.C. Hodges, and L. Columbus, *Physical determinants of beta-barrel membrane protein folding in lipid vesicles.* Biophys J, 2011. **100**(9): p. 2131-40.

42. Ramsey A. Foty, M.S.S., *Cadherin-mediated cell-cell adhesion and tissue segregation in relation to malignancy.* Int. J. Dev. Biol., 2004. **48**: p. 397-409.
43. Aperia, A., et al., *Na+-K+-ATPase, a new class of plasma membrane receptors.* American Journal of Physiology-Cell Physiology, 2016. **310**(7): p. C491-C495.
44. Schwefel, D., et al., *Structural Basis of Multivalent Binding to Wheat Germ Agglutinin.* Journal of the American Chemical Society, 2010. **132**(25): p. 8704-8719.
45. Reuben Lotan, H.W.S., Halina Lis, Nathan Sharon, *Subunit Structure of Soybean Agglutinin.* Journal of Biological Chemistry, 1973. **249**(4): p. 1219-1224.
46. Viola Mönkemöller, M.S., Peter McCourt, Karen Sørensen, Bård Smedsrød, Thomas Huser, *Imaging fenestrations in liver sinusoidal endothelial cells by optical localization microscopy* The Royal Society of Chemistry, 2013.
47. Basiji, D.A., et al., *Cellular Image Analysis and Imaging by Flow Cytometry.* Clinics in laboratory medicine, 2007. **27**(3): p. 653-viii.
48. Dominical, V., L. Samsel, and J.P. McCoy, *Masks in imaging flow cytometry.* Methods, 2017. **112**: p. 9-17.
49. Stanley Poh, E.P., Louis Tong, *Quantitative Image Analysis of Cellular Morphology Using Amnis® Imagestreamx Mark II Imaging Flow Cytometer: A Comparison against Conventional Methods.* Journal of Single Cell Genomics & Proteomics, 2015.
50. Dimopoulos, S., et al., *Accurate cell segmentation in microscopy images using membrane patterns.* Bioinformatics, 2014. **30**(18): p. 2644-2651.
51. Jenner, D., et al., *Using multispectral imaging flow cytometry to assess an in vitro intracellular Burkholderia thailandensis infection model.* Cytometry Part A, 2016. **89**(4): p. 328-337.
52. Franzen, C.A., et al., *Characterization of Uptake and Internalization of Exosomes by Bladder Cancer Cells.* BioMed Research International, 2014. **2014**: p. 11.

Chapter 3—Investigating liposome interactions with CEACAM+ HeLa cells

3.1—Introduction to question

Upon selecting imaging flow cytometry as the primary technique to investigate Opa-proteoliposome/CEACAM interactions, a method was developed to determine internal versus surface-adhered liposomes. The development of internal and surface cell masks allows us to identify with confidence internalized from surface-bound liposomes and enables the investigation of liposome and cell interactions. Using this method, two major questions are investigated in this chapter: do Opa proteins promote proteoliposome internalization into cells, and how are cellular interactions of proteoliposomes mediated by CEACAM?

3.2—HeLa model cell line

3.2.1—Considerations of choosing HeLa cell line

Early experiments looking at Opa proteoliposome interactions with CEACAM+ HeLa cells involved using three different types of cells. First, HeLa cells were provided by the lab of Scott Gray-Owen at the University of Toronto, which were stably-transfected to express recombinant CEACAM1, CEACAM3, CEACAM5, CEACAM6, CEACAM8, as well as a vector control line which does not overexpress CEACAM [1]. Secondly, HeLa CCL-2 cells were procured from ATCC and, using lipofectamine, were transiently transfected in-house with pMSCV plasmids coding for the above CEACAMs, as well as an empty pMSCV plasmid for vector control. These plasmids were also provided by the Gray-Owen lab. Successful transfections were selected for using puromycin dihydrochloride. Thirdly, Chinese Hamster Ovary (CHO) cells were transfected with the same pMSCV plasmids and selected for with puromycin as well. With a focus on testing Opa_{60} proteoliposome interactions in cells expressing CEACAM1 compared to vector control cells, the transiently-transfected

HeLa and CHO cells resulted in significantly lower α-CEACAM antibody staining and lower Opa proteoliposome fluorescence values compared to the stably-transfected HeLa cells (data not shown). Stably-transfected HeLa cells were selected as the primary cells for proteoliposome experiments, due in part to their higher α-CEACAM staining and Opa proteoliposome fluorescence values, as well as due to the desire to compare liposome binding and internalization results with previously-published results investigating *Neisseria gonorrhoea* interactions, which were carried out in the same stably-transfected HeLa cell lines [1]. An important consideration for working with these cells was the level and consistency of CEACAM expression across the cell lines that would be tested, including CEACAM1, CEACAM3, and control cells. As expected, staining of CEACAM1+ and CEACAM3+ HeLa cells resulted in higher α-CEACAM antibody fluorescence values compared to control cells, with CEACAM1+ cells giving average fluorescence values approximately 4.3 times higher than the antibody staining of control cells, and CEACAM3+ cells giving fluorescence values approximately 1.85 times higher than control values (**Fig. 1**). Despite these differences in relative values, the higher antibody staining present on CEACAM1+ cells compared to CEACAM3+ cells may not fully indicate higher CEACAM expression levels, but may result in part from differences in antibody affinity for the two CEACAM types. CEACAM1+ HeLa cells resulted as well in broader staining than CEACAM3+ cells, with some CEACAM1+ cells showing a surface CEACAM staining intensity comparable to CEACAM3+ cells, and some CEACAM1+ cells showing considerably higher α-CEACAM fluorescence staining. Growth conditions for the HeLa cells can affect expression levels of different CEACAMs, as CEACAM1+ HeLa cells can decrease CEACAM expression when they are kept at high confluence for extended periods of time, while control cells may begin to express CEACAM on their surface when kept too confluent (data not shown). Thus, in order to ensure consistent CEACAM expression for all cell lines,

HeLa cells are split before reaching 80% confluence and cells are discarded after they reach 25 passages.

3.2.2—Validating HeLa lines with *E. coli* expressing OpaI

In order to validate that the model HeLa lines performed as expected, stably-transfected CEACAM1+, CEACAM3+, and control HeLa cells were incubated with BL21 (DE3) *Escherichia coli* cells transformed with a pEX plasmid coding for either MS11 OpaI or an empty control plasmid. Cells were grown under selection with ampicillin but without protein induction in order to prevent over-expression of Opa proteins. In addition, DiI was included in the LB media to enable its incorporation into cell membranes as the *E. coli* grow. After growing overnight, *E. coli* were centrifuged and washed several times with fresh LB before being given to HeLa cells at a MOI of 50 cfu/cell. *E. coli* uptake into HeLa cells was analysed using spot count masks and an internal mask in order to determine the average number of fluorescent punctae per cell (**Fig. 2**). As expected, *E. coli* expressing OpaI internalized into CEACAM1+ and CEACAM3+ HeLa cells at levels significantly higher than *E. coli* transformed with a blank control plasmid. Compared to control bacteria, there was a slightly-higher internalization of OpaI+ *E. coli* into control cells, although in control cells internalized punctae of both OpaI and Opaless control *E. coli* were significantly lower than bacterial internalization into either CEACAM1+ or CEACAM3+ HeLa cells. There was a slight increase in uptake of OpaI *E. coli* compared to control *E. coli* in CEACAM3+ cells, and a more significant increase in CEACAM1+ cells, suggesting that OpaI most effectively promoted bacterial uptake into HeLa cells when engaging CEACAM1. These results demonstrate that the HeLa cell lines used in this and subsequent experiments with liposomes can engage Opa proteins in binding interactions that are able to lead to internalization.

Important differences exist between bacteria and liposomes which may result in variations in internalization processes between the two systems, and these differences should be considered when comparing Opa proteoliposome binding and uptake to that of OpaI+ *E. coli*. The clearest difference is the size and shape difference between *E. coli*, which are ~2.0 µm long and elongated [2], compared to liposomes, which are spherical and typically less than a few hundred nanometers in diameter [3]. Other important differences between *E. coli* and proteoliposomes include the substantial protein and lipid heterogeneity on the Gram-negative BL21 (DE3) *E. coli* membrane, such as the presence of lipopolysaccharide (LPS) [4], a high molecular weight complex similar in composition to Neisserial lipooligosaccharide (LOS). LOS has been shown to bind Opa proteins on the surface of *Neisseria* [5], and similar interactions between *E. coli* LPS and OpaI may therefore modulate CEACAM interactions which would be absent in proteoliposomes.

3.3—Considerations of negative control liposomes

3.3.1—Potential negative control liposomes

In order to determine what role Opa proteins play in proteoliposome uptake into cells, negative control liposomes lacking functional Opa proteins needed to be generated and analysed for applicability. Proteoliposomes containing recombinant Opa_{50} (OpaA from *Neisseria gonorrhoeae* strain MS11), which is thought to not interact with CEACAM proteins [6], were evaluated as potential negative control liposomes . Additionally, non-proteinaceous liposomes were also evaluated as negative-control liposomes. Surprisingly, liposomes expected to serve as negative controls gave internal fluorescence values comparable to or even higher than values of Opa_{60} proteoliposomes when exposed to CEACAM1+ and control HeLa cells. The high cell fluorescence values of liposomes

containing Opa_{50} were thought to possibly result from non-CEACAM interactions on the cell surface, since Opa_{50}, while not binding CEACAM proteins, does interact with heparan sulfate proteoglycans (HSPGs) [6]. HSPGs are glycoproteins composed of long anionic heparan sulfate chains containing N-acetylglucosamine and glucuronic acid, which attach to a protein core. This protein core may attach to the cell surface as a transmembrane protein (as in syndecans) or with a GPI-anchor (as in glypicans) [6]. HSPG proteins are similar to CEACAM proteins in that they can serve as cell-signal transducers and be involved in cell-cell attachment, and can in fact be present on HeLa cells in the forms of Syndecan-1 and Syndecan-4 [7]. Therefore, the presence of HSPGs such as Syndecan-1 or Syndecan-4 on the tested HeLa cells could result in high-binding and internalization of Opa_{50} proteoliposomes in a manner not dependent on CEACAM, but which precludes the use of Opa_{50} proteoliposomes as suitable negative-control liposomes.

In contrast to Opa_{50} proteoliposomes, whose binding partner could be present on the tested HeLa cells, the high non-specific internalization of Opaless liposomes had a less clear explanation. Both proteoliposomes and non-proteinaceous liposomes were formed with polyethylene glycol (PEG-1000 DMPE), a relatively high molecular weight, water-soluble polymer conjugated to phosphatidylethanolamine (PE) lipids, which was present in the liposomes at 5 mol%. The energy of steric repulsion of PEG polymers on nanoparticles has been found to be comparable to or even exceed the bending energy of the membrane upon endocytosis; therefore, in order to internalize PEGylated particles, ligand/receptor interactions must usually overcome substantial steric repulsion of the PEG [8]. Because liposomes without targeting moieties tend to lack specific interactions with cell surfaces, overcoming this steric repulsion is considerably more difficult, and PEGylated liposomes without targeting ligands are frequently expected to not internalize well in most cellular contexts. For instance, previously-published investigations into uptake of various liposomes

generally report that liposomes containing surface PEGs and/or lacking targeting ligands typically demonstrate lower uptake into cells in culture and *in vivo*, including investigations using J774 macrophages [9], alveolar macrophages[10], KB tumour cells [11], human hepatoma (HepG2) cells [12], J6456-FR lymphoma cells [13], and Her2-overexpressing cancer cells [14]. Liposomes containing water soluble polymers on their surface such as PEG experience steric shielding of their surfaces, which subsequently reduces protein interactions with liposome bilayers, including protein interactions that result in opsonisation by the reticuloendothelial system [15, 16]. Therefore, the high non-specific uptake of non-proteinaceous liposomes into the HeLa cells tested warranted further investigation to understand the cause of this uptake before proceeding, which is the topic of the following section.

3.3.2—HeLa cell uptake of non-proteinaceous liposomes

One force potentially driving non-specific liposome interactions with cells can be the enhanced membrane fusogenicity common with small unilamellar vesicles (SUVs). As the size of small vesicles decreases, the lipid packing in the bilayer is altered in a manner that disorders the acyl chains, increases the depth of water permeation into the lipid bilayer, and decreases the membrane melting temperature (T_m) [17]. The destabilization of ordered lipid packing in vesicles of small sizes tends to increase the free energy of the system, referred to as curvature strain, which can promote membrane interactions of the small vesicle with other lipid bilayers and proteins [17-19]. It is important, therefore, to consider whether non-proteinaceous liposomes could be interacting and internalizing into cells through a non-specific, non-active uptake process such as membrane fusion followed by membrane recycling [20] or whether other internalization process are involved.

In order to investigate non-specific uptake of non-proteinaceous liposomes, fluorescent liposomes of different diameters were created by extrusion through polycarbonate membranes with varying pore sizes (30, 100, 200, and 400 nm). Liposome sizes were confirmed through dynamic light scattering and are reported in **Table 1**. These non-proteinaceous liposomes were then incubated with control, CEACAM1+, and CEACAM3+ HeLa cells and the internal and surface liposomal fluorescence values were determined for each type of HeLa cell (**Fig. 3**). Internal fluorescence values reflect liposomes that were taken into the cells, while surface fluorescence values may reflect liposomes that adhered to the membrane or components on the membrane (such as proteins or carbohydrates), or through membrane fusion between the liposomes and cell surface. The results show a clear inverse correlation between liposome size and internal fluorescence values of liposomes within cells. Internal liposomal fluorescence values for all three HeLa lines were highest after incubation with non-proteinaceous liposomes of 30 nm diameter, while the lowest non-specific internal fluorescence values were seen after incubation with liposomes extruded through 400 nm pores. Liposome incubation with CEACAM3+ HeLa cells generally resulted in lower internal and lower surface fluorescence values than with either control or CEACAM1+ cells, suggesting that perhaps the surface of these cells was less amenable to non-specific liposome interactions, or perhaps that with these CEACAM3+ cells, non-specific surface interactions on average resulted in lower liposome internalization. Also apparent is a significant decrease in both surface and internal fluorescence values between liposomes extruded through 100 nm and 200 nm pore membranes. If non-specific liposome binding and uptake largely results from adhesion and fusion with cell membranes, this sudden and significant drop may be due to a much lower curvature strain in liposomes extruded through larger pores. Other mechanisms exist through which non-proteinaceous liposomes may internalize into cells, however, which would not require liposomes to fuse with cell membranes. One possibility

could be liposomal uptake through macropinocytosis (see 1.5.2), a process normally used by cells for non-specific internalization of extracellular fluid. Macropinocytic uptake is not receptor mediated and involves the actin-driven formation of membrane ruffles on the surface of cells that form pits which later pinch off and internalize into the cells [21].

To investigate how the internalization process of Opaless liposomes compares to Opa proteoliposomes, competition experiments were undertaken between 200 nm fluorescent Opa_{60} proteoliposomes and excessive (5X) concentrations of either non-fluorescent Opa_{60} proteoliposomes or non-fluorescent Opaless proteoliposomes. If cells are pre-treated with non-fluorescent Opa_{60} proteoliposomes and then incubated with both fluorescent Opa_{60} proteoliposomes and non-fluorescent Opa_{60} proteoliposomes, cellular internal fluorescence could be expected to be lower than if cells are simply exposed to fluorescent Opa_{60} proteoliposomes. Such a decrease in fluorescence is reasonable if internalization is mediated by CEACAM proteins, since there exist finite CEACAM proteins on the cell surface, and binding locations on CEACAM occupied by non-fluorescent proteoliposomes instead of fluorescent proteoliposomes should result in decreased internal fluorescence. In contrast, however, if cells are pre-exposed to non-fluorescent, non-proteinaceous liposomes and then exposed to fluorescent Opa_{60} proteoliposomes along with non-fluorescent non-proteinaceous liposomes, it was hypothesized internal fluorescence would be marginally-decreased or unchanged. This assumes Opa_{60} proteoliposomes engage CEACAM while Opaless liposomes do not, since there should exist little competition with Opaless liposomes for internalization if different pathways are used for uptake between proteoliposomes and non-proteinaceous liposomes. This also assumes non-fluorescent Opaless liposomes would not engage and block binding sites on CEACAM proteins, which is reasonable considering there has been no evidence to date that the binding termini of CEACAM proteins engage membranes directly. Surprisingly, pre-incubation of both non-fluorescent Opa_{60} proteoliposomes and non-

fluorescent Opaless liposomes served to fully inhibit cellular internal fluorescence of fluorescently Opa_{60} proteoliposome (**Fig. 4**). This result shows that nearly all of the internal fluorescence of Opa_{60} proteoliposomes in this context results from internalization pathways that can be out-competed using non-proteinaceous liposomes, suggesting that both Opa_{60} proteoliposomes and Opaless liposomes can internalize into CEACAM1+ and control HeLa cells through the same, likely non-CEACAM-mediated pathways.

The finding that Opa_{60} and Opaless liposomes can internalize through the same competable pathway gives insight as to how these liposomes may be internalizing. That the internalization of fluorescent proteoliposomes is competable by using non-proteinaceous liposomes suggests that these liposomes are not internalizing following membrane fusion to HeLa cells, as such a process should not be so strongly competable since the HeLa cell surface is a comparatively large area. The major non-specific internalization pathway most likely to be accessible and shared between Opa_{60} and Opaless liposomes therefore involves liposomal internalization alongside bulk extracellular fluid through non-receptor-mediated macropinocytosis.

3.3.3—Macropinocytic uptake of liposomes

In order to investigate whether macropinosomes are involved in the non-specific internalization of Opaless liposomes, cells were pre-treated with the inhibitor Ethylisopropyl amiloride (EIPA). This amiloride derivative inhibits the Na+/H+ exchanger (NHE) found on the membranes of cells which is believed to be required for actin-driven ruffling of the membrane; inhibition of NHE lowers the submembranous pH and thereby interferes with the actin remodelling and membrane ruffling necessary for macropinocytosis [22, 23]. Inhibition of NHE in CEACAM1+, CEACAM3+, and control HeLa cells was investigated in order to

determine if macropinocytosis was a contributor to non-specific liposome uptake (**Fig. 5**). The results show that the uptake efficiency (defined here as internal fluorescence intensity of liposomes divided by surface fluorescence intensity) of Opaless liposomes was inhibited by treatment with EIPA, suggesting that macropinocytosis plays a role in non-specific liposome uptake. Further, EIPA generally exhibited a greater effect on uptake efficiency with smaller compared to larger liposomes. For instance, EIPA given to cells before exposure to 30 nm Opaless liposomes significantly inhibited liposome uptake into control, CEACAM1+, and CEACAM3+ cells. EIPA-treated cells exposed to 30 nm Opaless liposomes resulted in less than half the internalization efficiency of buffer-control cells. In contrast, EIPA treatment of cells prior to exposure to large 400 nm Opaless liposomes did not effectively inhibit liposome internalization, as Opaless liposome internalization efficiency in treated control, CEACAM1+, and CEACAM3+ cells was not significantly different compared to untreated cells. These results suggest that in all three HeLa cell lines tested, Opaless liposomes internalize at least in-part through macropinocytosis, but that the extent of macropinocytosis regarding non-specific internalization is controlled by liposome size. These conclusions agree well with the physiological role and physical properties of macropinosomes. Involved in non-specific bulk fluid and nutrient uptake, macropinosomes are heterogeneous in size and range from around two hundred nanometers up to several micrometers in diameter [24]. 30 nm and 100 nm liposomes would be expected to be able to access the full range of macropinosome sizes prior to non-specific internalization, while larger liposomes might only be able to access a more limited fraction of total available macropinosomes.

Additionally, differences between not just the fraction of macropinosomes accessible to smaller liposomes, but also the increased number of smaller liposomes able to fit into macropinosomes of a specific size can explain the significantly higher internal cellular fluorescence values seen with the non-specific uptake of small liposomes. Referring again to

the liposome diameters listed in Table 1, the number of lipids per liposome (N_{lipids}) can be determined according to Equation 1, where d is the liposome diameter, h is the bilayer thickness roughly approximated at 5 nm [25], and a is the lipid headgroup area approximated as a PC headgroup of 0.71 nm^2 [25, 26]. Liposomes extruded through a membrane with a 0.03 μm pore size (resulting in a 47.8 nm diameter, d) are composed of approximately $1.64x10^4$ PC lipids per liposome. In contrast, the largest liposomes analysed in this experiment were extruded through 0.4 μm pores (d=298.4 nm) and contain approximately $7.69x10^5$ lipids per liposome, nearly 47 times more lipids. Because DiI is at the same molar concentration in all liposome preps, fluorophore interactions/quenching within the bilayers should be similar regardless of liposome size and therefore show similar fluorescence yields per DiI molecule. In light of the greater number of DiI molecules per large liposome, however, liposomes of 400 nm diameter could be assumed to show ~47 times higher fluorescence intensity per liposome than a 30 nm liposome.

Eqn. 1 $$N_{lipids} = \frac{\left[4\pi\left(\frac{d}{2}\right)^2 + 4\pi[\left(\frac{d}{2}\right)-h]^2\right]}{a}$$

Assuming each liposome is a sphere, the volume of a single 298.4 nm liposome extruded through 400 nm pores is around 247 times the volume of a 47.8 nm liposome extruded through 30 nm pores; therefore, while approximately 47 liposomes extruded through a 30 nm pore are required to equal the fluorescence intensity of a single 400 nm-extruded liposome, the small liposomes reach this equal fluorescence intensity in approximately 20% the volume. The reduced volume requirement for smaller liposomes to equal the fluorescence intensity of larger liposomes may partially explain the significantly higher fluorescence seen with uptake of smaller non-targeted liposomes; in macropinosomes accessible to both 30 nm and 400 nm liposomes, a greater number of small liposomes might be able to fit based on volume

constraints, resulting in significantly higher fluorescence due to the more efficient fluorescence intensity per volume occupied for smaller vesicles.

The high internal fluorescence values for Opaless liposomes and the finding that EIPA at least partially inhibits the internalization of liposomes between 30 and 200 nm suggests that non-specific internalization is likely due in part to macropinocytic uptake rather than membrane fusion. Since macropinocytosis is stimulated by growth factors such as epidermal growth factor (EGF) [27], this could also explain the observed result that cells incubated with liposomes in serum-free media show lower internal fluorescence values than cells incubated with liposomes in media supplemented with growth factor-rich fetal bovine serum (data not included). Further, the sudden and significant decrease in internalization as liposomes increase in extrusion size from 100 nm to 200 nm pores (actual diameters measured as 165 and 197 nm, respectively) seems unlikely to fully result from curvature strain and membrane fusion alone, and suggests that macropinosomes on control, CEACAM1+, and CEACAM3+ HeLa cells are in effect fractionating liposomes around this size range, perhaps due to the sizes of the available macropinosomes.

To confirm the presence of macropinosomes on the HeLa cells tested, the uptake of a fluid-phase marker for macropinosomes was investigated. 70,000 MW fluorescent dextran is internalized almost exclusively through macropinocytosis, and its internalization into cells is usually a sign of non-specific bulk fluid-phase uptake [28]. Control, CEACAM1+, and CEACAM3+ HeLa cells all internalized 70K MW fluorescent-dextran when it was exposed to them in the extracellular media. The highest fluorescent-dextran uptake was found in CEACAM1+ HeLa cells while the lowest dextran-uptake was in CEACAM3+ cells (**Fig. 6**). Cell pre-treatment with EIPA inhibited dextran uptake into control and CEACAM1+ cells but not with CEACAM3+ cells, confirming that for CEACAM1+ cells dextran uptake appears driven by macropinocytosis.

The results of dextran uptake into cells correlate with non-specific liposome uptake with a few exceptions. Following incubation of Opaless liposomes with HeLa cells, the lowest internal fluorescence values were typically seen in CEACAM3+ cells, which correlates well with the low dextran fluorescence seen in CEACAM3+ cells. That CEACAM1+ cells apparently took in significantly more 70K MW dextran correlates somewhat with the uptake of Opaless liposomes between 100-400 nm in size, in which CEACAM1+ cells showed internal liposome fluorescence values equal to or higher than either control or CEACAM3+ cells. One exception to this pattern appears to be the non-specific internal fluorescence values of 30 nm liposomes, which were higher in control cells than CEACAM1+ cells. It is perhaps unsurprising that CEACAM1 expression on HeLa cells seems to correlate with generally-higher non-specific uptake of both liposomes and dextran. A number of commonalities exist between molecular processes related to the activation of certain CEACAM proteins and molecular processes that drive macropinocytosis within cells. Macropinocytosis is typically a transient process driven by growth-factor stimulation and nutrient uptake [27, 29, 30]. Constitutive macropinocytosis can be induced, however, through overexpression of certain signalling receptors on cells. For instance, overexpression of atypical protein kinase C (aPKC) in HeLa cells was found to lead to Src activation, which resulted in growth-factor independent macropinocytosis [29]. In light of the connection between macropinocytosis and cell growth, the promotion of constitutive macropinocytosis with aPKC expression and Src activation was hypothesized to partially explain the link between aPKC overexpression and tumorigenesis [29]. As described in Section 1.3.3, CEACAM1 and CEACAM3 can engage similar signalling pathways, with CEACAM1-L associating with the actin cytoskeleton and promoting interactions with protein kinase C members while CEACAM3, after Opa engagement, induces Src protein tyrosine kinase activation and actin-reorganization [1, 31]. It

is possible that overexpression of certain CEACAM proteins such as CEACAM1 might support macropinocytosis in a manner similar to aPKC overexpression.

Interestingly, members of the cadherin family of homophilic cell-cell adhesion molecules, which share many structural and functional similarities to CEACAM proteins, have been shown to promote macropinocytosis [32]. This is thought to result from E-cadherin and N-cadherin regulating closure of macropinocytic vesicles on the cell surface through cadherin-cadherin adhesion across membrane ruffles. Additionally, N-cadherin was shown to promote dextran uptake into cells [32]. It seems possible that a similar phenomenon could occur within the context of CEACAM1+ HeLa cells, since CEACAM1, similar to E-cadherin and N-cadherin, engages in homophilic adhesion and regulates similar cell processes, such as cell differentiation, proliferation, and migration. It is tempting to speculate therefore that that abnormally high CEACAM1 expression within the context of the CEACAM1+ HeLa cells used here may help drive macropinosome closure within membrane ruffles in a manner similar to cadherin adhesins. As CEACAM3 is not an adhesion CEACAM, but rather is used by neutrophils to lure *Neisseria* into the cells for phagocytosis and killing, CEACAM3 might not be expected to drive macropinosome closure in the manner that E-cadherin and N-cadherin were found to do so. Thus, the self-adhesion properties of CEACAM1 but not CEACAM3 could explain in part the generally higher non-specific liposome uptake and higher dextran internalization into CEACAM1+ cells. It remains unclear, however, why non-specific uptake is higher in control cells than CEACAM3+ cells, even if non-specific uptake into control cells is also generally lower than in CEACAM1+ cells.

3.3.4—The development of Opa(HV-) proteoliposomes as negative control liposomes

As a result of these investigations, it was decided that further experiments into Opa proteoliposome interactions with CEACAM would use proteoliposomes extruded through 400 nm pores for both Opa_{60} proteoliposomes and negative control liposomes. Liposomes extruded at 400 nm were shown to non-specifically internalize into cells at far lower levels than liposomes of smaller diameters. Since these investigations focus on liposomal Opa-CEACAM interactions, and not non-specific uptake of liposomes, it is desirable to keep non-specific liposome uptake as low as possible to avoid confounding results when investigating the relevance of Opa proteins to liposome uptake. From the findings reported here, it is expected that employing liposomes of a larger size will help lower non-specific uptake and more clearly enable differences in uptake to emerge between liposome populations which are due specifically to Opa-CEACAM interactions.

Additionally, it was decided to pursue the use of proteoliposomes rather than non-proteinaceous liposomes as negative control liposomes. Negative control proteoliposomes containing a membrane protein that doesn't bind CEACAM may better match the physical properties of Opa_{60} proteoliposomes than would non-proteinaceous liposomes. For instance, the presence of membrane proteins within liposomes could alter the propensity of liposomes to adhere to or fuse with other bilayers [33]. Thus, ensuring equal molar amounts of protein in both assay and control liposomes more closely keeps the differences between Opa_{60} and control proteoliposomes focused on the desired target of investigation: the activity Opa extracellular loops.

In order to more closely match the physical properties of Opa_{60} proteoliposomes, a membrane protein was therefore sought which would enable non-binding proteoliposomes to be used as a negative control. Opa_{50} had been previously investigated but was found unsuitable due to

high internalization, which may have resulted from cell-surface interactions with HSPGs. A pET-28b plasmid based on the Opa_{60} plasmid was therefore generated in which the majority of Opa_{60} HV1 and HV2 regions, which are required for CEACAM binding, were removed and replaced with a short, seven-residue section composed of glycine and serine residues (GSGSGSG) (**Fig. 7**). Because HV1 and HV2 are required for CEACAM binding, the hypothesis was that removing these sections would abolish CEACAM binding, allowing Opa(HV-) proteoliposomes to serve as negative-control liposomes. A short glycine-serine region was used to replace HV1 and HV2 rather than simply deleting HV1 and HV2 in order to ensure that Opa(HV-) would retain some aspect of extracellular loops, however attenuated. To generate this replacement region, glycine was included in order to prevent formation of unexpected secondary structure, while serine was included in order to ensure this short replacement section was hydrophilic. This rational is similar to why glycine and serine linkers are frequently used in multidomain protein therapeutics, for which unexpected binding interactions involving the linker must be avoided [34]. Opa(HV-) was found to express in BL21 (DE3) *Escherichia coli* cells similarly to Opa_{60} and the purification and folding protocol was the same (described in the Appendix). Due to replacing the large HV regions of Opa_{60} with a shorter glycine-serine linker section, the molecular weight of Opa(HV-) decreased from ~29.4 kDa to ~22.5 kDa, and upon folding into liposomes, Opa(HV-) was found to run on an SDS-PAGE gel as a single band approximately 5kDa smaller than folded Opa_{60} (**Fig. 8**). Formation of Opa(HV-) proteoliposomes by extrusion through 400 nm pores results in liposomes of comparable but slightly smaller size than Opa_{60} proteoliposomes, approximately 243 nm in diameter (23.2% polydispersity) compared to 290 nm (13.7% polydispersity) for Opa_{60}.

3.4—Interactions of Opa_{60} and Opa(HV-) proteoliposomes with HeLa cells

3.4.1—Role of Opa in promoting proteoliposome interactions

In order to investigate Opa proteoliposome interactions with CEACAM+ HeLa cells, cells were exposed for 15 minutes to Opa_{60} and Opa(HV-) proteoliposomes extruded through 400 nm pores. Liposome exposure to cells occurred at 37°C at a phospholipid concentration of 0.2 μM. Following liposome exposure, cells were allowed to incubate further for 0, 1, 2, or 3 hours before being lifted and fixed in 4% PFA. Exposure of CEACAM1+, CEACAM3+, and control HeLa cells results in significantly higher internalization of Opa_{60} proteoliposomes across the timecourse (**Fig. 9**) in all three cell lines compared to Opa(HV-) proteoliposomes (**Fig. 10**). Importantly, because Opa(HV-) proteoliposomes were found to be slightly smaller in diameter than Opa_{60} proteoliposomes (243 nm to 290 nm, indicating an average liposomal volume for Opa(HV-) proteoliposomes approximately 59% of Opa_{60} proteoliposomes), the differences between Opa_{60} and Opa(HV-) internalization may even be slightly conservative since it was shown earlier that smaller liposomes non-specifically internalize at higher levels than larger liposomes. Internalization of Opa_{60} and Opa(HV-) proteoliposomes increased across several hours following initial proteoliposome exposure, with internalization plateauing after 2 hours in control and CEACAM1+ cells, while internalization continued to increase up to 3 hours following proteoliposome exposure in CEACAM3+ cells. Other experiments investigating liposome internalization have reported faster internalization times, such as in NIH3T3 cells that internalize targeted liposomes using macropinocytosis up to an hour after exposure but result in decreased liposome fluorescence by three hours after exposure as fluorophores degrade within lysosomes [35]. It is unknown currently why internalization of Opa proteoliposomes into HeLa cells might proceed more slowly than many other internalization experiments using targeted liposomes, however Opa-mediated

internalization of *Neisseria* bacteria into these same HeLa cell lines was also found to occur across several hours [1].

Calculating the percent increase in proteoliposome internalization that Opa_{60} engenders above Opa(HV-) can give insight into the extent that Opa_{60} promotes proteoliposome internalization. Opa_{60} was most effective at promoting proteoliposome internalization in the context of CEACAM3+ cells, which showed a linear increase in internalization of both types of proteoliposomes up to 3 hours following liposome exposure. Opa_{60} promotes proteoliposome uptake above control Opa(HV-) proteoliposomes to a similar extent in both control and CEACAM1+ cells, as determined by raw internal fluorescence intensity. For all HeLa lines, surface fluorescence intensities of both Opa_{60} and Opa(HV-) proteoliposomes decrease as time increases beyond the initial proteoliposome exposure. This decrease can mirror the increase in internal cellular fluorescence of the liposomes. On the surface of CEACAM1+ HeLa cells, for instance, more Opa_{60} proteoliposomes than Opa(HV-) proteoliposomes are initially bound to the surface when cells are analysed immediately after proteoliposome exposure. By two hours following proteoliposome exposure, however, the surface fluorescence of Opa(HV-) proteoliposomes is higher than Opa_{60} proteoliposomes, supporting the conclusion that Opa_{60} proteoliposomes internalized into CEACAM1+ cells to a greater extent than control liposomes. Similar trends are found in control and CEACAM3+ cells, although the trend is not as clear. Histograms of liposome fluorescence for cell populations show that the increase in mean fluorescence as time increases appears due to decreasing numbers of cells that register no liposome fluorescence, and therefore a general shift toward more cells having at least some fluorescence, rather than significantly increasing the fluorescence maximum seen by the population (**Fig. 11**). This indicates that some cells internalized liposomes much quicker than other cells, but that once internalization occurs, further increases in average internal fluorescence for the general population must come from

slower cells internalizing liposomes rather than cells that quickly internalized liposomes continuing to do so to ever higher levels. This may be due to a depletion in available liposomes on the surfaces of these cells. Using spot masks and the spot counting algorithm developed in the previous chapter, punctae within and on the surfaces of cells can be counted and analysed in order to compare to fluorescence intensities. Spot counts calculate higher internalization of Opa_{60} proteoliposomes than Opa(HV-) control liposomes in all three HeLa lines, mirroring the results obtained from fluorescence intensity measurements. Similarly, counting surface punctae results in a decrease in surface punctae as incubation time increases following proteoliposome exposure as proteoliposomes are taken into cells (**Fig. 12**).

Analysis of internal or surface fluorescence intensities alone may not fully inform about internalization processes. Also important is considering the ratio of internal to total or surface fluorescence, which might be thought of as giving an idea about a cell population's efficiency of internalization [36]. For example, at a specific timepoint, two populations of cells might exist in which both have the same internal fluorescence values. If one population has high surface fluorescence, however, while the second population has low surface fluorescence, then the population with low surface fluorescence would appear to have engaged in more efficient internalization compared to the high-surface fluorescence population, as a greater percent of that population's available fluorescence was internalized. In such a case, only considering the raw internal fluorescence values would miss an important difference between these two populations. In order to look at internalization efficiency of Opa_{60} and Opa(HV-) proteoliposomes, the ratio between internal and surface fluorescence was calculated for CEACAM1+, CEACAM3+, and control HeLa cells. The ratio between internal and surface intensities was used because this method utilizes only fluorescence data which has been correctly identified as internal or surface for the calculation. An alternative method is to calculate internal fluorescence as a percent of total cellular fluorescence, however, this

incorporates fluorescence data into the calculation that could not be confidently ascribed to being internal or surface. This is because there exists some space within each cell in which surface fluorescence cannot be distinguished from internal liposome fluorescence with our masking methods used. Using only fluorescence data from known compartments prevents incorrectly counting fluorescence which is internalized but near the plasma membrane (and therefore indistinguishable from actual surface fluorescence using our masking methods) against a population's internalization efficiency. As a result, fluorescence in this part of the cell (the region between 90% Adaptive Erode of full Brightfield mask and 75% Adaptive Erode of full Brightfield mask) is not used to calculate internalization efficiency.

Interestingly, compared to control proteoliposomes, Opa_{60} promotes a higher internal to surface ratio for CEACAM1+, CEACAM3+, and control HeLa cells, however, the extent of this ratio changes quite differently over time depending on surface CEACAM on the cells (**Fig. 13**). In CEACAM3+ and control HeLa cells, Opa_{60} promotes efficient proteoliposome internalization soon after proteoliposome exposure, with Opa_{60} at one hour after liposome exposure increasing the ratio of internal to surface liposomes between 100-150% above control Opa(HV-) proteoliposomes. As time passes, the ratio of internal to surface liposome fluorescence increases for both Opa_{60} and Opa(HV-) proteoliposomes, however Opa(HV-) proteoliposomes begin to internalize into cells to such a level that they approach Opa_{60} proteoliposomes in terms of the ratio of internal to surface fluorescence. Thus, Opa_{60} and Opa(HV-) proteoliposomes appear to be taken into control and CEACAM3+ cells at similar efficiencies as time increases following liposome exposure. Compared to Opa(HV-), for instance, at 3 hours following proteoliposome exposure, Opa_{60} results in approximately a 20% higher ratio of internal to surface fluorescence in CEACAM3+ and control cells. The implication of this is that as time increases following proteoliposome exposure, Opa(HV-) proteoliposomes catch up to Opa_{60} proteoliposomes in terms of the ratio of internal to surface

fluorescence, as Opa(HV-) drives higher amounts of proteoliposomes into these cells and increases internal fluorescence at the expense of surface fluorescence. In contrast to CEACAM3+ and control cells, looking at the ratio of internal to surface proteoliposome fluorescence within CEACAM1+ cells gives completely different results with regard to Opa_{60} and Opa(HV-). Unlike with CEACAM3+ and control cells, in which the ratio of internal to surface fluorescence of Opa(HV-) proteoliposomes approaches the ratio for Opa_{60} proteoliposomes as time following liposome exposure increases, in CEACAM1+ cells at one hour following exposure, Opa_{60} proteoliposomes begin with only a slightly higher ratio of internal to surface fluorescence than do Opa(HV-) proteoliposomes (33% higher for Opa_{60}) but this difference increases as time post-exposure increases. By three hours following exposure to CEACAM1+ cells, the ratio of internal to surface fluorescence for Opa_{60} proteoliposomes has steadily increased compared to the same ratio for Opa(HV-) and is approximately 71% higher than the ratio for control liposomes. This implies that for CEACAM1+ cells, unlike in CEACAM3+ or control cells, Opa_{60} when compared to control proteoliposomes promotes increasingly higher ratios of internal to surface proteoliposomes.

This result seen in CEACAM1+ cells but not CEACAM3+ or control cells is what would be expected if Opa_{60} acts to promote proteoliposome uptake in an enhanced manner compared to Opa(HV-). As time lengthens following liposome exposure, the higher effectiveness of Opa_{60} at promoting internalization compared to Opa(HV-) should lead to an increasing separation between the ratios of Opa_{60} and Opa(HV-) proteoliposomes that internalize compared to liposomes still remaining on the cell surface. Because Opa_{60} promotes enhanced liposome internalization into CEACAM1+ cells compared to Opa(HV-), increasing the time available for liposomes to internalize only serves to further allow more Opa_{60} proteoliposomes to internalize into cells compared to Opa(HV-) proteoliposomes. In CEACAM3+ and control cells, extending the time available for proteoliposomes to internalize results in Opa(HV-)

liposomes catching up to Opa_{60}, suggesting that whatever the cause is of Opa_{60} proteoliposomes initially internalizing into these cells at higher levels than Opa(HV-) proteoliposomes, this process is unsustainable. Across all three hours the ratio of internal to surface fluorescence steadily increases for both Opa_{60} and Opa(HV-) as liposomes internalize and are depleted from the cell surface. As time following liposome exposure to CEACAM3+ or control cells lengthens, however, the ratio of internal to surface fluorescence increases faster with Opa(HV-) proteoliposomes than Opa_{60} proteoliposomes, which indicates a process by which Opa_{60} does not promote more efficient internalization than Opa(HV-) into CEACAM3+ and control cells, unlike the situation in CEACAM1+ cells.

3.4.2—Importance of CEACAM expression for Opa proteoliposome interactions

In the previous section, the binding and uptake of Opa proteoliposomes into CEACAM1+, CEACAM3+, and control cells was discussed with a specific focus on the role Opa proteins play in promoting proteoliposome internalization. In order to further analyse what role different CEACAM proteins play in promoting internalization, the binding and internalization of Opa_{60} proteoliposomes can be compared at different timepoints with respect to CEACAM1+, CEACAM3+, or control HeLa cells.

Total cell fluorescence immediately after proteoliposome exposure shows the total amount of proteoliposomes engaging each cell type, since total fluorescence accounts for both internal and surface proteoliposomes. Immediately after proteoliposome exposure, CEACAM1+ HeLa cells bound higher amounts of both Opa_{60} and Opa(HV-) proteoliposomes than either control or CEACAM3+ cells, with Opa_{60} proteoliposome fluorescence approximately 1.4 times higher than Opa(HV-) fluorescence (**Fig. 14**). This result is consistent with Opa_{60} promoting proteoliposome binding to cellular CEACAM1. Proteoliposome binding was

lowest to CEACAM3+ cells, although for these cells total Opa_{60} fluorescence was approximately 5.0 times higher than Opa(HV-) fluorescence. This result is consistent with the lower overall proteoliposome fluorescence intensities reported earlier for CEACAM3+ cells, as well as the large difference between Opa_{60} proteoliposome fluorescence values and those for control proteoliposomes. It is unknown why CEACAM3+ cells bind proteoliposomes at much lower levels than do CEACAM1+ or control cells, although it is difficult to compare straight fluorescence values between CEACAM3+ and CEACAM1+ cells as potential differences in CEACAM expression within these two cell lines prevent direct comparisons of proteoliposome internal fluorescence. One method to attempt a valid comparison that can account for differences in CEACAM expression is by analysing the ratio of internal to surface fluorescence as was shown in **Figure 13** and described previously, which showed that Opa_{60} increases the ratio of internal to surface proteoliposome fluorescence beyond Opa(HV-) in the context of CEACAM1+ cells but not CEACAM3+ cells.

Within a population of CEACAM+ cells, subpopulations of cells displaying low, medium, or high CEACAM density on their surface can be determined from α-CEACAM antibody staining. These sub-populations can then be analysed [37] to correlate proteoliposome uptake with CEACAM-expression. For example, within the population of CEACAM1+ HeLa cells, subpopulations defined by cells of the lowest 25% αCEACAM antibody staining, middle 50% staining, and highest 25% antibody staining were defined and Opa_{60} proteoliposome internalization for each subpopulation was determined (**Fig. 15**). Proteoliposome uptake was positively correlated with CEACAM1 expression as determined by pan-CEACAM antibody staining, indicating that cells expressing higher levels of CEACAM1 internalize on average higher numbers of Opa_{60} proteoliposomes. This result is again consistent with earlier results suggesting that Opa_{60} promotes binding and internalization into CEACAM1+ cells.

3.4.3—The role of metabolic energy in proteoliposome internalization by HeLa cells

The importance of cellular metabolic energy to the internalization of Opa_{60} was investigated within the context of CEACAM1+, CEACAM3+, and control HeLa cells. Cells were pre-treated by inhibitors of glycolysis (2-deoxyglucose) and oxidative phosphorylation (sodium azide) in order to deplete the cells of ATP [38, 39]. Binding of proteoliposomes to the cell surface is not expected to be inhibited following energy-depletion as liposome binding to surface markers such as CEACAM does not depend on cellular ATP. Depletion of metabolic energy results in decreased active-uptake of proteoliposomes in CEACAM1+, CEACAM3+, and control HeLa cells (**Fig. 16**). Treatment of HeLa cells with metabolic inhibitors exerts greater effects, however, on proteoliposome uptake in the context of CEACAM1+ and CEACAM3+ cells than in control cells. Treating CEACAM1+ cells decreased internal proteoliposome fluorescence by 91% while treating CEACAM3+ cells decreased fluorescence by 99%. This suggests that nearly all proteoliposome internalization into CEACAM1+ and CEACAM3+ HeLa cells is through active-uptake processes. In contrast, treatment of control cells with inhibitors of ATP synthesis decreased Opa_{60} proteoliposome uptake by only 51%, suggesting that internalization of proteoliposomes by control cells does utilize metabolic energy, but that there may exist non-active uptake pathways within control cells that also contribute to proteoliposome internalization. It is currently unknown why control cells might partially internalize liposome fluorescence in a manner not requiring metabolic energy while CEACAM1+ and CECAM3+ cells do not do so, although the lack of metabolic energy suggests some type of fusion process may be occurring. Possibly, the large amounts of CEACAM1 and CEACAM3 overexpression on CEACAM1+ and CEACAM3+ HeLa cells might be directly or indirectly inhibiting direct membrane-membrane interactions with liposomes, while control cells, lacking CEACAM overexpression, can engage in higher amounts of non-specific, non-energy dependent interactions.

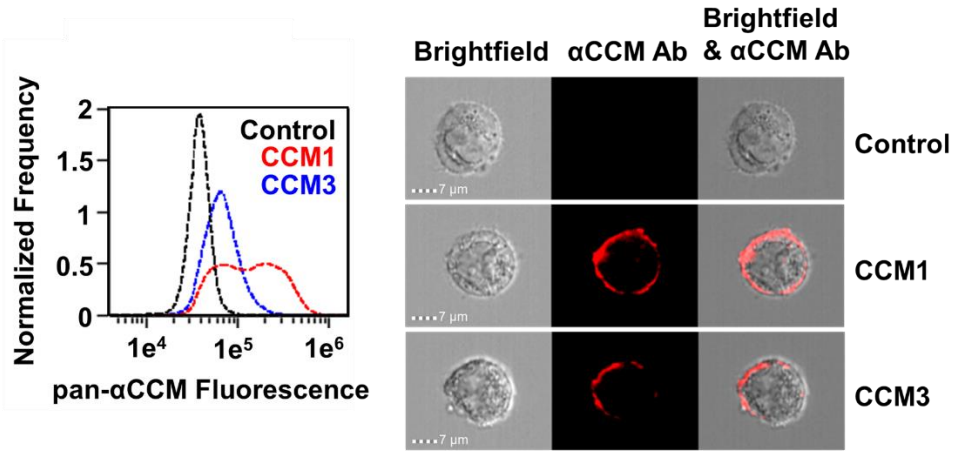

Figure 1. Pan-CEACAM (CCM) antibody staining in control, CEACAM1+, and CEACAM3+ HeLa cells. Using a pan-CEACAM antibody results in a higher antibody fluorescence in CEACAM1+ cells compared to CEACAM3+ cells, although this difference may partially reflect different antibody binding affinities for CEACAM1 and CEACAM3 and so may not fully indicate different protein expression levels. In contrast, anti-CEACAM fluorescence was low on control HeLa cells. In images, antibody staining is shown as red fluorescence compared to the cell Brightfield image.

A. **B.**

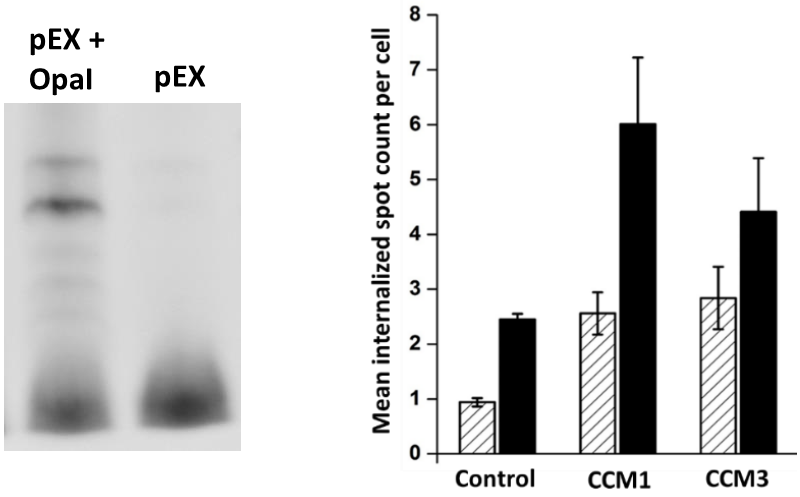

Figure 2. OpaI promotes E. coli internalization into CEACAM1 and CEACAM3 HeLa cells. (A) *E. coli* transformed with pEX plasmid with OpaI insert express Opa as shown by Western blot staining. A 1:1000 αOpa primary antibody and 1:5000 Alexa-555 goat anti-mouse secondary antibody show bands around 29 kDa in *E. coli* transformed with OpaI+ pEX plasmid. (B) E. coli expressing OpaI (black) were found to internalize into cells at higher levels than plasmid control E. coli (grey stripes) as determined by a spot-count algorithm. *E. coli* internalization into CEACAM1 and CEACAM3 cells was higher than into control HeLa cells, suggesting that OpaI promotes *E. coli* internalization through both these CEACAMs. Approximately 2000 cells were analysed for each condition. Error bars represent 99% C.I.

Membrane pore size	Liposome diameter (nm)	Polydispersity (%)
0.4 µm	298.4 (no protein)	27.7 (no protein)
	290.0 (Opa_{60})	13.7 (Opa_{60})
	243.7 (Opa(HV-))	23.2 (Opa(HV-))
0.2 µm	197.2	27.5
0.1 µm	165.4	16.3
0.03 µm	47.8	--

Table 1. **Liposome diameter and polydispersity following extrusion through polycarbonate membranes of various pore sizes.** Diameter reflects particle size while polydispersity reflects size variance. Data is included for Opaless liposomes, as well as Opa_{60} and Opa(HV-) proteoliposomes.

A.

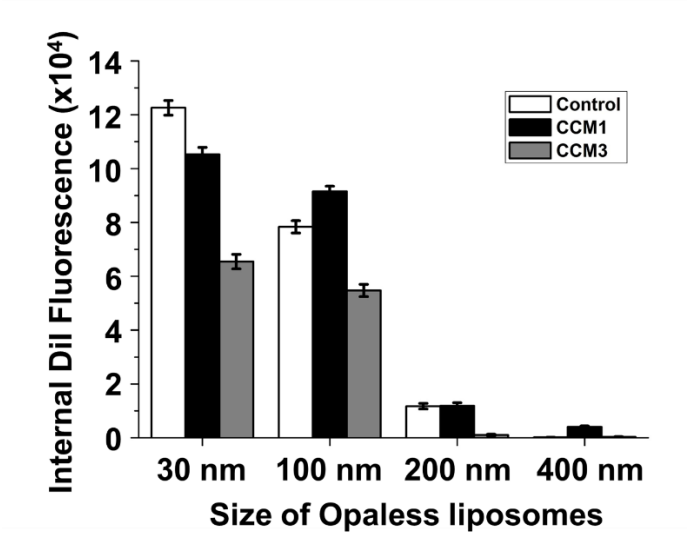

B.

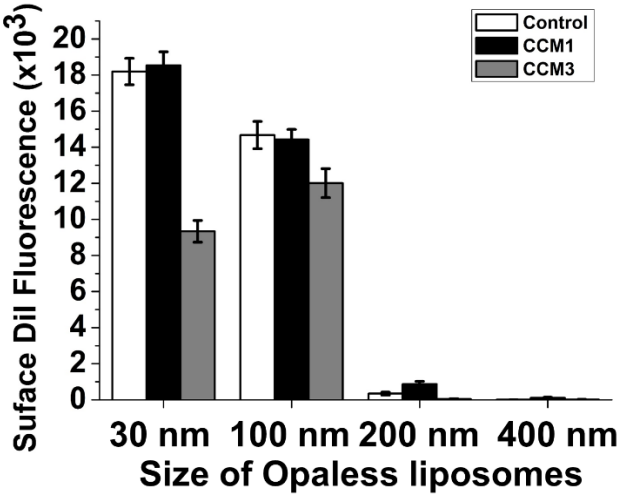

Figure 3. Non-specific uptake of liposomes decreases as liposome size increases. (A) Opaless liposomes show an inverse correlation between increasing size (using approximately 30, 100, 200, and 400 nm particles) and non-specific uptake into control (white), CEACAM1+ (black), and CEACAM3+ (grey stripes) HeLa cells. (B) A similar trend was seen when looking at surface instead of internal liposome fluorescence for the same liposomes with control, CEACAM1+ and CEACAM3+ cells. Approximately 2000 cells were analysed per condition. Error bars represent 95% C.I.

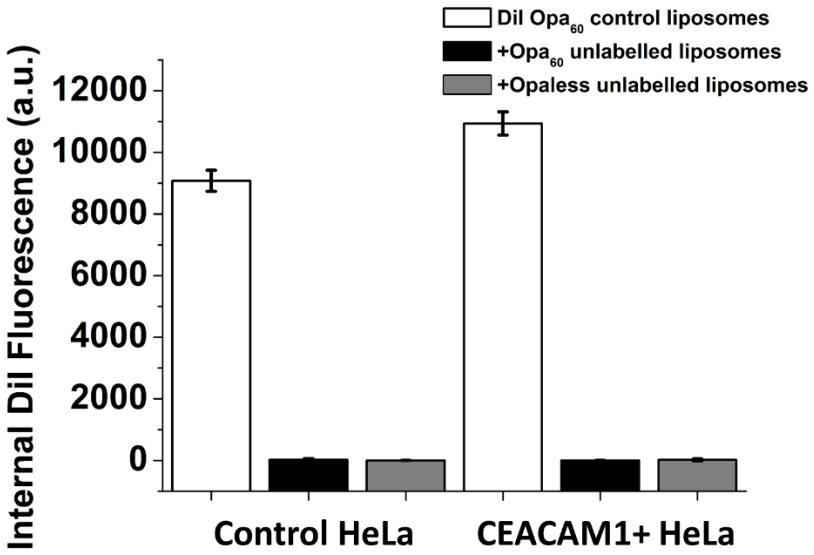

Figure 4. Opaless liposomes compete with Opa$_{60}$ proteoliposomes for internalization into control and CEACAM1+ HeLa cells. Internal fluorescence of Opa$_{60}$ proteoliposomes is decreased when control or CEACAM1+ cells are pre-incubated with either non-fluorescent Opa$_{60}$ proteoliposomes (black) or non-fluorescent Opaless liposomes (grey). Pre-incubation of cells with buffer does not inhibit uptake of fluorescent Opa proteoliposomes (white). These results imply that Opaless liposomes interact with control and CEACAM1+ HeLa cells in a manner that competes with proteoliposome internalization, suggesting that internalization of control and proteoliposomes can internalize through the same pathways. Approximately 2000 cells were imaged for each condition. Error bars represent 95% C.I.

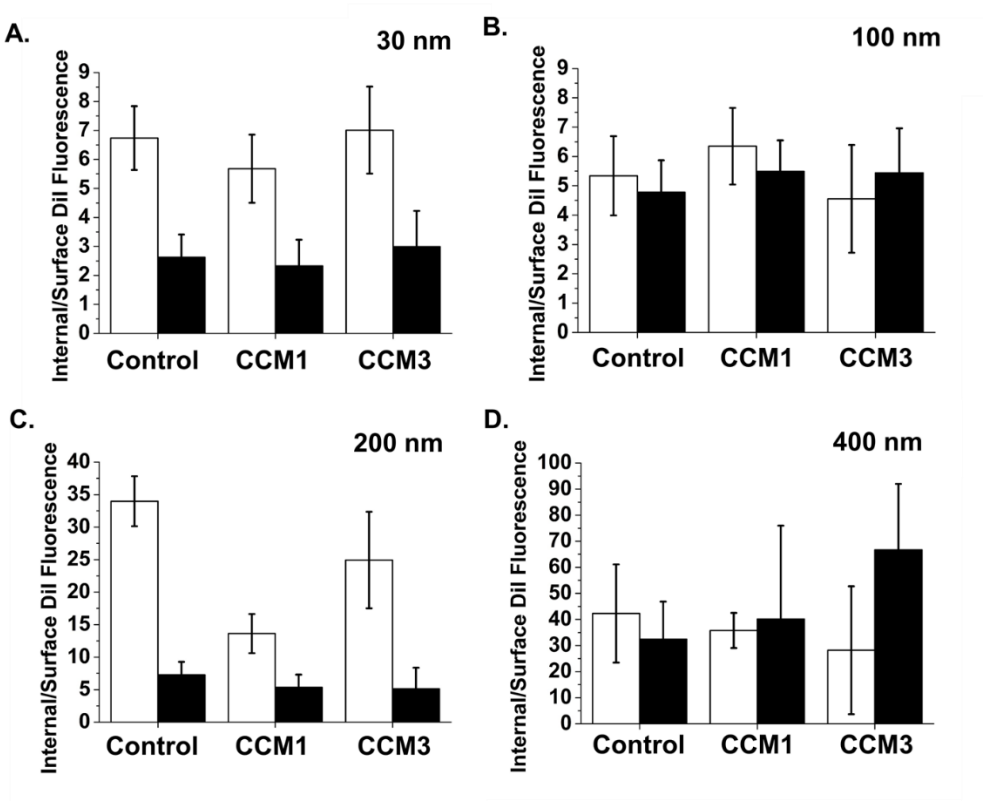

Figure 5. The inhibitor of macropinocytosis EIPA decreases non-specific uptake of liposomes into HeLa cells in a manner inversely correlated to liposome size. Liposomes extruded through membranes with pore sizes of 30 nm (A), 100 nm (B), 200 nm (C), and 400 nm (D) were exposed to control, CEACAM1, and CEACAM3 HeLa cells pre-treated with EIPA (black) or control DMSO (white). The uptake efficiency (internal/surface fluorescence) of 400 nm liposomes was largely unaffected by EIPA, while the uptake efficiency of 30 nm liposomes was decreased upon EIPA exposure, suggesting macropinosomes play a greater role in the non-specific uptake of these smaller liposomes. Approximately 2000 cells were analysed for each condition. Error bars represent 95% C.I.

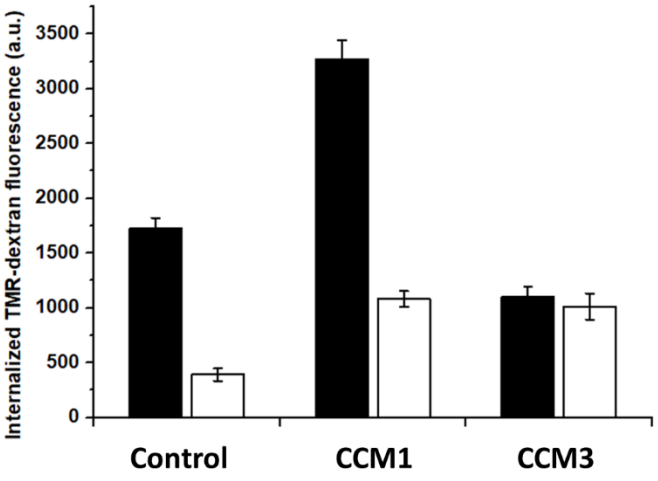

Figure 6. CEACAM1+ HeLa cells internalize higher levels of 70 kDa TMR-dextran than control or CEACAM3+ HeLa cells. HeLa cells internalize 70 kDa dextran, a fluid-phase marker for micropinocytosis, with CEACAM1+ cells showing the highest internalization of dextran, suggesting that CEACAM1+ cells may internalize particles non-specifically at higher levels than control or CEACAM3+ cells. Compared to a buffer control (black), EIPA inhibition (white) of dextran uptake into CEACAM1+ cells confirms that dextran uptake is driven by membrane ruffling and macropinocytosis. Approximately 2000 cells were analysed for each condition. Error bars represent 99% C.I.

A.

Opa(HV-) sequence:

CATATGGCAAGTGAAGACGGCGGCCGCGGCCCGTATGTGCAGGCGGATTTAGCC
TACGCCTACGAACACATTACCCACGATTATCCGGAACCAACCGCTCCAAACAAG
AACAAAATAAGCACGGTAAGCGATTATTTCAGAAACATCCGCACCCGCTCCGTC
CACCCCCGGGTGTCGGTCGGCTACGACTTCGGCGGCTGGAGGATAGCGGCAGAT
TATGCCCGTTACAGAAAATGGGGATCAGGATCAGGATCAGGAACGGAAAATCAG
GAAAACGGTACGTTCCACGCCGTCTCCTCACTCGGCTTATCCGCTATTTACGATTT
CCAAATAAACGATAAATTCAAACCCTATATCGGCGCGCGCGTCGCCTACGGACA
CGTCGGATCAGGATCAGGATCAGGACGCGTGGGTCTCGGTGTCATCGCCGGCGT
CGGTTTCGACATCACGCCCAAGCTGACCCTGGACGCCGGGTATCGCTACCACAAC
TGGGGACGCTTGGAAAACACCCGCTTCAAAACCCACGAAGCCTCATTGGGCGTG
CGCTACCGCTTCTAAGGATCC

Length (bp): 564

Vector: pET-28b

5' site: NdeI

3' site: BamHI

B.

```
Opa60     1    ASEDGGRGPYVQADLAYAYEHITHDYPEPTAPNKNKISTVSDYFRNIRTRSVHPRVSVGY  60
Opa(HV-)  1    ASEDGGRGPYVQADLAYAYEHITHDYPEPTAPNKNKISTVSDYFRNIRTRSVHPRVSVGY  60

Opa60     61   DFGGWRIAADYARYRKWNNNKYSVNIENVRIRKENGIRIDRKTENQENGTFHAVSSLGLS  120
Opa(HV-)  61   DFGGWRIAADYARYRKWGSGSGS------------------GTENQENGTFHAVSSLGLS  102

Opa60     121  AIYDFQINDKFKPYIGARVAYGHVRHSIDSTKKTIEVTTVPSNAPNGAVTTYNTDPKTQN  180
Opa(HV-)  103  AIYDFQINDKFKPYIGARVAYGHVGSGSGSGRVGLG-----------------------  138

Opa60     181  DYQSNSIRRVGLGVIAGVGFDITPKLTLDAGYRYHNWGRLENTRFKTHEASLGVRYRF  238
Opa(HV-)  139  -------------VIAGVGFDITPKLTLDAGYRYHNWGRLENTRFKTHEASLGVRYRF  183
```

Figure 7. Opa(HV-) genetic sequence and amino acid sequence alignment. (A) Opa(HV-) sequence was inserted into a pET-28b vector MCR using NdeI and BamH1 restriction sites. (B) Opa_{60} and Opa(HV-) sequence alignment show that the HV1 and HV2 regions of Opa_{60} were replaced with a short glycine-serine sequence for Opa(HV-).

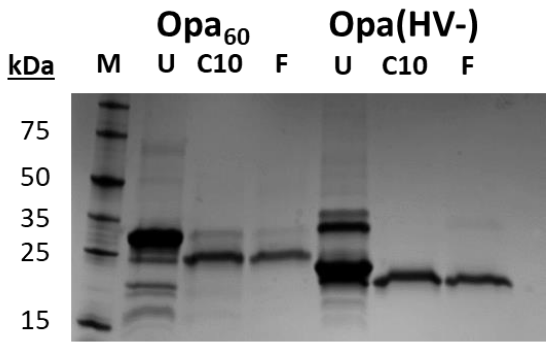

Figure 8. Opa$_{60}$ and Opa(HV-) folding gel. SDS-PAGE gel of Opa$_{60}$ and Opa(HV-) refolded into fluorescent DMPC liposomes after folding for 4 days at 37°C. Shown are unfolded Opa (U), Opa folded into C10-PC lipids (C10) and Opa folded into final liposomes (F) for both Opa$_{60}$ and Opa(HV-) proteins, as well as the molecular weight marker (M). Folded Opa$_{60}$ runs at a higher molecular weight than folded Opa(HV-) due to the truncation of Loops 2 and 3 of Opa$_{60}$ when replacing Opa$_{60}$ HV1 and HV2 with short glycine-serine regions for Opa(HV-).

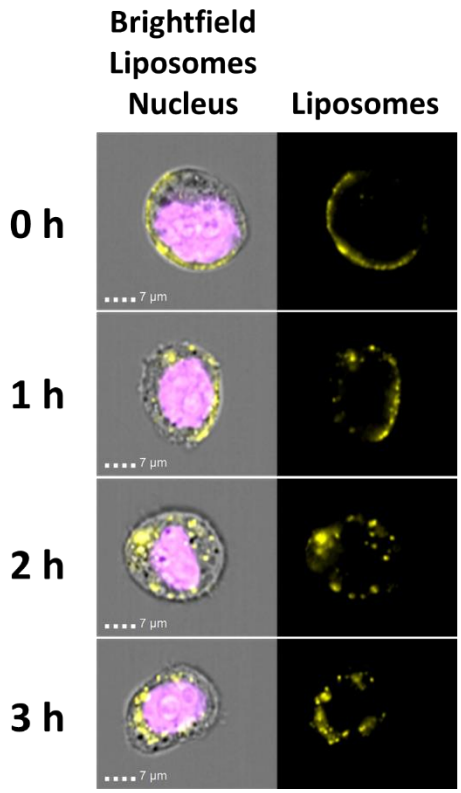

Figure 9. Opa proteoliposomes internalize into HeLa cells several hours after exposure. Representative Brightfield images of CEACAM1+ HeLa cells stained with DAPI (blue) and exposed to Opa_{60} proteoliposomes (yellow) show that proteoliposomes adhere to cell surface immediately after cell exposure (0 h), but across several hours can internalize into cells. Internalization of liposomes appears as fluorescence punctae within the borders of the cell as shown in the merged Brightfield image.

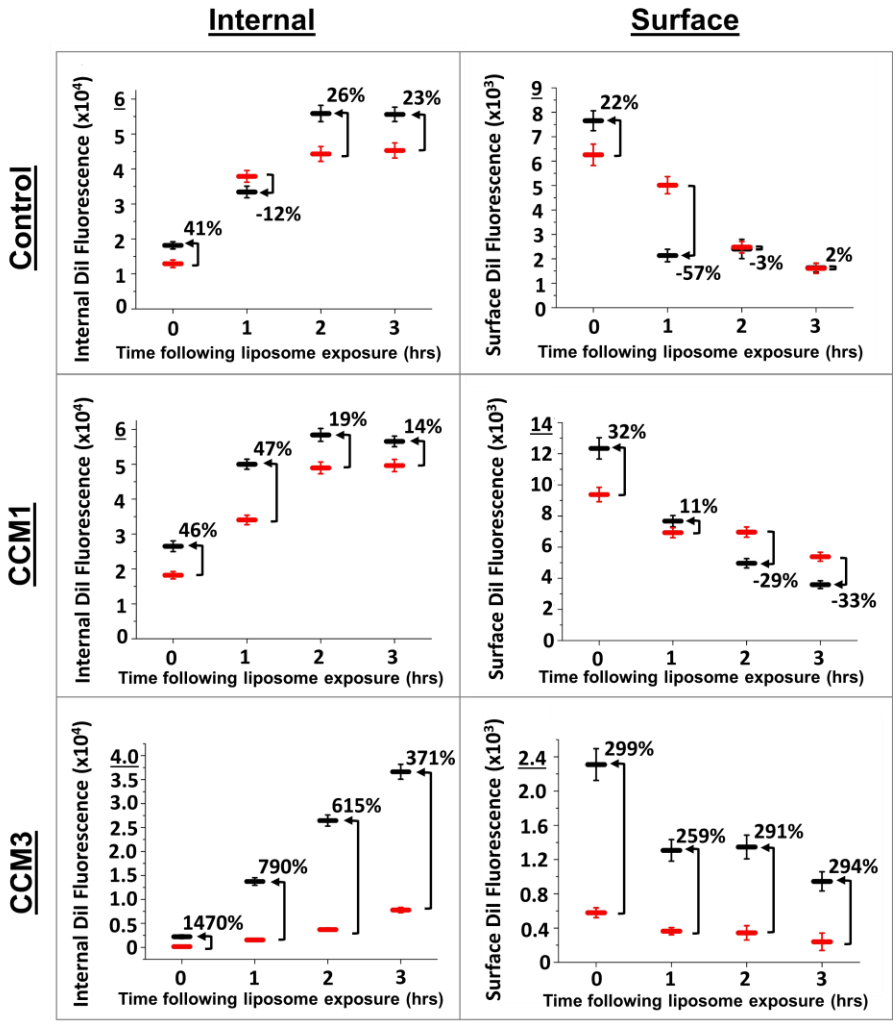

Figure 10. Opa$_{60}$ promotes proteoliposome uptake into HeLa cells compared to Opa(HV-) control liposomes. HeLa cells were pulsed briefly with proteoliposomes before incubating further (0, 1, 2, or 3 hrs) in liposome free media. Internal and surface liposome fluorescence was determined for control, CEACAM1+, and CEACAM3+ HeLa cells following exposure to Opa$_{60}$ (black) and Opa(HV-) (red) proteoliposomes. Liposomes internalize into control and CEACAM1+ cells up to 2 hours following exposure, while internalization into CEACAM3+ cells continues throughout the timecourse. A decrease in surface liposome fluorescence is seen over the course of the assay. The increase or decrease in Opa$_{60}$ proteoliposome fluorescence is given as a percent change of Opa(HV-) fluorescence. Approximately 2500 cells are analysed for each condition. Error bars represent 95% C.I.

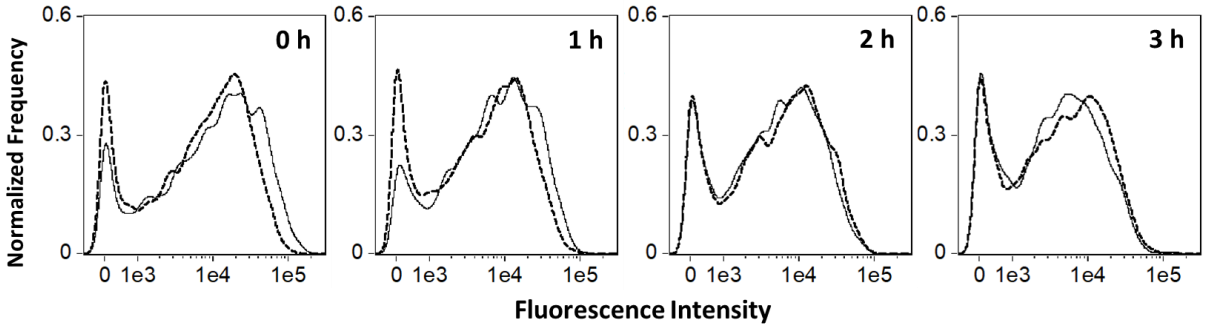

Figure 11. Opa_{60} (solid) and Opa(HV-) (bold dash) incubated with CEACAM1+ HeLa cells for 0, 1, 2, 3 hrs. Histograms of normalized frequency per internalized fluorescence intensity for Opa_{60} and Opa(HV-) proteoliposomes during timecourse of uptake. Between 0 and 1 hours following exposure, Opa(HV-) proteoliposomes show a higher population of cells with no fluorescence intensity compared to Opa_{60} proteoliposomes. By 2 hrs, the normalized populations of cells with no fluorescence intensity have reached a similar level between Opa(HV-) and Opa_{60} proteoliposomes, suggesting that some cells which had not internalized Opa(HV-) liposomes at 1 hr have now reached equivalent internalized fluorescence levels compared to cells exposed to Opa_{60} proteoliposomes. Thus, uptake of Opa(HV-) liposomes appears to be slower than Opa_{60} proteoliposome uptake, but given enough time, these proteoliposomes can non-specifically internalize.

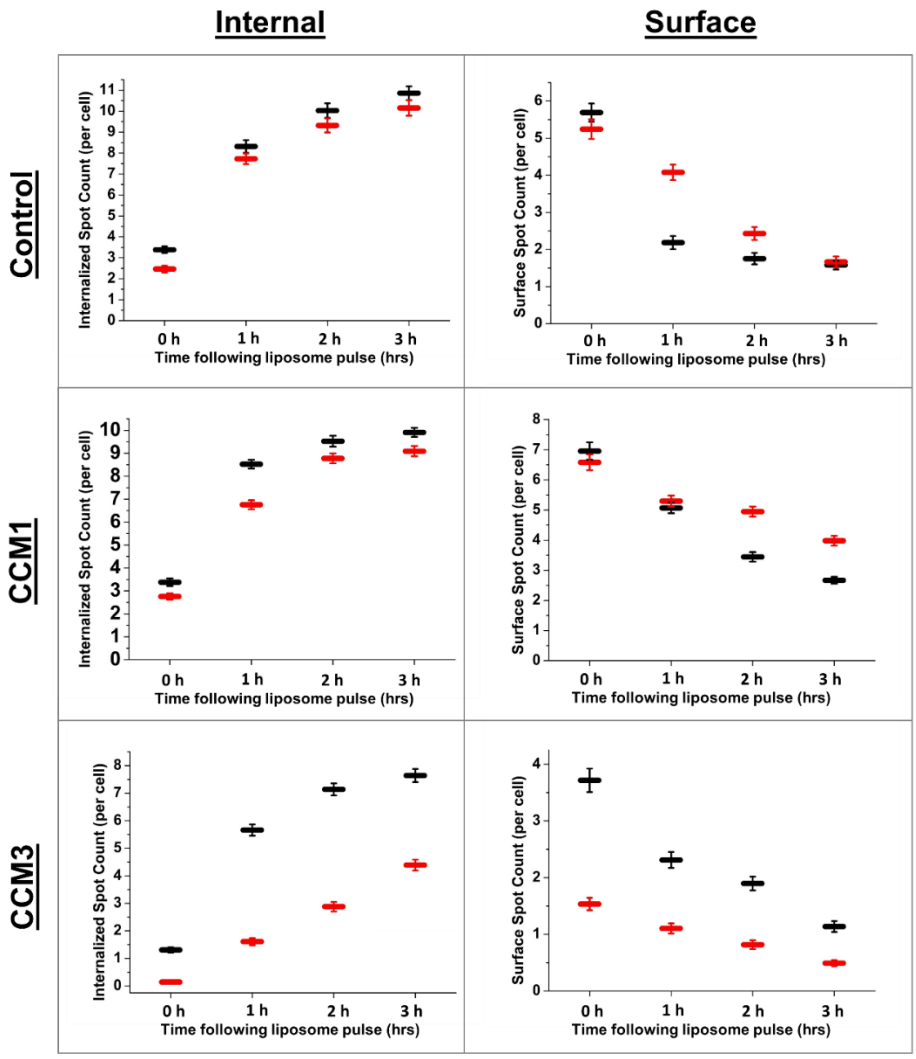

Figure 12. Spot counts indicate increasing numbers of proteoliposomes internalize and decreasing numbers are adhered to the cell surface as time following exposure increases. Similar to fluorescence intensity results, Opa_{60} proteoliposomes (black) internalize at higher levels than do Opa(HV-) proteoliposomes (red) after exposure to CEACAM1+, CEACAM3+, and control HeLa cells. As time increases beyond proteoliposome exposure, the number of proteoliposomes internalizing increases up to 2 hours in control and CEACAM1+ cells before levelling off, while in CEACAM3+ cells both Opa_{60} and Opa(HV-) proteoliposomes increase through the duration of the timecourse. Numbers of surface liposomes decrease across the timecourse for all cell types as they internalize into cells. Approximately 2500 cells are analysed for each condition. Error bars represent 95% C.I.

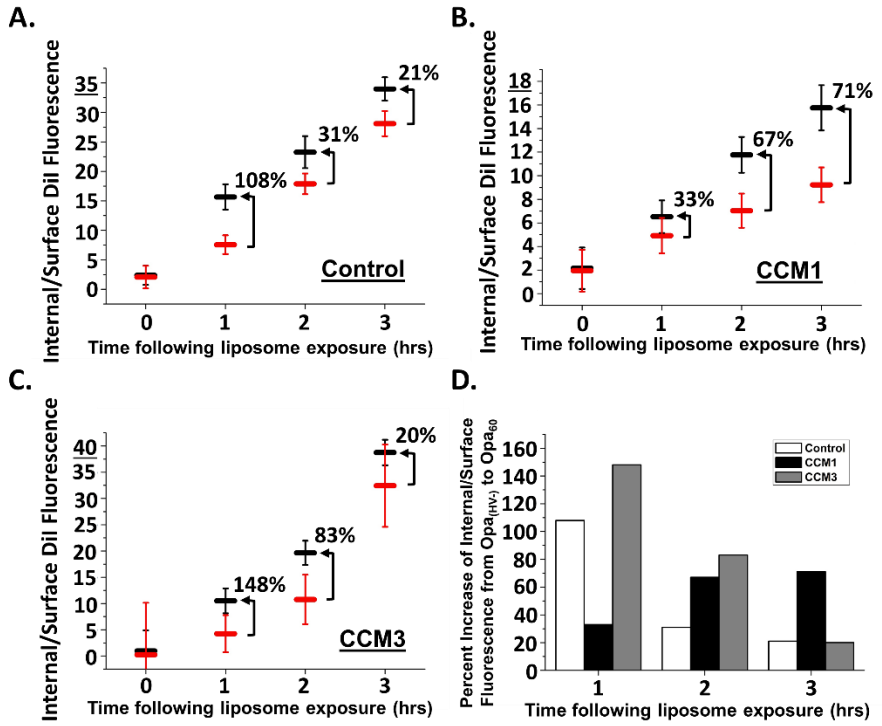

Figure 13. Opa$_{60}$ promotes proteoliposome uptake into HeLa cells. HeLa cells were pulsed briefly with proteoliposomes before incubating further (0, 1, 2, or 3 hrs). Liposome internalization efficiency (internal/surface fluorescence) was determined for control (A), CEACAM1+ (B), and CEACAM3+ (C) HeLa cells following exposure to Opa$_{60}$ (black) and Opa(HV-) (red) proteoliposomes. Opa$_{60}$ was found to promote proteoliposome uptake into HeLa cells compared to Opa(HV-), shown as higher Internal/Surface values. The increase or decrease in proteoliposome internalization efficiency from Opa(HV-) to Opa$_{60}$ is shown as a percent of baseline Opa(HV-) proteoliposome efficiency on each graph. These values were plotted in (D), showing that as time increases, efficiency of Opa$_{60}$ internalization when compared to Opa(HV-) internalization increases only within the context of CEACAM1+ HeLa cells. Approximately 2500 cells are analysed for each condition. Error bars in A-C represent 95% C.I.

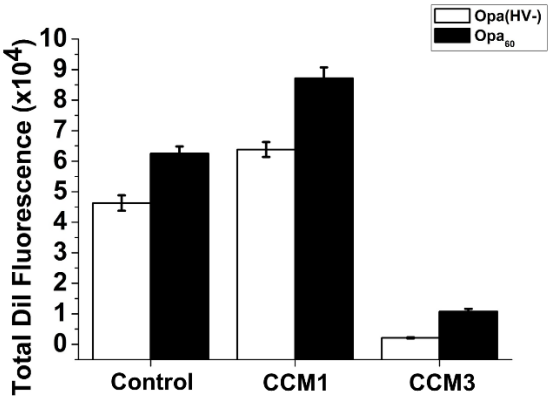

Figure 14. Total liposome fluorescence on HeLa cells reflects initial proteoliposome binding. The total cellular fluorescence for control, CEACAM1+, and CEACAM3+ HeLa cells was calculated immediately after a short, 15 minute proteoliposome exposure. Total fluorescence values were highest in CEACAM1+ cells and lowest in CEACAM3+ cells, reflecting higher proteoliposome binding in CEACAM1+ cells. For all three cell lines, Opa_{60} (black) promoted a higher initial binding of proteoliposomes compared to Opa(HV-) proteoliposomes (white). Approximately 2500 cells are analysed for each condition. Error bars represent 95% C.I.

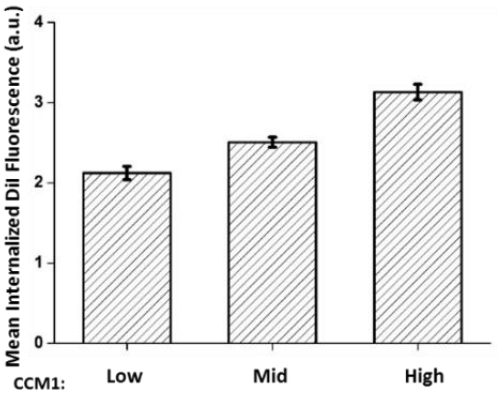

Figure 15. Correlation of Opa_{60} proteoliposome uptake with CEACAM1 expression levels. CEACAM1+ HeLa cells were separated into lowest 25%, middle 50%, and highest 25% CEACAM expressers through pan-αCEACAM rb antibody (1:100) staining followed by Alexa647 goat anti-rabbit secondary antibody (1:1000) staining. A positive correlation between CEACAM1 expression levels and internalized DiI fluorescence is observed, consistent with the hypothesis that CEACAM1 expression on cells may promote Opa_{60} proteoliposome uptake. Error bars represent 99% C.I.

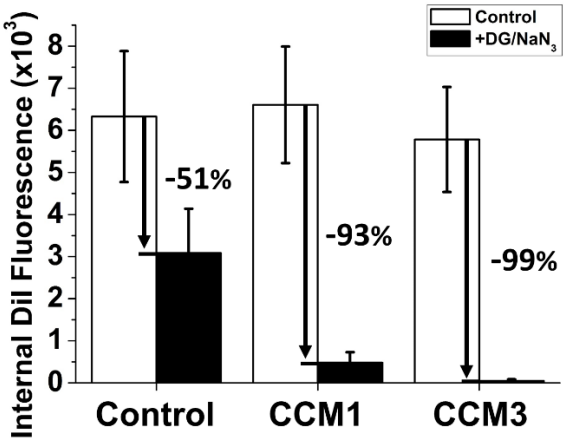

Figure 16. Cellular metabolic energy promotes internalization of Opa_{60} proteoliposomes into HeLa cells. Pre-treatment of control, CEACAM1+, or CEACAM3+ HeLa cells with metabolic inhibitors (black) depletes the available pool of ATP and decreases subsequent Opa_{60} proteoliposome uptake compared to untreated cells (white). The effect of ATP depletion was more pronounced in HeLa cells expressing CEACAM1 or CEACAM3, suggesting internalization into control cells may be due in part to non-active uptake processes. Approximately 2000 cells are analysed for each condition. Error bars represent 95% C.I.

3.5—References

1. McCaw, S.E., E.H. Liao, and S.D. Gray-Owen, *Engulfment of Neisseria gonorrhoeae: Revealing Distinct Processes of Bacterial Entry by Individual Carcinoembryonic Antigen-Related Cellular Adhesion Molecule Family Receptors.* Infection and Immunity, 2004. **72**(5): p. 2742-2752.
2. Reshes, G., et al., *Cell Shape Dynamics in Escherichia coli.* Biophysical Journal, 2008. **94**(1): p. 251-264.
3. Akbarzadeh, A., et al., *Liposome: classification, preparation, and applications.* Nanoscale Research Letters, 2013. **8**(1): p. 102-102.
4. Mamat, U., et al., *Detoxifying Escherichia coli for endotoxin-free production of recombinant proteins.* Microbial Cell Factories, 2015. **14**(1): p. 57.
5. Blake, M.S., et al., *Gonococcal opacity: lectin-like interactions between Opa proteins and lipooligosaccharide.* Infection and Immunity, 1995. **63**(4): p. 1434-1439.
6. Martin, J.N., et al., *Neisserial Opa Protein–CEACAM Interactions: Competition for Receptors as a Means of Bacterial Invasion and Pathogenesis.* Biochemistry, 2016. **55**(31): p. 4286-4294.
7. Brule, S., et al., *The shedding of syndecan-4 and syndecan-1 from HeLa cells and human primary macrophages is accelerated by SDF-1/CXCL12 and mediated by the matrix metalloproteinase-9.* Glycobiology, 2006. **16**(6): p. 488-501.
8. Li, Y., M. Kröger, and W.K. Liu, *Endocytosis of PEGylated nanoparticles accompanied by structural and free energy changes of the grafted polyethylene glycol.* Biomaterials, 2014. **35**(30): p. 8467-8478.
9. Vertut-Doï, A., H. Ishiwata, and K. Miyajima, *Binding and uptake of liposomes containing a poly(ethylene glycol) derivative of cholesterol (stealth liposomes) by the macrophage cell line J774: influence of PEG content and its molecular weight.* Biochimica et Biophysica Acta (BBA) - Biomembranes, 1996. **1278**(1): p. 19-28.
10. Perry, D.G. and W.J. Martin, *Fluorescent liposomes as quantitative markers of phagocytosis by alveolar macrophages.* Journal of Immunological Methods, 1995. **181**(2): p. 269-285.
11. Cheng, Z., et al., *Simultaneous Quantification of Tumor Uptake for Targeted and Nontargeted Liposomes and Their Encapsulated Contents by ICPMS.* Analytical chemistry, 2012. **84**(17): p. 7578-7582.

12. Mei, L., et al., *Increased tumor targeted delivery using a multistage liposome system functionalized with RGD, TAT and cleavable PEG.* International journal of pharmaceutics, 2014. **468**(1-2): p. 26-38.
13. Shmeeda, H., et al., *Intracellular uptake and intracavitary targeting of folate-conjugated liposomes in a mouse lymphoma model with up-regulated folate receptors.* Molecular cancer therapeutics, 2006. **5**(4): p. 818-824.
14. Kirpotin, D., et al., *Sterically stabilized anti-HER2 immunoliposomes: design and targeting to human breast cancer cells in vitro.* Biochemistry, 1997. **36**(1): p. 66-75.
15. Gullotti, E., J. Park, and Y. Yeo, *Polydopamine-based surface modification for the development of peritumorally activatable nanoparticles.* Pharmaceutical research, 2013. **30**(8): p. 1956-1967.
16. Klibanov, A.L., et al., *Amphipathic polyethyleneglycols effectively prolong the circulation time of liposomes.* FEBS letters, 1990. **268**(1): p. 235-237.
17. Wetterau, J.R. and A. Jonas, *Effect of dipalmitoylphosphatidylcholine vesicle curvature on the reaction with human apolipoprotein AI.* Journal of Biological Chemistry, 1982. **257**(18): p. 10961-10966.
18. McMahon, H.T., M.M. Kozlov, and S. Martens, *Membrane Curvature in Synaptic Vesicle Fusion and Beyond.* Cell, 2010. **140**(5): p. 601-605.
19. Koller, D. and K. Lohner, *The role of spontaneous lipid curvature in the interaction of interfacially active peptides with membranes.* Biochimica et Biophysica Acta (BBA)-Biomembranes, 2014. **1838**(9): p. 2250-2259.
20. Fine, M., et al., *Massive endocytosis driven by lipidic forces originating in the outer plasmalemmal monolayer: a new approach to membrane recycling and lipid domains.* The Journal of general physiology, 2011. **137**(2): p. 137-154.
21. Swanson, J.A. and C. Watts, *Macropinocytosis.* Trends in Cell Biology, 1995. **5**(11): p. 424-428.
22. Commisso, C., R.J. Flinn, and D. Bar-Sagi, *Determining the macropinocytic index of cells through a quantitative image-based assay.* Nature protocols, 2014. **9**(1): p. 182.
23. Koivusalo, M., et al., *Amiloride inhibits macropinocytosis by lowering submembranous pH and preventing Rac1 and Cdc42 signaling.* The Journal of cell biology, 2010. **188**(4): p. 547-563.
24. Lim, J., et al., *A role for SNX5 in the regulation of macropinocytosis*. Vol. 9. 2008. 58.

25. Lewis, B.A. and D.M. Engelman, *Lipid bilayer thickness varies linearly with acyl chain length in fluid phosphatidylcholine vesicles.* Journal of molecular biology, 1983. **166**(2): p. 211-217.
26. Pidgeon, C. and C.A. Hunt, *Calculating number and surface area of liposomes in any suspension.* Journal of Pharmaceutical Sciences, 1981. **70**(2): p. 173-176.
27. Nakase, I., et al., *Active macropinocytosis induction by stimulation of epidermal growth factor receptor and oncogenic Ras expression potentiates cellular uptake efficacy of exosomes.* Scientific Reports, 2015. **5**: p. 10300.
28. Commisso, C., R.J. Flinn, and D. Bar-Sagi, *Determining the macropinocytic index of cancer cells through a quantitative image-based assay.* Nature protocols, 2014. **9**(1): p. 182-192.
29. Tisdale, E.J., A. Shisheva, and C.R. Artalejo, *Overexpression of atypical protein kinase C in HeLa cells facilitates macropinocytosis via Src activation.* Cellular signalling, 2014. **26**(6): p. 1235-1242.
30. Falcone, S., et al., *Macropinocytosis: regulated coordination of endocytic and exocytic membrane traffic events.* J Cell Sci, 2006. **119**(22): p. 4758-4769.
31. Sadekova, S., et al., *The CEACAM1-L glycoprotein associates with the actin cytoskeleton and localizes to cell–cell contact through activation of Rho-like GTPases.* Molecular biology of the cell, 2000. **11**(1): p. 65-77.
32. Sabatini, P.J., et al., *Cadherins at cell-autonomous membrane contacts control macropinocytosis.* Journal of cell science, 2011: p. jcs. 076901.
33. Gad, A.E., R. Broza, and G.D. Eytan, *Calcium-induced fusion of proteoliposomes and protein-free liposomes Effect of their phosphatidylethanolamine content on the structure of fused vesicles.* Biochimica et Biophysica Acta (BBA)-Biomembranes, 1979. **556**(2): p. 181-195.
34. van Rosmalen, M., M. Krom, and M. Merkx, *Tuning the flexibility of Glycine-Serine linkers to allow rational design of multidomain proteins.* Biochemistry, 2017. **56**(50): p. 6565-6574.
35. Khalil, I.A., et al., *High density of octaarginine stimulates macropinocytosis leading to efficient intracellular trafficking for gene expression.* Journal of Biological Chemistry, 2006. **281**(6): p. 3544-3551.
36. Gottstein, C., et al., *Precise quantification of nanoparticle internalization.* ACS nano, 2013. **7**(6): p. 4933-4945.

37. Gedye, C.A., et al., *Cell surface profiling using high-throughput flow cytometry: a platform for biomarker discovery and analysis of cellular heterogeneity.* PloS one, 2014. **9**(8): p. e105602.
38. Kang, J., E. Heart, and C.K. Sung, *Effects of cellular ATP depletion on glucose transport and insulin signaling in 3T3-L1 adipocytes.* American Journal of Physiology-Endocrinology and Metabolism, 2001. **280**(3): p. E428-E435.
39. Kondo, T. and E. Beutler, *Depletion of red cell ATP by incubation with 2-deoxyglucose.* The Journal of laboratory and clinical medicine, 1979. **94**(4): p. 617-623.

Chapter 4—Additional considerations toward proteoliposome interactions with HeLa cells

4.1—Introduction to additional considerations

In the previous chapter, interactions of Opa proteoliposomes with surface CEACAM proteins on human cells were investigated. It was found that Opa_{60} promotes proteoliposome uptake into cells compared to negative control proteoliposomes in which the CEACAM-binding hypervariable regions HV1 and HV2 of Opa_{60} were replaced with short glycine-serine regions. It was also found that expression of CEACAM1 on the cellular surface appears to promote proteoliposome uptake. Uptake of proteoliposomes into CEACAM1+, CEACAM3+, and to a lesser extent control cells depends on metabolic energy. In this chapter, additional considerations of Opa proteoliposome uptake into CEACAM+ cells are investigated, such as how progression through the cell cycle affects proteoliposome uptake, as well as addressing proteoliposome trafficking following internalization into CEACAM1+ cells. Preliminary investigations into a functional readout to indirectly measure proteoliposome internalization through delivery of a cytotoxic compound are also described.

4.2—Relevance of cell cycle and size for proteoliposome uptake

4.2.1—The relationship between cell cycle stage and protein expression profiles

In the previous chapter, a specific population of cells (CEACAM1+, CEACAM3+, control) were largely treated as a homogeneous cell sample. In reality, significant differences can exist from cell to cell within a monoclonal population [1]. Notably, cells in different growth and replication stages can express significantly different proteome profiles; this phenomenon has been studied extensively in several cell types, including HeLa cells, in order to better understand how changes in mRNA and protein expression levels correlate to cell growth and division [2, 3]. Such information is important for better understanding how different proteins

relate to normal and unregulated cell growth. For instance, one study analyzing the proteome of NB4 cells, a promyelocytic leukemia cell line, found that of 6505 proteins surveyed, 358 (approximatley 5.5%) were correlated with significant differences across different stages of the cell cycle (G_1, S, G_2, and M), with the cell-cycle stage associated with maximal expression for many proteins often correlating with a protein's role in the cell [4]. For example, proteins that bind transcription factors frequently express in the G_1 stage, while proteins associated with DNA synthesis show maximal expression in the S phase, as new DNA strands are actively synthesized [4]. Several studies have analyzed changes in mRNA expression levels in HeLa cells across different cell cycle stages and found that expression of some proteins correlates with progression through the cell cycle [5, 6]. For instance, one study of HeLa cells found that over 850 genes were periodically expressed at different stages of the cell cycle, with most genes previously-associated with tumour proliferation showing differential expression levels based on cell cycle stage [6]. 18.6% of these genes were maximally expressed in G_1, while maximal expression of 45.2% of genes was associated with G_2 [6]. Similar to previous studies, genes with maximal expression in G_1 were usually associated with replication intiation and DNA metabolism, while genes displaying maximal expression later in the cell cycle (G_2/M) frequently played roles in regulating mitotic processes and cell adhesion [6].

Because CEACAM1 is involved in cell-adhesion and can be correlated with cell proliferation and tumourigenesis [7], qualities which indicate its expression might be differentially-expressed throughout the cell cycle, the dependence of CEACAM1 expression on cell cycle progression was analyzed. In order to differentiate between early/late cell cycle cells, a histogram of DAPI intensity was plotted, producing an intensity distribution with two distinct peaks (**Fig. 1A**). These peaks correlate to cells in the G_1 and G_2 phases, with cells in the G_2 phase, occuring after DNA replication but before cell divison, characterized by their display

of approximatley double the DAPI intensity of cells in G_1 [8]. DAPI intensity for cells in the S phase falls between the G_1 and G_2 peaks, as DNA is in the process of replicating but has not fully doubled [8].

4.2.2—The relation of HeLa cell cycle to CEACAM expression, cell growth, and proteoliposome internaliation

With G_1 and G_2 CEACAM1+ cells identified through DAPI staining, the correlation between cell cycle and CEACAM1 expression was determined (**Fig. 1B**). G_2 was associated with significantly higher CEACAM1 levels than G_1, confirming that CEACAM1 expression varies with the cell cyle. This finding matches with previous reports suggesting that maximal expression of HeLa proteins involved in cell adhesion occurs later in the cell cycle. It is important to consider how overexpression of CEACAM1 may affect the association of CEACAM1 expression with the cell-cycle, however. In the stably-transfected HeLa cells used in these experiments, CEACAM1 expression is believed to be significantly higher than the expression of endogenous CEACAM in non-transfected cell lines. It would be interesting to see how lower levels of endogenous CEACAM on cells correlates with cell cycle expression. In addition to CEACAM1 expression, cell size was positively correlated with progression through the cell cycle, a finding that matches previous reports suggesting that cells often increase in size as they near division [8]. Cell size was also positively-correlated with CEACAM1+ expression (data not shown).

Since a correlation between CEACAM1+ expression and Opa proteoliposome uptake was reported in the previous chapter, it would be reasonable to expect that progression through the cell cycle, in addition to correlating with cell size and CEACAM1 expression, may also correlate with proteoliposome internalization. The results show that progression from G_1 to

G_2 phases is associated with increased Opa_{60} as well as Opa(HV-) proteoliposome uptake in both control and CEACAM1+ cells when proteoliposomes are incubated with cells for one hour (**Fig. 2**). The highest proteoliposome internalization occured with Opa_{60} proteoliposomes in the context of CEACAM1+ cells. The increase in proteoliposome internalization from G_1 to G_2 in negative controls (control HeLa cells without CEACAM, Opa(HV-) proteoliposomes) cannot be related to CEACAM expression and thus may be due to an increase in cell surface area, which would provide greater area for non-specific liposome interactions with the cells. The higher internal fluorescence values seen with Opa_{60} proteoliposomes and CEACAM1+ cells remain higher than equivalent negative controls for cells in G_1 (which internalized more proteoliposomes than negative control G_1 cells) and cells in G_2 (which internalized more proteoliposomes than negative control G_2 cells). These higher fluorescence values appear to be Opa_{60} and CEACAM1 mediated.

Similarly, due to the positive correlation between cell size and CEACAM1 expression, the relation between cell size and proteoliposome uptake was also investigated. Cells were categorized as smallest 25%, middle 50%, and largest 25% according to Brightfield area. Again, an increase in both Opa_{60} and Opa(HV-) proteoliposome uptake was seen in both control and CEACAM1+ cells as cell size increases (**Fig. 3**). The highest internal fluorescence values occured with Opa_{60} proteolipsomes and CEACAM1+ cells. The smallest 25% CEACAM1+ cells internalizing only slightly more Opa_{60} proteoliposomes than the smallest 25% of cells in control conditions (Opa(HV-) and control cells), however at larger cell sizes among control and CEACAM1+ cells (middle 50% or largest 25%), the difference in internalized proteoliposome fluorescence for CEACAM1+ cells and Opa_{60} proteoliposomes widens over the middle 50% and largest 25% of control cells and Opa(HV-) proteoliposomes. This suggests that in the smallest cells, differences in proteoliposome internalization may be difficult to discern between control conditions and Opa_{60}

proteoliposomes with CEACAM1+ cells. As cell size increases, however, the increase in proteoliposome internalization with Opa_{60} and CEACAM1 cells becomes more apparent when compared to the largest cells of control conditions. Again, the positive correlation with cell size and proteoliposome internalization seen in control conditions may be due to increased opportunities for non-specific binding with larger cells. The higher internal fluorescence values associated with Opa_{60} proteoliposomes and CEACAM1+ cells again suggests a role of Opa_{60} and CEACAM1 in proteoliposome internalization, which is promoted in the context of larger cells, perhaps due to increased CEACAM1 expression seen on the surface of larger cells.

4.3—Considerations of endocytic processing and trafficking

4.3.1—Introduction to endocytic processing and trafficking

The intracellular processing of internalized particles depends on several factors, including cell type, cargo identity, and uptake pathways utilized [9] (for an overview of various important uptake pathways, see Section 1.5.2). Of particular importance is the consideration of cargo trafficking to lysosomes following internalization. Lysosomes are low-pH (4.5-5.0) enclosed comparments containing over sixty hydrolases, which play the primary role in degradation of cargo trafficked to them during autophagy, endocytosis, and phagocytosis [10, 11]. Additionally, lysosomes play a role in degradation of protein aggregates and damaged organelles [10]. Due to the role lysosomes play in normal degradative processes, dysregulation of lysosome function can in some cases promote cancer [10].

Trafficking of cargo to lysosomes involves a complicated process of sorting, recycling, and processing, as cargo proceeds through endosomal compartments that steadily decrease in pH (**Fig. 4**) [9, 12]. Internalizaion of cargo, endocytic fluid, receptors, and membrane that occurs

after clathrin-mediated endocytosis, phagocytosis, macropinocytosis, or other uptake processes is first processed in early sorting endosomes, reached within a few minutes of internalization [13]. The purpose of early endosomes is sorting of cargo and they are morphologically-complex compartments containing several subdomains. Some subdomains cluster cargo that will be recycled back to the suface, while other domains compartmentalize cargo that is destined to proceed through further endosomal processing [13]. In these domains intended for further maturation, the pH decreases to approximately 5.5 [13]. Markers characterizing this portion of endosomal processing include Ras associated binding (Rab) proteins Rab4 and Rab5, as well as Early endosomal antigen-1 (EEA1), which is only associated with early endosomes and is commonly used to stain this compartment [13]. The Rab proteins are small GTP-binding proteins; Rab5 is the most well characterized of these proteins, and its role within early endosomes includes fusion of primary endocytic vesicles with early endosomes and mediating vesicle motility on actin and microtubules [13, 14]. Especially important is its role in recruiting several other effector proteins to early endosomes, including EEA1, which regulates early endosome fusion events through binding members of Soluble NSF(N-ethylmaleimide-sensitive factor) Attachment Protein Receptor (SNARE) proteins such as syntaxin 6 [13]. In contrast to the role of Rab5 in mediating fusion events, Rab4 on early endosomes regulates compartments destined for recycling through Rab11-recycling endosomes [13, 15]. Recycling endosomes return specific surface components, including some internalized receptors, to the plasma membrane. This recycling process can occur either through a fast pathway (approximately 5 minutes) or a slow pathway (requiring 30 minutes) [13].

After sorting by the early endosome, cargo may be sent to intracellular organelles, such as the Golgi apparatus, for further processing, or proceed further down the endosomal pathway to immature multivesicular bodies (MVBs), which eventually mature to late endosomes or

MVBs [16, 17]. This maturation process involves the loss of Rab5 and the recruitment of Rab7 and Rab9 to the endosomes [18]. Fusion of late endosomes with hydrolase-filled lysosomes appears to require Rab7, as well as soluble NSF attachment proteins (SNAPs), which facilitate vesicle tethering, formation of a trans-SNARE complex to bridge the vesicles, and eventually membrane fusion [17]. Fusion of late endosomes with lysosomes delivers the cargo into a low pH environment of 4.5-5.0, typically within 30 minutes of uptake, where degradation occurs in the presence of acidic hydrolase enzymes [19]. Lysosome associated membrane-protein 1 (LAMP1) and LAMP2 are transmembrane glycoproteins constituting the major population (>50%) of membrane proteins on lysosomes [19]. LAMP1 and LAMP2 appear to play similar roles, including maintaining lysosomal integrity [19]. Due to their high lysosome-associated expression, both LAMP1 and LAMP2 are common markers for lysosomes [20]. Additional lysosomal markers can include lysosome-associated hydrolases such as cathepsin D [21] as LAMP proteins can also be found on the cell membrane [22].

The importance of determining whether internalized liposomes are processed through the endosomal pathway is important for understanding whether cargo could experience lysosomal degradation. In cases where delivery of therapeutic compounds through liposomes is desired, escaping the endosomal pathway can facilitate access of active compounds to the cytosol or target organelles. To this end, strategies have been developed to disrupt endosomal processing of liposomes, including the creation of low-pH fusogenic liposomes, and liposomes that target delivery to specific organelles upon endocytosis [23-25].

4.3.2—Investigating trafficking of Opa_{60} proteoliopsomes to early endosomes and lysosomes in CEACAM1+ HeLa cells

To determine if uptake of Opa_{60} proteoliposomes engages the endocytic pathway, CEACAM1+ cells were exposed for 15 minutes to fluorescent Opa_{60} proteoliposomes, and then allowed to incubate further for 0, 20, 40, or 60 minutes. After incubating, cells were lifted and fixed, and then stained with an antibody specific for either EEA1 (to visualise early endosomes) or LAMP1 (to visualise lysosomes). To analyze the data in IDEAS, the Bright Detail Similarity R3 Feature was used, which compares the fluorescence of two images (here, EEA1 or LAMP1 fluorescence compared with proteoliposome fluorescence) in order to determine their colocalization. This result is calculated as a log-transformed Pearson's correlation coefficient, for which a value of 1.3 and above was defined as exhibiting colocalization. The results, reported as the percent of cells meeting the cutoff for colocalization between proteoliposome fluorescence and either EEA1 or LAMP1 fluorescence, confirm that Opa_{60} proteoliposomes colocalize with both EEA1 and LAMP1 following internalization into CEACAM1+ cells (**Fig. 5**). The percent of cells in which proteoliposomes colocalize with EEA1 increases between 0 and 40 minutes before decreasing after 40 minutes. This suggests that proteoliposome colocalization with early endosomes reached a maximum 40 minutes after exposure, after which most proteoliposomes may have passed out of early endosomes to later endocytic compartments. The fact that proteoliposome colocalization with early endosomes already occurred in approximately 10% of cells at 0 minutes post-incubation likely results from the 15 minute window in which liposomes could internalize into cells during initial exposure. This short-exposure window was necessary as liposome binding does not occur with cells at 4°C and thus binding without internalization could not be synchronized using low temperature incubations.

In contrast to proteoliposome colocalization with EEA1, which peaked around 40 minutes following proteoliposome exposure, colocalization with LAMP1 steadily increases across all 60 minutes assayed. This result suggests that proteoliposomes traffic out of early endosomes and their processing results in their eventual colocalization with lysosomes. Because this process requires trafficking through immature MVBs and late endosomes, a delay exists between colocalization with early endosomes and lysosomes. Thus, while proteoliopsome colocalization with EEA1 occurs in nearly 10% of cells immediately after proteoliposome exposure, colcoalization with LAMP1 only occurs in approximately 3% of cells. Additionally, colocalization with LAMP1 only increases across the course of the assay, unlike the drop off seen with EEA1, indicating that by 60 minutes following proteoliposome exposure, proteoliposome fluorescence continues to be associated with lysosomes.

Investigating the colocalization of Opa proteoliposomes with markers for early endosomes and lysosomes suggests that internalized proteoliposomes traffic through both these compartments. Colocalization with EEA1 peaks and then drops off by 40 minutes post-exposure, while colocalization with LAMP1 increases across the duration of the assay, likely due to proteoliposomes reaching lysosomes at the end of endosomal processing. Trafficking of Opa proteoliposomes to lysosomes could be expected to complicate therapeutic delivery to CEACAM1+ cells, as lysosomal degradation of internalized cargo would prevent cargo from reaching its intracellular target. It is unclear, however, what percent of internalized Opa proteoliposomes traffic through the full endosomal pathway in these cells, or if some population of liposomes escape before reaching lysosomes, or even avoid the endosomal pathway altogether. Analyzing proteoliposome fluorescence that colocalizes with neither EEA1 nor LAMP1 in cells shows that proteoliposomes exist within cells that do not colocalize with either of these markers, but these proteoliposomes may simply be at a stage of endosomal processing in which EEA1 or LAMP1 are not present on the compartment. To

better understand if Opa proteoliposomes can be used to mediate delivery of therapeutic compounds to cells, doxorubicin-loaded proteoliposomes were used to investigate delivery of a cytotoxic compound to HeLa cells, which is the topic of the next section.

4.4—Liposomal delivery of doxorubicin

4.4.1—Doxorubicin is a cytotoxic compound which can be delivered by nanoparticles

Therapeutic liposomes have been used for delivery of numerous active compounds, including amphotericin B and nystatin (to treat fungal infections), annamycin and daunorubicin (to treat leukemias), and vincristine (to treat Non-Hodgkin lymphoma) among many others [26-31]. One of the most commonly-studied and clinically-successful therapeutic liposome formulations is non-targetted liposomal-encapsulated doxorubicin (Doxil), approved by the FDA in 1995 to treat leukemia and cancers of the brain, bone, breast, and lung [26]. Doxil is also the only PEGylated liposome formulation currently available on the market. Doxorubicin-loaded nanoparticles are commonly used platforms for investigations into therapeutic delivery, with cellular uptake of loaded-nanoparticles occuring as soon as ten minutes following exposure and continuing for up to twenty-four hours using uptake pathways that can traffic to lysosomes [32].

The active compound in Doxil, doxorubicin, is a member of the anthracycline class of anticancer drugs isolated from the bacterium *Streptomyces peucetius* var. *caesius [33]*. Doxorubicin has two main structural regions, a water-soluble, basic (pK_a=8.15), reducing amino-sugar (daunosamine) and a water-insoluble aglycone (adriamycinone), making it amphipathic [33]. Doxorubicin is a DNA topoisomerase II inhibitor, and inhibits cell growth by inducing DNA double-strand breaks, although its exact mechanisms of action regarding strand-breakage remains unclear [33]. Doxorubicin can intercalate between DNA base-pairs

and lead to inhibition of DNA synthesis and DNA-dependent RNA synthesis through steric obstruction of the DNA strand as well as disordering of the DNA template [33]. Additionally, doxorubicin causes the formation of a covalent topoisomerase-DNA complex which can inhibit religation in replicating DNA [33]. It is possible the iron-catalyzed generation of free radicals may also be involved in doxorubicin-induced cytotoxicity [33]. Doxorubicin has also been shown to promote histone eviction from chromosomes regardless of DNA double-strand breaks [34]. DNA instability caused by doxorubicin has been shown to induce cathepsin B activity in HeLa cells, and possibly although not always activation of apoptotic factors such as Caspase 3 [35]. Doxorubicin additionally can induce release of cytochrome C from mitochondria as well as mitochondrial permeabilization [35]. Doxorubicin has been shown to be active throughout the cell cycle, although its maximal toxcitiy occurs during the DNA synthesis (S) phase, with low levels of doxorubicin causing cells to continue through the S phase before dying in G_2 [33, 36].

Doxorubicin-induced DNA strand breaks can be directly detected and quantified through imaging flow cytometry by staining of permeabilized cells with a phospho-histone H2AX (S139) antibody [37]. Following DNA strand breakage, Histone H2AX is phosphorylated (γ-H2AX) at Ser139, which serves to recruit DNA repair factors to the DNA repair foci [38]. In order to confirm that a γ-H2AX antibody would detect doxorubicin-induced DNA breakage in the HeLa cells, cells were exposed to varying concentrations of doxorubicin in the extracellular medium across two days. Following lifting of cells, fixation, and permeabilization, the cells were stained with the primary γ-H2AX antibody and a fluorescent Alexa647 secondary antibody. Additionally cell nuclei were stained with DAPI. Exposure of cells to high levels of doxorubicin (0.01 mM) resulted in DAPI nuclear staining becoming less well-defined and more punctate, as well as increased binding by the γ-H2AX antibody that localizes to the nucleus (**Fig. 6**). Cells exposed to less than 0.001 mM doxorubicin did

not see a significant change in antibody binding form buffer controls. These results match previously-reported results suggesting the IC_{50} of doxorubicin for cells was approximately 0.1 μM, but that DNA strand breaks were not detected at this concentration [39]. To better understand the effects of doxorubicin on nuclear DAPI staining, histograms of DAPI intensity were generated (**Fig. 7**). The DAPI histograms for cells exposed to low levels of doxorubicin (less than 0.001 mM) indicate expected DAPI binding, with two distinct peaks indicating cells in G_1 and G_2). DAPI intensity for cells exposed to 0.001 mM doxorubicin indicates a shift in the relative G_1 and G_2 populations, with G_1 appearing to decrase and G_2 appearing to broaden. This may result from cells progressing through S phase into G_2 before dying, as was reported previously in literature and described above. 0.01 mM doxorubicin in signficiant front-tailing for DAPI intensity, with a single peak of high intensity dominating the histogram. This may indicate a substantial increase in the G_2 population [39] as cells progress through S to G_2 but die before dividing. Additionally, DAPI intensity for cells treated with high levels of doxorubicin was higher than DAPI intensity for cells treated with buffer or low doxorubicin concentrations. DAPI interacts with DNA primarily by binding in the minor groove of AT sequences [40], and it is possible that doxorubicin effects on DNA strand structure, including inducing histone ejection as described earlier, facilitate DAPI binding to DNA by increasing access to the minor groove. If DNA strand breakage and histone ejection increases DNA minor groove sites accessible to DAPI, an increase in staining intensity could result.

4.4.2—Production of doxorubicin-loaded Opa proteoliposomes and effects on HeLa cells following exposure

Formation of liposomes with doxorubicin is typically inefficient unless a pH gradient is used to drive loading of doxorubicin into liposomes. The method used here involves creating non-fluorescent Opa_{60} proteoliposomes using normal Opa proteoliposome production methods except that proteoliposomes with folded Opa_{60} were formed in a buffer of 300 mM sodium citrate at pH 3.5, as described in published protocols [33, 41]. Opa proteins are expected to remain folded due to the high stability of folded Opa beta barrels, but the functional effects of low-pH liposomes on Opa must still be verified. Proteoliposomes were then dialyzed into 25 mM HEPES, 150 mM NaCl at pH 7.3, so that the external buffer was nearly 10,000 less acidic than the low pH internal compartment, generating a pH gradient across the liposome bilayer. Because doxorubicin is amphipathic, it is able to transition across the liposomal bilayer where it is protonated in the low pH aqueous core. This traps charged doxorubicin within the liposome, leading to its accumulation and eventual precipitation through self-association within the liposome core. Images of these doxorubicin precipitates using cryotransmission electron microscopy have shown that the preciptates form diffuse fibrous-bundles within liposomes loaded with citrate [33].

Using the protocol described, Opa_{60} and Opa(HV-) proteoliposomes were produced in a low pH citrate buffer, dialyzed into HEPES, and loaded with doxorubicin. After doxorubicin loading, proteoliposomes were dialyzed several times into HEPES buffer pH 7.3 in order to remove unincorporated doxorubicin, resulting in a red liposome mixture and clear dialysis buffer. Because doxorubicin absorbs light at 496 nm [33], the concentration of doxorubicin within the two proteoliposome samples was measured at that absorbance wavelength and compared to a standard curve in order to quantify loading. The concentration of doxorubicin was found to be approximately 97.6 µM within Opa_{60} proteoliposomes and 91.0 µM within

Opa(HV-) proteoliposomes. Although these concentrations are lower than many published concentrations (which can be 1 mM or more within liposomes) [33, 41], it is encouraging that doxorubicin concentrations between Opa_{60} and Opa(HV-) proteoliposomes are close to one another as signficant differences in loading between the two proteoliposomes could create confounding results when correlating cellular effects with proteoliposome internalization. Loading of proteoliposomes with doxorubicin exhibited significant effects on liposome size and polydispersity, as proteoliposomes loaded with only citrate buffer were approximately 288.2 nm in diameter (40% polydispersity) for Opa_{60} proteoliposomes and 250.2 nm (30.4% polydispersity for Opa(HV-) proteoliposomes, while upon doxorubicin loading, Opa_{60} proteoliposomes were found to have an average diameter of 644.6 nm (72.2% polydispersity) while Opa(HV-) proteoliposomes were found to be 611.2 nm (80.8% polydispersity). The increase in size and polydispersity following doxorubicin loading is significant and indicates that precipitation of doxorubicin within the liposomal interior destabilizes the liposomes somewhat and likely leads to increased liposomal aggregation and fusion. Further, the fact that proteoliposome size and polydispersity is high in citrate-buffered proteoliposomes without doxorubicin compared to proteoliposomes formed by usual methods (10 mM HEPES, 150 mM NaCl, pH 7.3) suggests that even low-pH citrate buffer alone is sufficient to destabilize proteoliposomes slightly. This could be explained by the fact that the lipid bilayer is partially permeable to protons, causing the formation of an electrochemical gradient across the liposomes with a slight negative interior charge when citrate-buffered liposomes are dialyzed into HEPES buffer. It could be that the formation of this electrochemical gradient destabilizes the liposomes slightly and promotes aggregation and fusion. Loading of liposomes with doxorubicin can produce nanoparticles approximately 100 nm in size and resulting in less fusion than what is seen here, and more work is needed to optimize doxorubicin loading of Opa proteoliposomes [33].

HeLa cells were exposed to doxorubicin loaded-proteoliposomes, proteoliposomes without doxorubicin, or dialysis buffer control for 30 minutes before the cells were washed several times and allowed to incubate at 37°C for several days in media. The results of four day incubations were most promising and are shown below (**Fig. 8**). Both dialysis buffer controls and proteoliposomes without doxorubicin resulted in no γ-H2AX binding within the nuclei of cells. Surprisingly, higher γ-H2AX staining was found in control cells than in CEACAM1+ HeLa cells. Additionally, higher staining was found in cells exposed to doxorubicin-loaded Opa(HV-) proteoliposomes than Opa_{60} proteoliposomes. These unexpected results appear to contradict previously-reported results showing CEACAM1+ cells internalized higher levels of proteoliposomes, and that proteoliposome uptake was promoted by Opa_{60}. Several factors may be at play here which are leading to confounding results. First, doxorubicin-loaded Opa(HV-) proteoliposomes were found to exhibit a slightly lower size and higher polydispersity than Opa_{60} proteoliposomes as described above. This may indicate a larger amount of smaller Opa(HV-) proteoliposomes were given to the cells than Opa_{60} proteoliposomes, perhaps leading to increased non-specific uptake. Additionally, the large sizes and polydispersities for both types of proteoliposomes following doxorubicin loading indicates significant liposome destabilization and aggregation or fusion, which may also indicate increased propensity for non-specific fusion with cells. Non-specific fusion of proteoliposomes to cells could occur in a manner that would still deliver doxorubicin to the cytosol without requiring active uptake and without CEACAM mediation. Previously-discussed results in Chapter 3 showed that metabolic energy plays a role in proteoliposome uptake into both CEACAM1+ and control cells, but that metabolic inhibition decreases uptake into control cells significantly less than into CEACAM1+ cells. This raised the possibility that control cells might engage liposomes in a non-specifc, non-energy dependent manner which is less accessible to CEACAM+ HeLa cells, perhaps due to high levels of

CEACAM expression on the cell surface. If so, then perhaps higher γ-H2AX fluorescence in control cells might be explained by a scenario in which control cells, with a higher propensity than CEACAM+ cells for non-energy dependent liposome interactions (such as membrane fusion), are exposed to large, polydisperse, destabilized liposome aggregates that readily fuse with cells due to doxorubicin precipitate-induced membrane destabilization. More investigation is required to understand the process leading to the unexpected results reported here. Since the significant increase in doxorubicin-induced proteoliposome swelling and polydispersity is a potential explanation, different methods for doxorubicin loading are being considered, which might better retain typical proteoliposome size and polydispersities. For example, the use of sulfate instead of citrate anion within liposomes was found to result in a tighter packing and decreased flexibility of doxorubicin fibrous aggregates [33].

In order to understand how proteoliposome-mediated doxorubicin delivery to HeLa cells affects nuclear staining, histograms of DAPI intensity were plotted (**Fig. 9**). Dialysis buffer controls and non-doxorubicin proteoliposome controls resulted in two distinct peaks for G_1 and G_2 as shown by DAPI staining, with higher numbers of cells found in the G_1 phase. Doxorubicin delivery by Opa proteoliposomes to control cells resulted in a relative lowering of the G_1 peak, and an increase in DAPI intensity, which suggests that doxorubicin delivery to control cells by Opa proteoliposomes interferes with cells dividing and proceeding back to G_1 phase after DNA synthesis in the S phase. Surprisingly, within the context of both Opa_{60} and Opa(HV-) proteoliposome-mediated doxorubicin delivery to CEACAM1+ cells, at least three distinct peaks were seen in histograms of DAPI intensity. It is currently unknown what a third peak represents if not cells in the G_1 or G_2 phase. An additional peak could result from cells accumulating in the S phase, or potentially as a result of doxorubicin increasing DNA accessibility to DAPI, but it is unclear why this occurs with CEACAM1+ cells only. Each distinct DAPI peak for doxorubicin-treated control and CEACAM1+ cells was analyzed for

correlations to γ-H2AX staining intensities (**Fig. 10**). γ-H2AX antibody intensities for control cells within either G_1 or G_2 subpopulations (first and second DAPI peaks) were not significantly different. Surprisingly, subpopulations of CEACAM1+ HeLa cells defined by their nuclear staining intensiy occuring within the first, second, or third DAPI peaks did correlate with significant differences in γ-H2AX antibody staining. The peak of lowest DAPI intensity was found to correlate with the lowest γ-H2AX antibody staining, while the peak of highest DAPI fluorescence intensity correlated with the highest γ-H2AX fluorescence for CEACAM1+ cells. More work needs to be done to understand the unexpected results discussed here.

4.5—Conclusions

In this chapter, various properties of Opa proteoliposomal uptake by CEACAM1+ HeLa cells were investigated. Additionally, progress with preliminary experiments to deliver liposomal doxorubicin to HeLa cells was discussed. It was found that progression of CEACAM1+ HeLa cells through the cell cycle correlates with increased proteoliposomal uptake. Additionally, increased cell size correlates with proteoliposomal uptake. Because progression through the cell cycle and cell size were also correlated with increased CEACAM1 expression, it may be that larger cells in later stages of the cell cycle express higher amounts of surface CEACAM1, leading to enhanced Opa proteoliposome internalization. Internalized proteoliposome fluorescence was found to colocalize with markers for both early endosomes and lysosomes, suggesting that at least some proteoliposomes are processed through the classical endocytic pathway. Finally, early experiments in delivering doxorubicin to HeLa cells using Opa proteoliposomes were discussed. Although Opa_{60}-mediated delivery of doxorubicin through CEACAM1 has not yet been established, a number of interesting

cellular effects were found to result from proteoliposomal delivery of doxorubicin, including increased numbers of DNA repair foci as measured by γ-H2AX antibody staining, as well as effects on nuclear staining by DAPI. The next chapter will summarize conclusions from the work presented in this thesis, as well as discuss various directions for future research.

A.

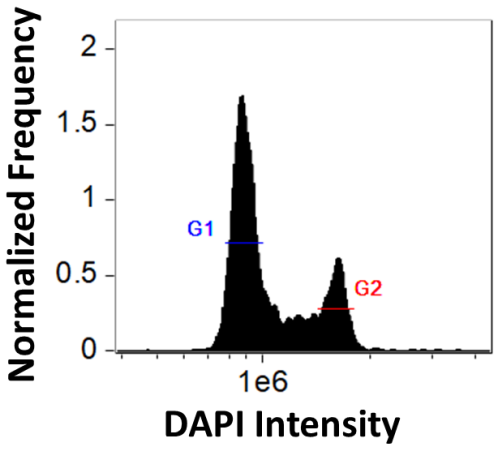

B.

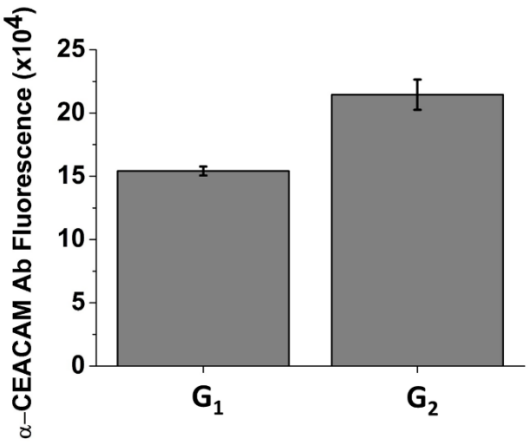

Figure 1. DAPI intensity can be used to identify cells in G_1 and G_2, which correlates with CEACAM1 expression. (A) Histogram of DAPI intensity from CEACAM1+ HeLa cells with gates set to G_1 and G_2 populations. Cells in G_2 have approximately double the DNA as G_1 cells and therefore double the DAPI intensity. (B) CEACAM1+ cells gated into G_1 and G_2 subpopulations exhibit different levels of CEACAM expression as detected by α-CEACAM antibody staining. Error bars represent 95% C.I.

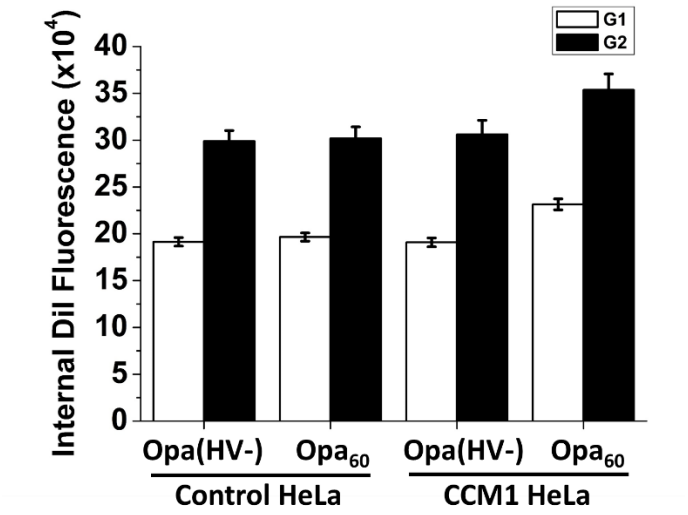

Figure 2. Progression through the cell cycle correlates with increased Opa proteoliposome uptake in CEACAM1+ and control HeLa cells. As cells progress from G_1 (white) to G_2 phase (black), proteoliposome internalization is increased. The highest internalization fluorescence values were seen with Opa_{60} proteoliposomes and CEACAM1+ Hela cells in the G_2 phase. This may be due to increased CEACAM expression on the cell surface as cells progress through the cell cycle. Approximately 2000 cells in G_1 and 1000 cells in G_2 are analysed for each condition. Error bars represent 95% C.I.

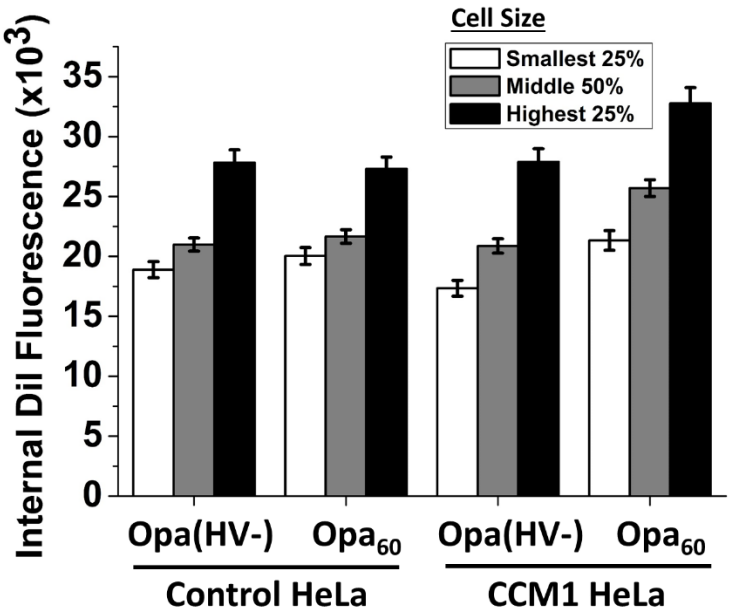

Figure 3. Cell size correlates with increased uptake of proteoliposomes. Cells gated by Brightfield Area into the lowest 25% (white), middle 50% (grey), and largest 25% (black) of cells were analysed for proteoliposome uptake. Larger cells were correlated with increased uptake. The highest uptake values were associated with Opa_{60} proteoliposomes and CEACAM1+ HeLa cells. Approximately 4000 cells were analysed for each condition before being further categorized by size. Error bars represent 95% C.I.

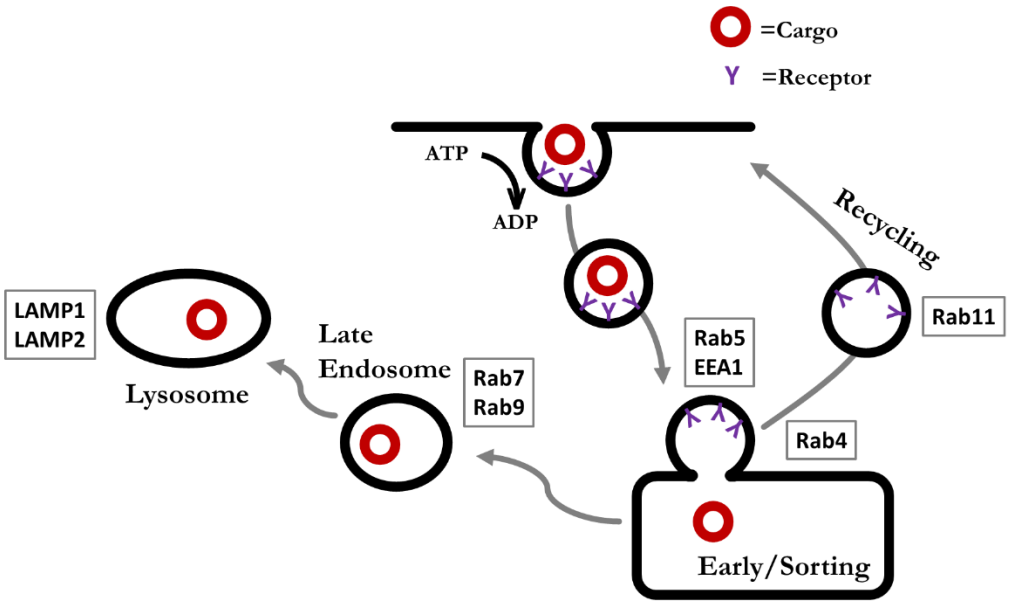

Figure 4. Schematic representation of endosomal trafficking of cargo following an active-uptake process. Example cargo (red spheres) internalized by cell-surface receptors (purple) using metabolic energy (ATP) may be processed within sorting endosomes while cell receptors cycle back to the surface. Internalized particles may then enter the endosomal pathway where they experience a significant drop in pH as endosomal compartments fuse with lysosomes. Therapeutic compounds targeted to cells that enter this pathway must either escape into the cytosol or other intracellular compartments or survive lysosomal degradation in order to exhibit efficacy. Relevant cellular trafficking proteins are given at different stages for this process in grey boxes.

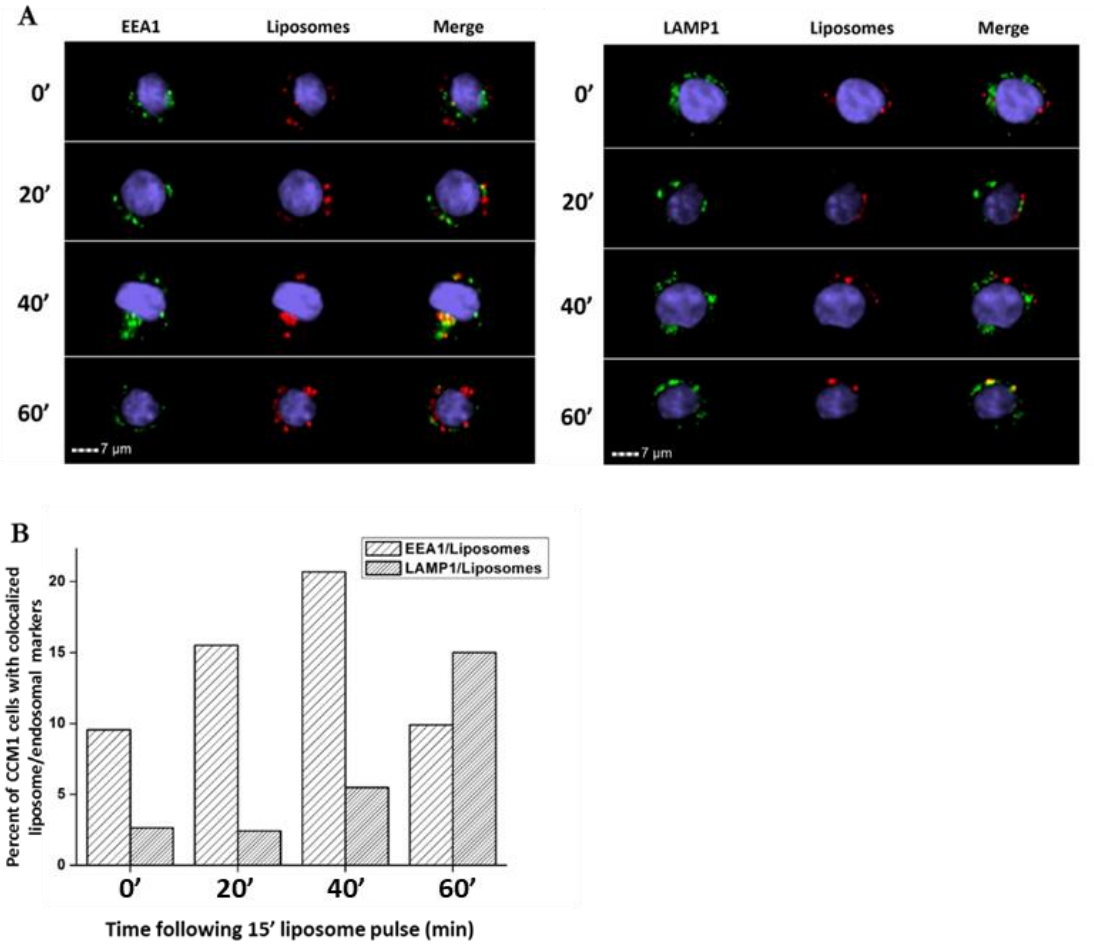

Figure 5. Opa_{60} proteoliposome fluorescence colocalizes with early endosomal antigen 1 (EEA1) and lysosome-associated membrane protein 1 (LAMP1). (A) Representative images of cells with labelled early-endosomes (EEA1, left panel, green) or lysosomes (LAMP1, right panel, green), and DiI-labelled Opa_{60} proteoliposomes (red). Red or green channel fluorescence is shown with DAPI nuclear staining (blue), along with a merged image in which colocalization between green EEA1 or LAMP1 antibody fluorescence and red liposome fluorescence appears yellow. (B) A Pearson correlation coefficient to measure colocalization between red and green pixels was measured for each cell and a gate was set at 1.3 or higher to determine cells with colocalization. The percent of CEACAM1 cells showing colocalization between liposomes and either EEA1 or LAMP1 is given for each timepoint. The fraction of cells showing colocalization between Opa_{60} proteoliposomes and EEA1 (light

grey) increases up to 40 minutes following liposome exposure. In contrast, the fraction of cells with colocalization between proteoliposomes and the lysosomal marker LAMP1 (dark grey) starts at 40 minutes following exposure, suggesting that at least some Opa_{60} proteoliposomes are processed through the endosomal pathway following internalization and reach lysosomes. Approximately 500-1000 cells that were positive for both DiI and either EEA1 or LAMP1 were analysed for each condition.

A.

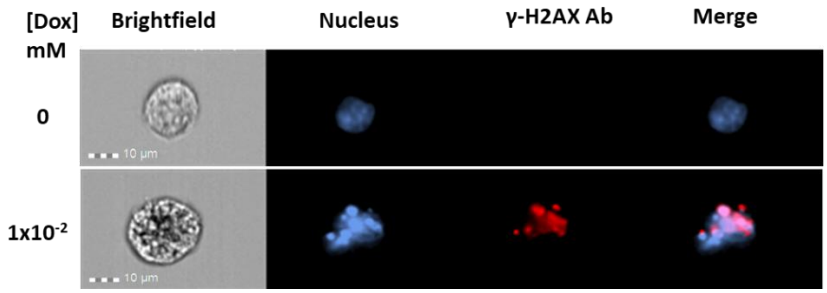

B.

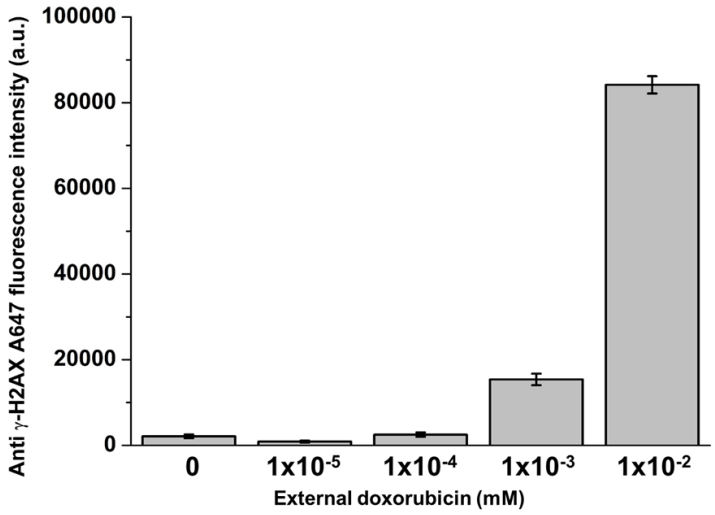

Figure 6. Effects of doxorubicin on HeLa cells can be detected by γ-H2AX antibody staining. (A) Doxorubicin-induced DNA strand breakage can be detected with a γ-H2AX antibody, which shows fluorescent punctae (red) localizing to the nucleus (blue) within HeLa cells. (B) Increasing concentrations of extracellular doxorubicin result in increased γ-H2AX antibody nuclear staining. Approximately 3000 cells were analysed for each condition. Error bars represent 99% C.I.

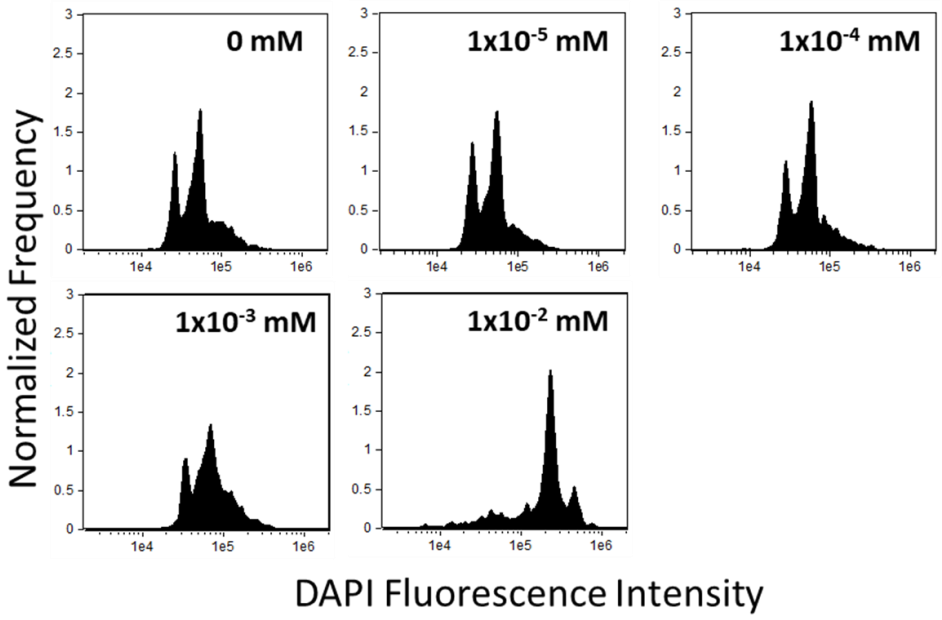

Figure 7. Increasing extracellular concentrations of doxorubicin induces changes in DAPI staining profiles and intensities. As CEACAM1+ HeLa cells are exposed to increasing concentrations of doxorubicin in the media, they exhibit a relative increase in the DAPI peak identified as G_2 as well as an increase in DAPI fluorescence intensity. Changes in DAPI staining correspond to γ-H2AX antibody staining from Figure 6, with doxorubicin concentrations below 1 μM showing little or no effect through γ-H2AX staining and DAPI intensity.

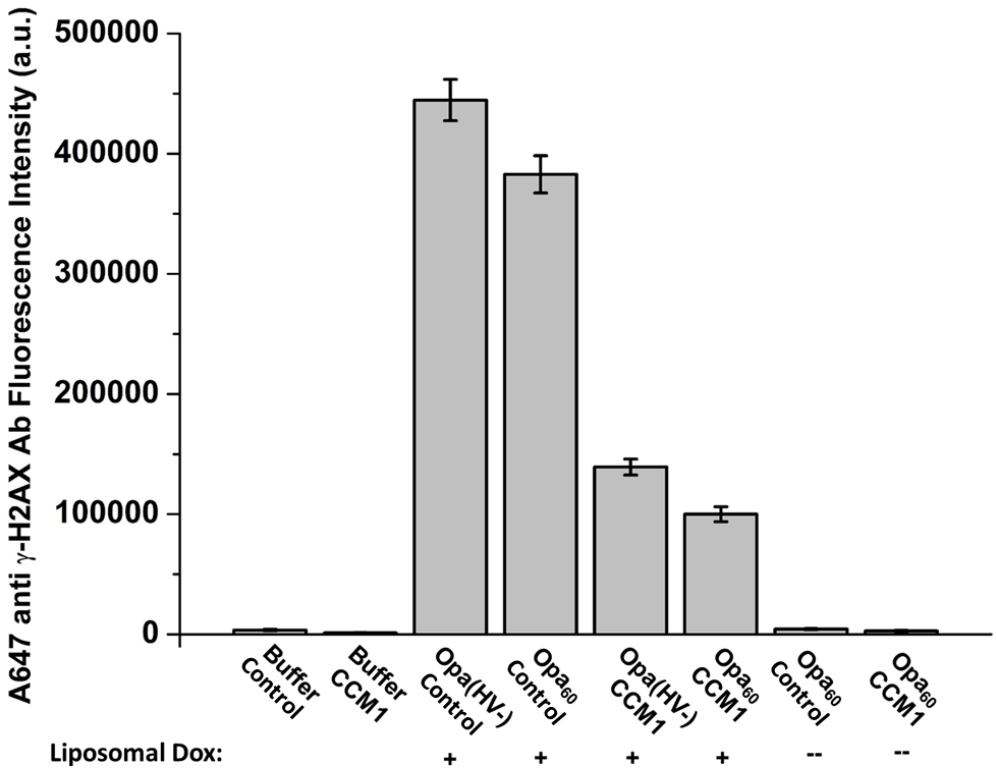

Figure 8. Exposure of CEACAM1+ and control HeLa cells with proteoliposomes loaded with doxorubicin causes an increase in γ-H2AX nuclear staining. Dialysis buffer and Opa_{60} proteoliposome controls without doxorubicin showed no effect on γ-H2AX staining. Surprisingly, the highest γ-H2AX staining levels were seen in control HeLa cells exposed to Opa(HV-) proteoliposomes. It is currently not understood why that is, although non-specific liposome fusion may be partially responsible. Approximately 3000 cells were analysed for each condition. Error bars represent 99% C.I.

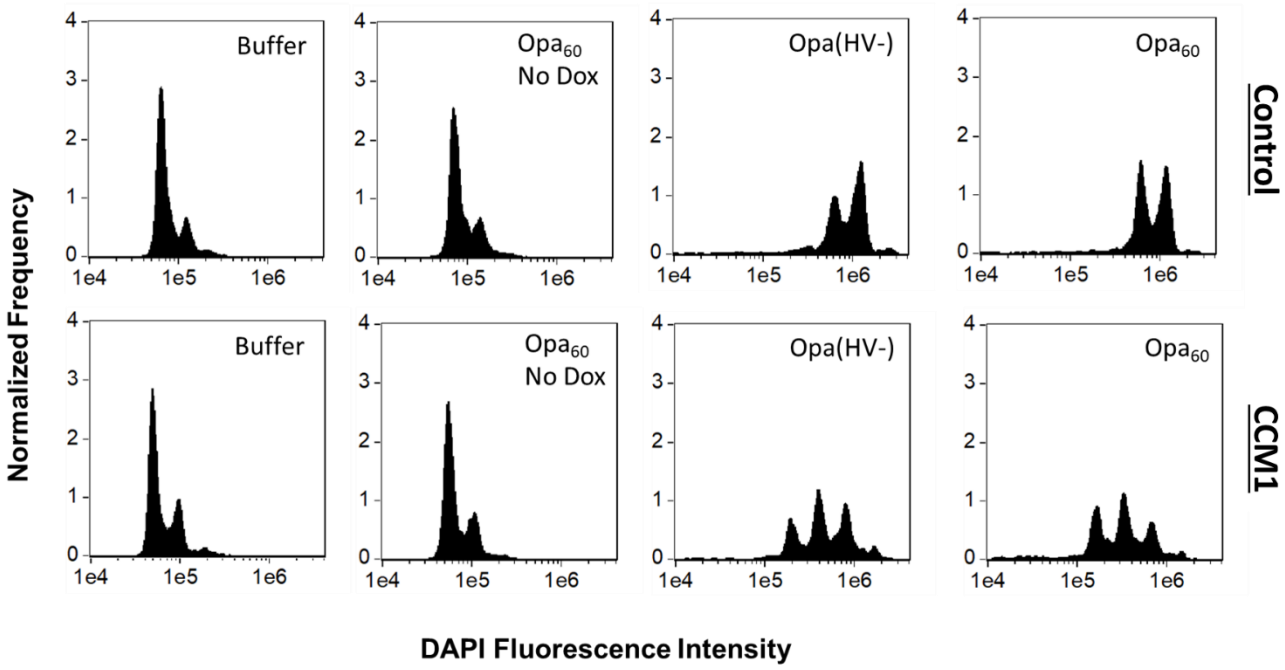

Figure 9. Doxorubicin delivery by proteoliposomes induces a change in DAPI fluorescence profiles. Compared to buffer and proteoliposome controls without doxorubicin, cellular exposure to proteoliposomes with doxorubicin causes an increase in DAPI staining intensity in CEACAM1+ and control HeLa cells. Control cells show a clear increase in the DAPI peak identified as G_2 while CEACAM1+ cells show an additional, unknown third DAPI peak. Each histogram is composed of approximately 3000 cells.

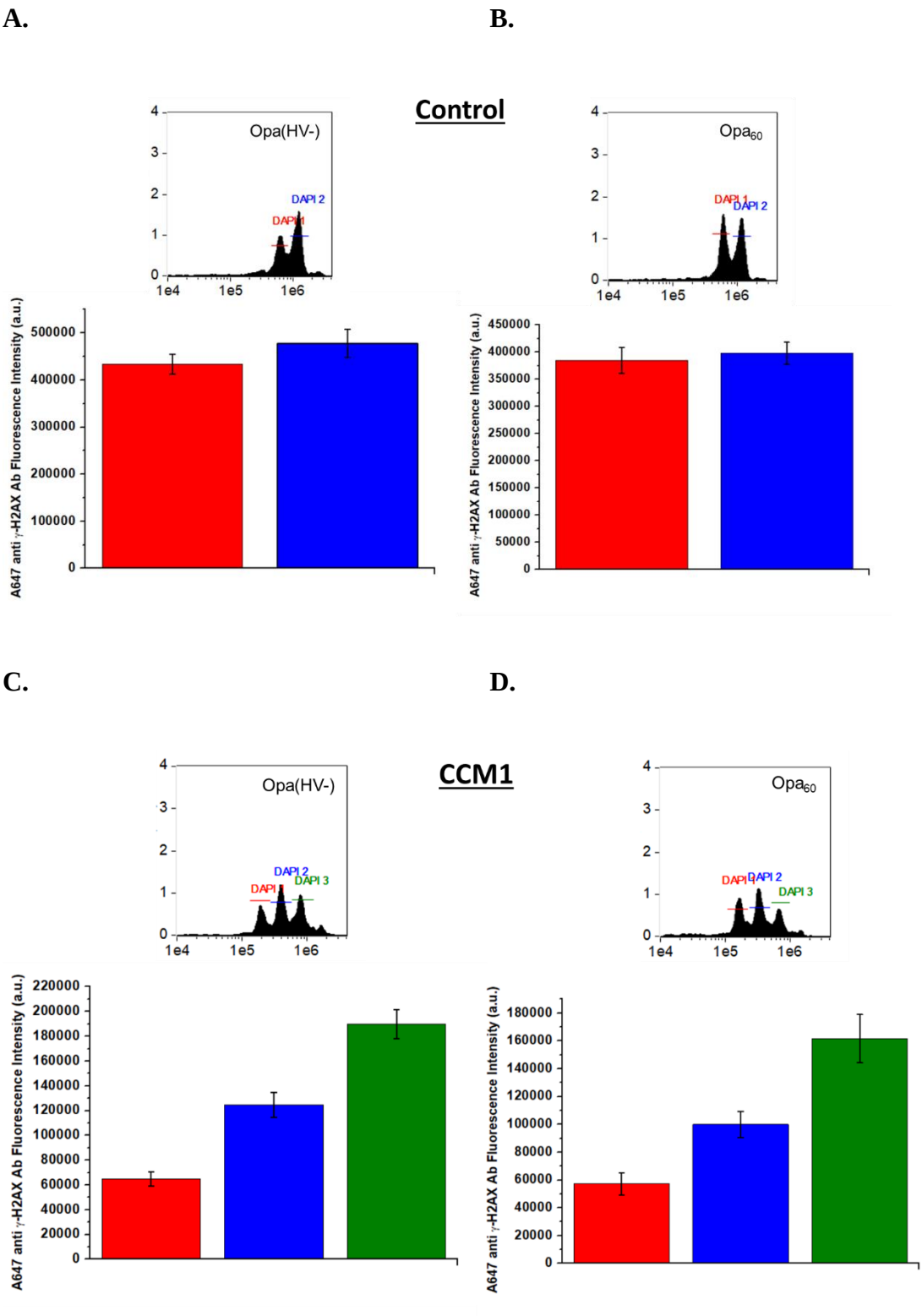

Figure 10. DAPI peaks following liposomal doxorubicin delivery correlate with increasing γ-H2AX stain in CEACAM1+ cells but not in control cells. Delivery of doxorubicin to control cells through both Opa(HV-) (A) and Opa_{60} proteoliposomes (B)

resulted in shifts in DAPI intensity. These two peaks (red, blue) did not correlate well with γ-H2AX staining. In CEACAM1+ cells, however, the three DAPI peaks (red, blue, green) do correlate with γ-H2AX staining for both Opa(HV-) (C) and Opa_{60} proteoliposomes (D). Approximately 3000 cells were analysed for each condition and further categorized into different DAPI peaks with approximately 600-1500 cells per peak. Error bars represent 95% C.I.

4.6—References

1. Gedye, C.A., et al., *Cell surface profiling using high-throughput flow cytometry: a platform for biomarker discovery and analysis of cellular heterogeneity.* PloS one, 2014. **9**(8): p. e105602.
2. Dolatabadi, S., et al., *Cell Cycle and Cell Size Dependent Gene Expression Reveals Distinct Subpopulations at Single-Cell Level.* Frontiers in Genetics, 2017. **8**: p. 1.
3. Boisvert, F.-M., et al., *A quantitative spatial proteomics analysis of proteome turnover in human cells.* Molecular & Cellular Proteomics, 2011: p. mcp. M111. 011429.
4. Ly, T., et al., *A proteomic chronology of gene expression through the cell cycle in human myeloid leukemia cells.* Elife, 2014. **3**: p. e01630.
5. Cho, R.J., et al., *Transcriptional regulation and function during the human cell cycle.* Nature Genetics, 2001. **27**: p. 48.
6. Whitfield, M.L., et al., *Identification of genes periodically expressed in the human cell cycle and their expression in tumors.* Molecular biology of the cell, 2002. **13**(6): p. 1977-2000.
7. Dankner, M., et al., *CEACAM1 as a multi-purpose target for cancer immunotherapy.* OncoImmunology, 2017. **6**(7): p. e1328336.
8. Sahumbaiev, I., et al., *Cell cycle staging from fluorescence DAPI images.*
9. Khalil, I.A., et al., *Uptake pathways and subsequent intracellular trafficking in nonviral gene delivery.* Pharmacol Rev, 2006. **58**(1): p. 32-45.
10. Dielschneider, R.F., E.S. Henson, and S.B. Gibson, *Lysosomes as Oxidative Targets for Cancer Therapy.* Oxidative Medicine and Cellular Longevity, 2017. **2017**: p. 3749157.
11. Chen, Y. and L. Yu, *Recent progress in autophagic lysosome reformation.* Traffic, 2017. **18**(6): p. 358-361.
12. Straubinger, R.M., et al., *Endocytosis of liposomes and intracellular fate of encapsulated molecules: encounter with a low pH compartment after internalization in coated vesicles.* Cell, 1983. **32**(4): p. 1069-1079.
13. Jovic, M., et al., *The early endosome: a busy sorting station for proteins at the crossroads.* Histology and histopathology, 2010. **25**(1): p. 99-112.
14. Gorvel, J.-P., et al., *rab5 controls early endosome fusion in vitro.* Cell, 1991. **64**(5): p. 915-925.

15. McCaffrey, M.W., et al., *Rab4 affects both recycling and degradative endosomal trafficking.* FEBS letters, 2001. **495**(1-2): p. 21-30.
16. Pfeffer, S.R., *Multiple routes of protein transport from endosomes to the trans Golgi network.* FEBS letters, 2009. **583**(23): p. 3811-3816.
17. Luzio, J.P., P.R. Pryor, and N.A. Bright, *Lysosomes: fusion and function.* Nature Reviews Molecular Cell Biology, 2007. **8**: p. 622.
18. Rink, J., et al., *Rab conversion as a mechanism of progression from early to late endosomes.* Cell, 2005. **122**(5): p. 735-749.
19. Eskelinen, E.-L., *Roles of LAMP-1 and LAMP-2 in lysosome biogenesis and autophagy.* Molecular aspects of medicine, 2006. **27**(5-6): p. 495-502.
20. Chen, J.W., et al., *Lysosome-associated membrane proteins: characterization of LAMP-1 of macrophage P388 and mouse embryo 3T3 cultured cells.* Archives of biochemistry and biophysics, 1985. **239**(2): p. 574-586.
21. Minchew, C.L. and V.V. Didenko, *Dual Detection of Nucleolytic and Proteolytic Markers of Lysosomal Cell Death: DNase II-Type Breaks and Cathepsin D.* Methods in molecular biology (Clifton, N.J.), 2017. **1554**: p. 229-236.
22. Baldeon, M., B. Ceresa, and J. Casanova, *Expression of constitutively active Rab5 uncouples maturation of the Salmonella-containing vacuole from intracellular replication*. Vol. 3. 2001. 473-86.
23. Kono, K., T. Igawa, and T. Takagishi, *Cytoplasmic delivery of calcein mediated by liposomes modified with a pH-sensitive poly (ethylene glycol) derivative.* Biochimica et Biophysica Acta (BBA)-Biomembranes, 1997. **1325**(2): p. 143-154.
24. Pollock, S., et al., *Uptake and trafficking of liposomes to the endoplasmic reticulum.* FASEB J, 2010. **24**(6): p. 1866-78.
25. Kube, S., et al., *Fusogenic Liposomes as Nanocarriers for the Delivery of Intracellular Proteins.* Langmuir, 2017. **33**(4): p. 1051-1059.
26. Sercombe, L., et al., *Advances and Challenges of Liposome Assisted Drug Delivery.* Frontiers in Pharmacology, 2015. **6**: p. 286.
27. Chang, H.-I. and M.-K. Yeh, *Clinical development of liposome-based drugs: formulation, characterization, and therapeutic efficacy.* International Journal of Nanomedicine, 2012. **7**: p. 49-60.
28. Wang, X., et al., *Are PEGylated liposomes better than conventional liposomes? A special case for vincristine.* Drug delivery, 2016. **23**(4): p. 1092-1100.

29. Chandrasekar, P.H., *Amphotericin B lipid complex: treatment of invasive fungal infections in patients refractory to or intolerant of amphotericin B deoxycholate.* Therapeutics and Clinical Risk Management, 2008. **4**(6): p. 1285-1294.
30. Offner, F., et al., *Liposomal Nystatin in Patients with Invasive Aspergillosis Refractory to or Intolerant of Amphotericin B.* Antimicrobial Agents and Chemotherapy, 2004. **48**(12): p. 4808-4812.
31. Wetzler, M., et al., *Phase I/II Trial of Nanomolecular Liposomal Annamycin in Adult Patients with Relapsed/Refractory Acute Lymphoblastic Leukemia.* Clinical lymphoma, myeloma & leukemia, 2013. **13**(4): p. 430-434.
32. Tang, N., et al., *Improving Penetration in Tumors With Nanoassemblies of Phospholipids and Doxorubicin.* JNCI: Journal of the National Cancer Institute, 2007. **99**(13): p. 1004-1015.
33. Abraham, S.A., et al., *The liposomal formulation of doxorubicin*, in *Methods in enzymology*. 2005, Elsevier. p. 71-97.
34. Pang, B., et al., *Drug-induced histone eviction from open chromatin contributes to the chemotherapeutic effects of doxorubicin.* Nature communications, 2013. **4**: p. 1908.
35. Bien, S., et al., *Doxorubicin-induced cell death requires cathepsin B in HeLa cells.* Biochemical pharmacology, 2010. **80**(10): p. 1466-1477.
36. Hortobágyi, G.N., *Anthracyclines in the Treatment of Cancer.* Drugs, 1997. **54**(4): p. 1-7.
37. Durdik, M., et al., *Imaging flow cytometry as a sensitive tool to detect low-dose-induced DNA damage by analyzing 53BP1 and γH2AX foci in human lymphocytes.* Cytometry Part A, 2015. **87**(12): p. 1070-1078.
38. Hesse, J.E., M.F. Faulkner, and J.M. Durdik, *Increase in double-stranded DNA break-related foci in early-stage thymocytes of aged mice.* Experimental gerontology, 2009. **44**(10): p. 676-684.
39. Fornari, F.A., et al., *Growth arrest and non-apoptotic cell death associated with the suppression of c-myc Expression in MCF-7 breast tumor cells following acute exposure to doxorubicin.* Biochemical Pharmacology, 1996. **51**(7): p. 931-940.
40. Tanious, F.A., et al., *DAPI (4', 6-diamidino-2-phenylindole) binds differently to DNA and RNA: minor-groove binding at AT sites and intercalation at AU sites.* Biochemistry, 1992. **31**(12): p. 3103-3112.

41. Fritze, A., et al., *Remote loading of doxorubicin into liposomes driven by a transmembrane phosphate gradient.* Biochimica et biophysica acta (BBA)-biomembranes, 2006. **1758**(10): p. 1633-1640.

Chapter 5—Final thoughts on work to date and ideas for future directions

5.1—Final thoughts on the results to date of Opa proteoliposome/CEACAM experiments

The aim of this research was to develop a novel method for targeting delivery of compounds to CEACAM-overexpressing cells. To this end, Opa_{60} proteoliposomes were proposed as a platform for liposomal uptake based on the ability of Opa proteins to induce engulfment of *Neisseria* through CEACAM. The lipophilic fluorophore DiI was chosen as a liposomal marker and fluorescent proteoliposomes containing DiI and folded Opa_{60} were created in order to determine binding and uptake into CEACAM+ and control HeLa cells.

In order to investigate liposome binding and uptake, a method needed to be developed in order to accurately identify surface-bound from internalized liposomes, which was the focus of Chapter 2. Using confocal microscopy, a number of membrane stains were used to delineate the membranes of HeLa cells. Stained cells could be imaged in sections through z-axis and images compressed into a z-stack image, which enabled individual fluorescent particles to be analysed for their spatial relation to the fluorophore stain. On a particle-by-particle bases, a decision had to be made as to whether each particle was internalized or surface adhered. The significant time-investment for data acquisition and analysis that this technique required, however, limited the number of cells that could be imaged per condition. Limited data sets, an inherent degree of subjectivity with denoting liposomes as internal or adhered, and inconsistent membrane staining all complicated this process, motivating a search for high-throughput alternative methods. Therefore, the applicability of imaging flow cytometry as a high-throughput method for the determination of internalized and surface-bound liposomes was investigated. To this end, a masking strategy was developed in order to denote with a high-degree of confidence the internal from surface compartments on suspended HeLa cells. Masks were validated on pre-fixed HeLa cells exposed to liposomes or

stained with antibodies on the surface, showing that an Adaptive Erode mask set to 75% of the full Brightfield mask prevented surface fluorescence from being erroneously quantified as internalized. Additionally, a spot counting feature was developed to quantify punctae within and on cells.

Chapter 3 focused on using imaging flow cytometry methods developed in Chapter 2 to quantify internal and surface fluorescence of liposomes with HeLa cells. High uptake of Opa_{50} and Opaless liposomes suggested negative-control liposomes engaged and internalized into cells at levels comparable to Opa_{60} proteoliposomes. Additionally, Opaless liposomes were found to compete with Opa_{60} proteoliposomes for uptake into CEACAM1+ cells, suggesting that proteoliposomes and Opaless liposomes internalized using the same competable pathway. It was hypothesized this pathway involved macropinocytosis due to the large size of macropinosomes compared to other endocytic vesicles and the fact that ligand receptors do not play a role in macropinocytic uptake. Opaless liposomes with diameters varying from approximately 30 nm to nearly 400 nm (formed by extrusion and confirmed by dynamic light scattering) were incubated with cells. A clear inverse correlation existed between liposome size and non-specific uptake, showing that small liposomes without Opa internalized well into HeLa cells. Uptake was inhibited by the macropinocytic inhibitor EIPA, supporting the role of macropinocytosis in non-specific uptake. Uptake by macropinocytosis was confirmed with fluorescent dextran uptake.

In order to limit the role macropinocytic uptake would play in non-specific liposome uptake, proteoliposomes were made by extrusion through 400 nm pores. Additionally, a novel negative-control Opa variant, based on removing the hypervariable regions from Opa_{60}, was created. This protein, Opa(HV-), was used in negative-control liposomes in subsequent experiments. Incubation of large, 400 nm proteoliposomes with HeLa cells resulted in uptake of both Opa_{60} and Opa(HV-) proteoliposomes into all cell types, however Opa_{60} appeared to

promote proteoliposome internalization at levels above Opa(HV-). Internalization of proteoliposomes was dependent on metabolic energy in CEACAM1+, CEACAM3+, and control cells, although this was true to a lesser extent in control cells, suggesting that proteoliposome fluorescence in control cells may partially result from a non-active process. It is currently unclear why control cells differ from CEACAM+ cells in that regard. Within CEACAM1+ cells, a positive correlation was shown between cells expressing high CEACAM and higher proteoliposome internalization.

Chapter 4 discussed various considerations of Opa proteoliposome uptake. A correlation was shown between HeLa cell progression through the cell cycle and liposome uptake, as well as a correlation between cell size and liposome uptake. As CEACAM1 expression was also shown to correlate with the cell cycle, it could be cells progressing through the cell cycle exhibit higher surface CEACAM1, causing higher Opa_{60} proteoliposome binding and engulfment. At least some proteoliposomes internalizing into CEACAM1+ HeLa cells are trafficked through the endocytic pathway, as was shown with liposome fluorescence colocalizing with markers for early endosomes and lysosomes.

Finally, proteoliposomes were loaded with doxorubicin to determine if Opa-CEACAM binding could lead to delivery of an active therapeutic compound to cells. Doxorubicin effects could be measured by antibody staining for phosphorylated H2AX, as well as through DAPI staining. Both Opa_{60} and Opa(HV-) proteoliposomes delivered doxorubicin to CEACAM1+ and control cells, with Opa(HV-) proteoliposomes and control cells being associated with higher γ-H2AX antibody staining. This could possibly result from an increased propensity for membrane fusion by liposomes after doxorubicin loading, although more investigation is needed.

In summary, imaging flow cytometry was used to develop a convincing method to determine liposomal internalization and surface binding. Progress was made toward understanding Opa-CEACAM mediated proteoliposome internalization, especially the propensity of cells to engage in non-specific uptake, which appears to be largely through macropinocytosis. Non-specific uptake of liposomes through macropinocytosis can be modulated by changing vesicle size. Understanding the relationship between liposome size and non-specific internalization was an important step in being able to show a difference between Opa_{60} and control liposome uptake since using larger liposomes decreased non-specific uptake and caused Opa-mediated uptake to emerge more clearly. Despite this progress, uptake of Opa(HV-) proteoliposomes still remains high in all cell types but CEACAM3+ cells, as does uptake into control cells.

5.2—Ideas for future directions

There remains much work to be done in order to fully elucidate the properties and mechanisms behind Opa_{60} and Opa(HV-) proteoliposome uptake into the stably-transfected CEACAM1+, CEACAM3+, and control HeLa cells studied here. Although this thesis presented strategies to investigate Opa_{60} and Opa(HV-) proteoliposome uptake which demonstrate clear differences in internalization between Opa_{60} and negative control proteoliposomes, there remains a need to more fully understand why control proteoliposomes internalize into the HeLa cells studied here at such high amounts. To this end, a new version of Opa(HV-) in which the semivariable region has been removed is being generated. Although the SV region alone is not able to induce binding to CEACAM, it would be interesting to see how an Opa(HV- SV-) variant differs in its interactions with the cells. Additionally, liposomes containing larger molecular weight PEG polymers than the PEG-1000 used in these experiments could interact differently with HeLa cells, and it would be

interesting to assay how liposomes with PEG-5000 on their surface interact with CEACAM1+ and control HeLa cells.

In order to further probe the relevance of CEACAM in mediating Opa proteoliposome uptake, CEACAM1 expression could be knocked down within CEACAM1+ HeLa cells using RNA interference (RNAi). RNAi uses double-stranded RNA to selectively inactivate messenger RNA for a specific gene within cells, silencing its expression [1]. It would be illuminating to determine how decreasing CEACAM1 expression within the context of stably-transfected CEACAM1+ HeLa cells interferes with liposome uptake. If proteoliposome uptake is decreased following RNAi, this result would suggest that high proteoliposomal uptake by control HeLa cells results from different properties between CEACAM1+ and control cells. This could possibly be due to a different propensity for liposome adhesion or fusion on the surface, implied by the fact that the decrease in proteoliposome uptake in control cells treated with metabolic inhibitors was far less than the decrease in uptake seen in treated CEACAM1+ or CEACAM3+ HeLa cells. An alternative method to probe CEACAM relevance toward uptake could be through blocking Opa-CEACAM interactions, perhaps through treatment of cells with an α-CEACAM antibody prior to liposome exposure. Incubation of cells with an antibody that binds the N-terminus of CEACAM could sterically-block proteoliposomes from binding CEACAM while retaining CEACAM proteins on the cell surface, and would be expected to result in a decrease in liposome binding and uptake through CEACAM.

There also remains much work to be done to elucidate what mechanisms of uptake are employed by HeLa cells regarding proteoliposome internalization. To this end, chemical inhibitors of various uptake processes should be screened for their efficacy in decreasing Opa proteoliposome entry into cells. Staurosporine is a broad spectrum serine-kinase inhibitor which has been suggested to inhibit *Neisseria* uptake mediated by CEACAM1 and

CEACAM3 [2]. It would be interesting to see whether treatment of the HeLa cells used here with staurosporine shows any effect on proteoliposome uptake. Similarly, the Src family kinase inhibitor PP2 could also be assayed to see its effects on uptake [2]. Importance of microtubules or actin microfilaments to CEACAM1 or CEACAM3-mediated uptake could be determined with nocodazole and cytochalasin D, respectively [3-5]. Clathrin-mediated endocytosis can be probed by treatment of cells with dynasore, an inhibitor of dynamin, which is required for membrane fission in CME uptake [6].

Finally, much work remains in order to deliver an active compound such as doxorubicin to CEACAM+ cells using Opa proteoliposomes. It was described here how doxorubicin exerted cytotoxic effects on HeLa cells independent of liposomal Opa_{60}, and that doxorubicin-induced DNA strand breakage was increased in control cells to levels even higher than CEACAM1+ cells. The current hypothesis is that doxorubicin loading into proteoliposomes is destabilizing the liposomes and promoting liposomal aggregation and fusion, suggested by measuring liposome size and polydispersity by dynamic light scattering. In order to better control liposome size, the precipitation of encapsulated doxorubicin can be modulated by the loading technique employed. Use of sulfate instead of citrate when establishing a pH gradient within liposomes, for example, was shown to affect the shape and flexibility of doxorubicin fibrous bundles, making them more tightly packed than when precipitated with citrate [7]. Modulating doxorubicin precipitation may change the membrane aggregation properties of the liposomes and allow for more clear results with respect to cellular delivery.

There remain many avenues of research that could be followed based on the work described in this thesis, but the ideas given in this section seem to be of particular importance. Regardless, it is clear from the work described here that there remains much potential for Opa proteoliposomes to be developed further as a platform for therapeutic delivery to cells expressing surface CEACAM proteins.

5.3—References

1. O'Keefe, E., *siRNAs and shRNAs: Tools for protein knockdown by gene silencing.* Word Lab, 2013.
2. McCaw, S.E., E.H. Liao, and S.D. Gray-Owen, *Engulfment of Neisseria gonorrhoeae: Revealing Distinct Processes of Bacterial Entry by Individual Carcinoembryonic Antigen-Related Cellular Adhesion Molecule Family Receptors.* Infection and Immunity, 2004. **72**(5): p. 2742-2752.
3. Vasquez, R.J., et al., *Nanomolar concentrations of nocodazole alter microtubule dynamic instability in vivo and in vitro.* Molecular Biology of the Cell, 1997. **8**(6): p. 973-985.
4. Saunders, C. and L.E. Limbird, *Disruption of microtubules reveals two independent apical targeting mechanisms for G-protein-coupled receptors in polarized renal epithelial cells.* Journal of Biological Chemistry, 1997. **272**(30): p. 19035-19045.
5. Casella, J.F., M.D. Flanagan, and S. Lin, *Cytochalasin D inhibits actin polymerization and induces depolymerization of actin filaments formed during platelet shape change.* Nature, 1981. **293**: p. 302.
6. Preta, G., J.G. Cronin, and I.M. Sheldon, *Dynasore - not just a dynamin inhibitor.* Cell Communication and Signaling : CCS, 2015. **13**: p. 24.
7. Abraham, S.A., et al., *The liposomal formulation of doxorubicin*, in *Methods in enzymology*. 2005, Elsevier. p. 71-97.

Appendix: Various Experimental Methods and Materials Used

Propagation of HeLa cells. HeLa cells stably transfected to express CEACAM or a control plasmid were cultured in a 37°C incubator with 5% CO_2 in a solution of Dulbecco's Modified Eagle Media (DMEM) (Gibco, 11965-092) supplemented with 10% fetal bovine serum (VWR, 97068-085), 1x Anti-anti (Gibco, 15240-062), and 1x Glutamax (Gibco, 35050-061). Cells were split using 0.25% trypsin- ethylenediaminetetraacetic acid (EDTA) (Gibco, 25200-056) when ~80% confluent and discarded by 25 passages in order to preclude endogenous CEACAM expression in control cells. HeLa CEACAM expression was monitored by Western blot with a polyclonal CEACAM antibody (Dako, A0115).

Staining of HeLa cells for surface CEACAM. HeLa cells were allowed to grow to ~60% confluence before lifting with 2 mM EDTA in phosphate buffered saline (PBS). Cells were centrifuged at 300 g and fixed in 4% paraformaldehyde (PFA) in PBS for 15 minutes before being centrifuged again and washed with PBS containing 10% normal-goat serum (NGS) to block non-specific antibody binding. Antibody staining was done with a rabbit polyclonal pan-CEACAM antibody (Dako, A0115) for 1 hour. Following two rounds of washing with 10% NGS in PBS, the cells were stained with an Alexa-647 goat anti-rabbit antibody (ThermoFisher). Cells were washed with PBS and stored at 4°C for imaging.

Expression and purification of recombinant Opa proteins. opa_{60} and opa(HV-) genes subcloned into pET28b vectors were transformed into a BL21 (DE3) *E. coli* strain in order to produce Opa proteins as described previously. Briefly, cells were grown in LB supplemented with kanamycin until they reached an $OD_{600} \approx 0.8$, when protein expression was induced with isopropyl-β-D-thiogalactoside. Following Opa expression into inclusion bodies, cells were centrifuged and then resuspended in lysis buffer [50 mM Tris (pH 8.0), 150 mM NaCl, Complete protease inhibitor tablet] before being lysed. The insoluble protein fraction was

pelleted (5,000 x g) and resuspended in extraction buffer (lysis buffer with 8 M urea) overnight. The remaining insoluble fraction was removed through centrifugation and soluble Opa proteins were purified using Co^{2+}-immobilized metal affinity chromatography and eluted [20 mM sodium phosphate (pH 7.0), 150 mM NaCl, 680 mM imidazole, 8 M urea]. The eluted fractions containing Opa were concentrated (MWCO= 10kDa) and the final Opa concentration was determined by A_{280} (MW= (29367.5 Da), ε=41830 M^{-1} cm^{-1} for Opa_{60}; MW=22487.8 Da, ε=37360 M^{-1} cm^{-1} for Opa(HV-)). Protein purity was assessed with SDS-PAGE.

Preparation of fluorescent liposomes and size determination by dynamic light scattering. A fluorescent lipid mixture composed of 62 mol% 1,2-dimyristoyl-*sn*-glycero-3-phosphocholine (DMPC), 16 mol% 1,2-dimyristoyl-*sn*-glycero-3-phospho(1'-rac-glycerol) (sodium salt) (DMPG), 16 mol% cholesterol, 5 mol% 1,2-dimyristoyl-*sn*-glycero-3-phosphoethanolamine-*N*-[methoxy-(polyethylene glycol)-1000] (ammonium salt) (DMPE PEG 1000), and 1 mol% (DiI) (ThermoFisher, D282) was dried under a stream of nitrogen and resuspended in 10 mM HEPES in Hank's Balanced Salt Solution (HBSS). The resulting lipid mixture was vortexed for 5 minutes and shaken at 500 rpm overnight before being hand-extruded through a Nucleopore track-etched membrane with pore sizes of 0.03 µm, 0.1 µm, 0.2 µm, and 0.4 µm (Whatman). Liposome sizes were determined by dynamic light scattering (DLS) using a Wyatt DynaPro Plate Reader II and Dynamics V7 software. Ten repeats were measured for each condition and the average liposome size was reported.

Preparation of fluorescent Opa proteoliposomes. Opa protein folding was adapted from previously published protocols. 1,2-didecanoyl-*sn*-glycero-3-phosphocholine (diC10PC, Avanti Polar Lipids) dissolved in chloroform was dried under nitrogen and resuspended in borate buffer [10 mM sodium borate (pH 12.0) and 1 mM EDTA], then sonicated for 30 minutes at 40% amplitude (Q500, Q Sonica) in order to form liposomes. Following

sonication, 4 M urea was added and 50 nm unfolded Opa_{60} or Opa(HV-) was aliquoted and mixed. The Opa/diC10PC-liposome mixture was incubated for 4 days at 37°C, after which folding was confirmed by SDS-PAGE. Following Opa folding, diC10PC-proteoliposomes were pelleted through ultracentrifugation (142,400 x g for 2 hrs at 12°C), resuspended in resuspension buffer [10 mM HEPES (pH 7.4) in HBSS], and mixed with dried fluorescent lipids (DMPC, DMPG, cholesterol, DMPE-PEG-1000) as described above. The lipid mixture was vortexed for 5 minutes and shaken at 500 rpm for several hours before extrusion through a Nucleopore track-etched membrane with a 0.4 or 0.2 µm pore size (Whatman).

Proteoliposome incubation with pre-fixed HeLa cells. Prior to Opa_{60} proteoliposome exposure, 2.0 x 10^6 CEACAM1 HeLa cells per condition were lifted and fixed with 4% paraformaldehyde in PBS for 10 minutes. Cells were centrifuged (300 g, 10 min) and washed with PBS and then exposed to Opa_{60} proteoliposomes in 10 mM HEPES/HBSS (pH 7.4) at a final phospholipid concentration of 0.2 mM for two hours. Cells were then centrifuged and washed with PBS before being fixed as previously described. Cells were washed in PBS and then incubated with 1:1000 DAPI in PBS for one hour before being washed once more and stored in PBS for imaging.

Timecourse of Opa proteoliposome uptake. Approximately 20 hours prior to liposome exposure, 2.0 x 10^6 HeLa cells expressing CEACAM1, CEACAM3, or a vector control line were seeded onto 60 x 15 mm cell culture plates (Cellstar, 628160). Proteoliposomes were produced as described above and extruded through a 0.4 µm membrane. Before the experiment, the liposomal phospholipid concentration was determined according to established protocols. HeLa cells were exposed to liposomes at a concentration of 0.2 mM total phospholipid for 20 minutes at 37°C in serum-free DMEM. Following liposome exposure, cells were washed again and allowed to incubate further for 0, 1, 2, or 3 hrs before being washed again and lifted by 2mM EDTA in PBS (pH 7.4). Cells were pelleted by

centrifugation at 300 x g for 10 minutes and then fixed in 4% PFA in PBS for 15 minutes before being pelleted at 400 x g for 10 minutes. The cell pellet was resuspended in PBS and stained with 1:1000 DAPI in PBS for one hour before being centrifuged and washed with PBS. Cells were stored at 4°C prior to imaging.

Inhibition of cells with ATP-metabolic inhibitors. 2.0 x 10^6 HeLa cells per plate were seeded the day before the experiment. Opa proteoliposomes were prepared as described previously. The day of the experiment, cells were pre-incubated for 30 minutes at 37°C with DMEM + 10 mM sodium azide and 100 mM 2-deoxyglucose (Sigma). Opa proteoliposomes were given at a concentration of 0.1 mM total phospholipids for 1 hour at 37°C, after which the cells were washed, lifted, and fixed as described previously. Cells were stained with 1:1000 DAPI in PBS before centrifugation at 400 g. Cells were washed with PBS and stored at 4°C prior to imaging.

Imaging flow cytometry. Cell imaging was performed on an ImageStream^X Mark II imaging flow cytometer (Amnis Corporation). DAPI fluorescence was excited with a 405 nm laser set to 40.0 mW intensity and emission was collected with a 420-505 nm filter (Ch 7). TMR-dextran fluorescence was excited with a 488 nm laser set to 100.0 mW intensity and emission was collected with a 595-660 nm filter (Ch 4). DiI fluorescence was excited with a 488 nm laser set to 100.0 mW intensity and a 561 laser set to 100.0 mW intensity and read using a 560-595 nm filter (Ch 3). Alexa-647 fluorescence was excited using a 642 nm laser set to 40.0 mW intensity and collected with a 660-740 nm filter (Ch 11). Brightfield images were collected on Ch 1 (camera 1) and Ch 9 (camera 2). Images were captured using a 60X, 0.9 NA objective. Approximately 4000-8000 in-focus, nucleated cells were captured for each sample. Single-label controls were imaged at the same settings to generate a compensation matrix.

Image processing. Images were analysed using IDEAS V. 6.2.64.0 software (Amnis Corporation). For each file, a compensation matrix created using single-label controls was applied to reduce spectral overlap between channels. In-focus cells were selected using a Brightfield RMS gradient, while single cells were gated on by plotting the Brightfield area against the aspect ratio. An internalization mask was created by an Adaptive Erode algorithm (100-75%, with 75% Adaptive Erode used to define the internal mask) applied to a Brightfield mask in order to exclude fluorescence at the membrane. A surface mask was designed by subtracting a 90% Adaptive Erode mask from the full Brightfield mask in order to capture fluorescence only at the cell surface. For DiI fluorescence measurements, a mask was applied to each cell to select for Ch3 (DiI) fluorescence intensity between 100-4095 greyscale value in order to exclude low-level background fluorescence (background threshold). An internalization or cell surface mask was combined with a DiI background threshold mask in order to quantify above-background DiI fluorescence either within or at the surface of the cell. For *E. coli,* a spot count algorithm was used instead of intensity in order to quantify the average number of spots (bacteria) per cell. To measure internalized TMR-dextran fluorescence, a background threshold mask was created to exclude Ch4 TMR intensity outside a 70-4095 greyscale value range. Ch4 (TMR) fluorescence intensity was quantified within the TMR background threshold mask and the Internalization mask.

E. coli growth conditions and labelling

A BL21 (DE3) *E. coli* cell strain was transformed with either a pEX vector subcloned with the *opaI* gene or an empty control vector. Cells were grown for 17 hours in ampicillin-supplemented Lysogeny Broth (LB) media containing 15 µg per mL of 1,1’-Dioctadecyl-3,3,3’,3’-Tetramethylindocarbocyanine Perchlorate (DiI) (Thermo Fisher, D282) until they

reached an OD_{600} of 1.0 (approximately 8.0 x 10^8 cfu/mL). *E. coli* were centrifuged at 4000 g for fifteen minutes and red cell pellets were observed. The pellets were washed twice in LB media before being suspended in LB to a final concentration of approximately 2.5 x 10^9 cfu/mL.

Incubation of Fluorescent E. coli with HeLa cells

HeLa cells stably-transfected to express CEACAM1, CEACAM3, or a vector control line were seeded onto plastic plates approximately 20 hrs prior to the experiment. The day of the experiment HeLa cells were washed with fresh media without FBS and cell counts for each line were determined. *E. coli* cells were diluted in DMEM and exposed to cells at a MOI of 50 cfu/cell for one hour at 37°C. Following a one hour exposure to bacteria, the HeLa cells were washed with fresh DMEM and allowed to incubate at 37°C for another four hours. At the end of the experiment, the cells were washed with DMEM before being lifted by 2mM EDTA in PBS (pH 7.4). Cells were spun at 300 g for 10 minutes and then fixed in 4% paraformaldehyde (PFA) for 15 minutes at room temperature. Cells were centrifuged at 400 g for 10 minutes, washed with PBS, and then stained with 1:1000 DAPI in PBS for 1 hour. Cells were washed again with PBS and then stored at 4°C prior to imaging.

Determining Macropinocytic Uptake of HeLa Cells

Macropinocytosis was quantified according to a published protocol as described in the text. Briefly, 2.0x10^6 cells were plated one day prior to the experiment. The day of the experiment, HeLa cells were washed with serum-free DMEM and incubated with 1 mg ml^{-1} lysine-fixable 70kDa Tetramethylrhodamine (TMR)-dextran (Invitrogen, D1818) at 37°C for 30 min. After, the cells were washed twice with serum-free DMEM then lifted with 2 mM EDTA in PBS and centrifuged at 300 g for 10 minutes. Cells were fixed with 4% PFA in PBS for 15

minutes at room temperature, centrifuged at 400 g, and stained with 1:1000 DAPI in PBS for one hour. Cells were finally centrifuged again and washed in PBS before being stored at 4°C prior to imaging. To inhibit macropinocytosis, cells were pre-exposed to 100 μM 5-(N-Ethyl-N-isopropyl)amiloride (EIPA) (Sigma) for 30 minutes in serum-free DMEM just prior to liposome exposure.

Colocalization of Opa_{60} proteoliposomes with EEA1 or LAMP1

0.2 mM [phosopholipid] of Opa_{60} proteoliposomes were exposed to $2.0x10^6$ CEACAM1 HeLa cells for 20 minutes in DMEM. Following liposome exposure, cells were washed and allowed to incubate further for 0, 20, 40, or 60 minutes. After incubation, cells were washed again with media, lifted with 2mM EDTA in PBS, and fixed with 4% PFA in PBS as described in Materials and Methods. Cells were centrifuged and resuspended in 10% normal-goat serum in PBS with 0.2% saponin to permeabilize the membranes. Antibodies to EEA1 (BD Biosciences, 610456) or LAMP1 (DSHB, H4A3) were incubated with cells 1:100 concentration along with 1:1000 DAPI, following which cells were centrifuged and washed with PBS. A goat anti-mouse Alexa488 secondary antibody was incubated with cells 1:1000 for 1 hour before cells were centrifuged and washed again in PBS for imaging.